Single-Molecule Magnets and their Electronic and Magnetic Interactions with Metallic Surfaces

Zur Erlangung des akademischen Grades eines
Doktors der Naturwissenschaften (Dr. rer. nat.)

von der KIT-Fakultät für Physik des
Karlsruher Instituts für Technologie (KIT)
genehmigte

Dissertation

von

M. Sc. Timo Frauhammer

Tag der mündlichen Prüfung:	20. November 2020
Referent:	Prof. Dr. Wulf Wulfhekel
Korreferent:	Prof. Dr. Wolfgang Wernsdorfer

Contents

1 Introduction

The digitalization of our society has advanced at an almost frightening pace during the last decades. The cause lies in the continuous progress in semiconductor technology and nano-fabrication methods. Therein, the efforts of semiconductor and computer industry were always towards building transistors, integrated circuits and even whole data processing systems as compact and powerful, but at the same time as efficient and cheap as possible. As one remarkable result of these aspirations, one can nowadays easily carry around portable devices like smartphones with computing capacities many orders of magnitude higher than the first commercial personal computers released in the 1980s. However, eventually this development will face natural given boundaries. Besides the diffraction limit of optical lithography, the lifetime of nanostructures declines drastically towards smaller structure size due to thermal diffusion of atoms. Furthermore, when the structure size approaches the nanometer scale, quantum mechanical effects play a non-negligible role, which in turn may result in the loss of functionality. One example would be a field effect transistor, which at too small size cannot avoid leakage currents in its off state because of quantum tunneling. Similarly, magnetic bits or floating gate transistors require a minimum size in order to ensure the long-time stability.

Therefore, the interest in alternative technologies has progressively increased in science and research. Among others, molecular spintronics [1] and quantum computing [2, 3, 4] are particularly prominent research domains in this respect. Both disciplines have in common, that they aim to exploit quantum properties of single atoms [5, 6], molecules [7], photons [8] or solid-state systems [4, 9], rather than suppress or avoid them. Besides the minimum structure size that can be achieved, this approach may additionally yield whole new types of functional units and devices. For both,

application in high-density data storage and quantum computing, magnetic systems, especially magnetic molecules and atoms, seem to be particularly interesting prospects.

The first so-called *single-molecule magnet* (SMM), the Mn_{12} cluster, was reported in 1993 [10, 11, 12]. In their pioneering work Sessoli et al. were able to observe, that these clusters show large spin-relaxation times and even magnetic hysteresis due to the bistability of their magnetic moment at low temperatures. This illustrated for the first time, that single magnetic molecules might be suitable to serve as magnetic bits for data storage. With this the quest for searching more stable SMMs with higher spin lifetimes began. The prototypical candidates are usually metal-organic complexes consisting of one or more magnetic ions, that are surrounded by organic ligands. It turns out that the stability and spin lifetime of an atomic magnetic moment is determined mostly by its chemical environment. By optimizing the molecular structure and symmetry, stability of magnetic moments up to temperatures of 60 K were reported for single-ion magnets based on rare earth ions [13].

But not only the search for suitable and stable SMMs for data storage, but also potential application in quantum computing attract more notice [7, 14]. For this purpose, the coherence of spin states is crucial, which is why also the nuclear spin states of an SMM may be considered to serve as qubits [15]. The most famous example is the $TbPc_2$ molecular magnet, where electronic readout [16] and coherent manipulation [17] of the terbium nuclear spin states was demonstrated, such that even Grover's algorithm could be implemented [18, 19].

One extremely important aspect - with a view to possible application of SMMs - is the electrical contact formation of a molecule, which is necessary for readout, manipulation and integration. On the single-molecule scale the usual solution to this is to either trap the molecule inside a break junction [20, 21, 22], or to simply deposit it on a metallic substrate in order to investigate it using scanning tunneling microscopy [23]. The latter allows imaging, contact formation, manipulation and spectroscopy of single molecules. It turns out, though, that the properties of a molecule are

substantially affected by its interaction with the metallic leads or surfaces. This issue will play a prominent role in all three projects of this thesis, where different single magnetic molecules were investigated mainly by low temperature scanning tunneling microscopy.

In the first project, bis(phthalocyaninato)dysprosium ($DyPc_2$) molecules were investigated. Generally, SMMs based on rare earth ions are considered particularly promising candidates, since the 4f electrons often exhibit large magnetic moments, which in turn is essentially electronically decoupled from its environment. Thereby, the magnetic moments are expected to be rather stable, however electronic readout and access are impeded. The results of this thesis, based on the aforementioned reports on $TbPc_2$, will illustrate how the molecule-substrate coupling can be exploited in order to read out the dysprosium moment indirectly in scanning tunneling microscopy. With this, intriguing perspectives to also address the dysprosium nuclear spin in scanning tunneling microscopy arise.

The second project deals with transition metal acetylacetonates. In contrast to rare earth systems, single-ion magnets based on the magnetic moment of 3d electrons have the advantage, that their magnetic moment can readily be addressed and read out in terms of electronic transport [24, 25]. In the framework of this work, two such molecules, namely $Co(acac)_3$ and $Cr(acac)_3$, were investigated. The results illustrate the established principles of how the symmetry and structure of the adsorbed molecules are crucial for the magnetic properties and spin stability.

The last project is devoted to a special class of magnetic molecules, the so-called spin crossover molecules [26]. These molecules stand out by the fact that they occur in two different states. The first one is a paramagnetic state, where the molecules exhibit a finite magnetic moment, while they are non-magnetic in the other state. Regarding technical application, these kinds of molecules are particularly interesting because the transition between the two states may be initiated by various external triggers such as temperature, pressure or light illumination [26]. In this project, spin crossover molecules adsorbed on ferromagnetic substrates were investigated, where again the molecule-substrate interaction takes the center

stage. It was supposed to be explored, whether the molecules exhibit a magnetic exchange interaction with the substrate and in the same time maintain their switching ability. For such a material system exciting application such as writing magnetic structures with light are conceivable. For this purpose, two such systems were investigated in the framework of this thesis. Firstly, Fe(1,10-phenanthroline)$_2$(NCS)$_2$ molecules (Fe-Phen) on one monolayer of iron nitride were examined using scanning tunneling microscopy. Secondly, Fe$\{[Me_2Pyrz]_3BH\}_2$ molecules (Fe-Pyrz) on thin films of lanthanum strontium manganate were studied using magneto-optic Kerr effect measurements and x-ray absorption spectroscopy and magnetic circular dichroism.

The thesis is structured as follows. First, in the upcoming chapter 2 the experimental and theoretical background is discussed elaborately. This includes on the one hand the experimental techniques that were used in this work, namely scanning tunneling microscopy, magneto-optic Kerr effect measurements and x-ray absorption spectroscopy. On the other hand, the quantum mechanical basics of SMMs and molecule interactions with metallic substrates, including lifetime broadening and the Kondo effect, are discussed elaborately. Then, chapter 3 gives a detailed description of the experimental setups and methods. The subsequent chapters 4, 5 and 6 present the results that were achieved in the framework of this dissertation. Therein, the beginning of each chapter contains an elaborate motivation of the respective project and a review on previous reports on the subject. Finally, chapter 7 gives a summary of the results and presents an outlook on future application and research.

2 Theoretical and Experimental Background

This chapter gives an introduction to the basics of the quantum mechanical description of single magnetic molecules and the experimental techniques that were used in the framework of this dissertation. Thereby, the first section introduces scanning tunneling microscopy (STM) describing the theoretical treatment of quantum tunneling and depicting common techniques like scanning tunneling spectroscopy (STS), inelastic electron tunneling spectroscopy (IETS) and spin-polarized measurements. Thereafter, the interaction between molecules and metal substrates and tunneling processes through molecules will be discussed. The third section gives a short introduction to magnetic interactions and the Kondo effect, which will be crucial for the stability of single spins on surfaces. Then, the fourth section introduces the basic concepts of single-molecule magnets (SMM) including crystal field theory (CFT), zero field splitting (ZFS) and quantum tunneling of magnetization (QTM) and finally deals with the special case of spin crossover complexes (SCO). Finally, the last sections deal with x-ray absorption spectroscopy (XAS) and x-ray magnetic circular dichroism (XMCD) as an element specific means to determine orbital and spin angular momentum, and the magneto-optic Kerr effect (MOKE).

2.1 Scanning Tunneling Microscopy and Quantum Tunneling

2.1.1 Scanning Tunneling Microscopy

The basic idea of scanning tunneling micropscopy (STM) is to scan a sample surface with a very sharp metallic tip as a probe [23, 27]. Applying a bias voltage between the sample and the tip, one can detect a small current when the tip-sample distance is of the order of a few Å, even when tip and sample are not in mechanical contact. This current is attributed to the quantum mechanical effect of *quantum tunneling*. This tunneling current turns out to be very susceptible to changes in the tip-sample distance and as will be discussed more elaborately in the following section, it depends crucially on the electronic structure of the sample.
The idea is now to scan the sample surface laterally (x-y-plane) while in the same time the tip height (z-position) is adjusted such that the tunneling current remains constant during the scan as illustrated in figure 2.1. Usually this is achieved by a feedback loop. The resulting image is the height profile $z(x,y)$ where both, the electronic structure of the sample and the actual topography can account for a contrast. If not stated otherwise, all the STM images shown in this work were measured in the this *constant-current mode*. Alternatively, one can just measure the tunneling current $I_\mathrm{T}(x,y)\big|_{z=\mathrm{const}}$ as function of the lateral position with constant tip height, which is called *constant-height mode*. Thereby, the (x,y,z)-positioning of the tip is realized by using piezoelectrics. These materials have the property to change their dimensions when an electric field is applied. Typically the tip is mounted on top of a piezoelectric tube [28], that readily allows for picometer precision in all three dimensions. Therefore, a scanning tunneling microscope (STM) not only allows for imaging single molecules and atoms on surfaces, but also permits to contact them or perform spectroscopy measurements. The latter usually is referred to as scanning tunneling spectroscopy (STS), where one measures the $I(V)$-characteristics at a fixed tip position. As will be elaborated in following sections, this can give deep insights in the electronic and even magnetic structure of the atom, molecule or substrate examined. Combining both, sub-nanometer spatial resolution with an energy resolution

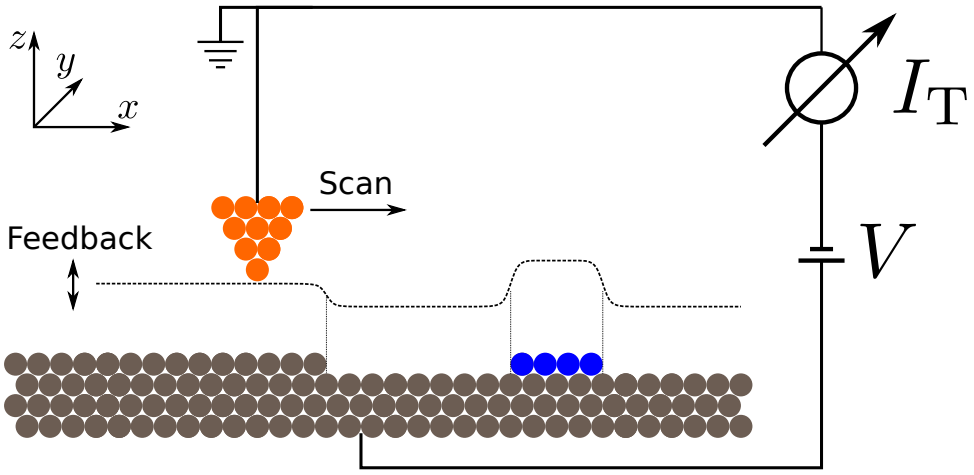

Figure 2.1: Constant current mode. A feedback loop adjusts the tip-sample distance during the scan, such that the tunneling current remains constant. Both, the actual topography and the electronic structure account for a contrast.

in spectroscopy down to $\mathcal{O}(20\,\mu eV)$ at mK temperatures, makes STM a unique tool in nano-analysis.

2.1.2 Models for Quantum Tunneling

In order to provide a decent understanding of what is actually probed in STM, one first has to get a grasp on the physics of quantum tunneling. The most straightforward approach towards tunneling is a one-dimensional model of a single particle with energy ϵ in front of a rectangular potential barrier V_0 [29, 30], which is illustrated in figure 2.2a. This problem can be described by the one-dimensional time-independent Schroedinger equation

$$\left(\frac{-\hbar^2}{2m}\frac{\mathrm{d}^2}{\mathrm{d}z^2} + V(z)\right)\,\psi(z) \;=\; \epsilon\,\psi(z)\;. \tag{2.1}$$

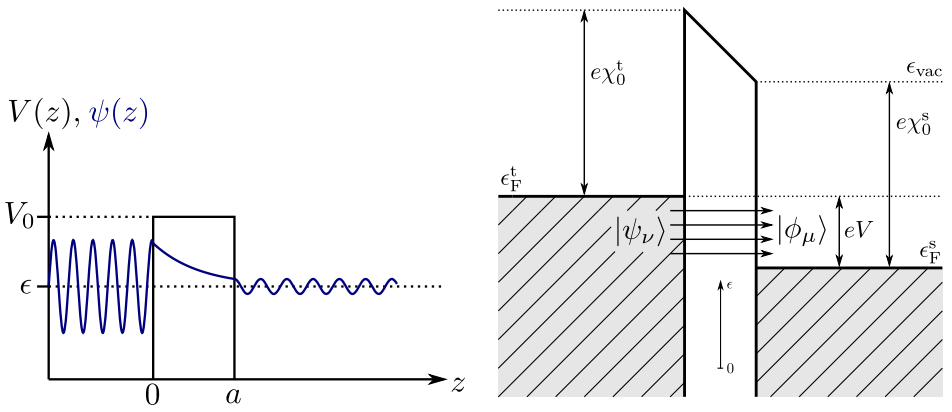

(a) 1-dimensional tunneling model **(b)** Bardeen model

Figure 2.2: Models for quantum tunneling.

The solution for a particle initially propagating along the positive z-direction is given by

$$\psi \propto \begin{cases} \mathrm{e}^{\mathrm{i}k\cdot z} + r \cdot \mathrm{e}^{-\mathrm{i}k\cdot z} & , \; z < 0 \\ b_1 \cdot \mathrm{e}^{\kappa\cdot z} + b_2 \cdot \mathrm{e}^{-\kappa\cdot z} & , \; 0 \leq z < a \\ t \cdot \mathrm{e}^{\mathrm{i}k\cdot z} & , \; z > a \end{cases} \tag{2.2}$$

with the wave vector $k = \sqrt{\frac{2m\epsilon}{\hbar^2}}$ and $\kappa = \sqrt{\frac{2m(V_0-\epsilon)}{\hbar^2}}$. The coefficients r and t are the amplitudes for the particle being reflected or transmitted through the barrier, respectively. Assuming that both the wave function and its spatial derivative are continuous, the transmission probability T is given by [29, 30]

$$T \;=\; |t|^2 = \left(1 + \left(\frac{k^2+\kappa^2}{2k\kappa}\right)^2 \sinh^2(\kappa a)\right)^{-1}, \tag{2.3}$$

which yields for the tunneling current [27]

$$I_{\mathrm{T}} \;\propto\; T \;\approx\; \mathrm{e}^{-2\kappa a}. \tag{2.4}$$

Note, that this simple model already predicts that the tunneling current is supposed to decline exponentially with the width of the tunneling barrier a, which can be observed in plenty of experiments including STM [31], mechanically controlled break junctions [32] or even planar tunnel junctions

[33]. Typically, κ is of the order of $1\,\text{Å}^{-1}$ such that the tunneling current drops by one order of magnitude as the tip-sample distance increases by 1 Å [27]. An improvement of this model was given independenly by Wentzel, Kramers and Brillouin [29, 34] (so-called WKB approximation), which is also applicable for non-rectangular barriers.

Note, that these models neglect the band structures of both, the STM tip and the sample, and the fermion properties of electrons, namely the Pauli exclusion principle. According to the latter an electron is only allowed to tunnel from an occupied tip (sample) state into an unoccupied sample (tip) state. Thereby, the occupation probability at a certain temperature is given by the Fermi-Dirac distribution $f(\epsilon)$. A more advanced model that takes into account both of these issues is therefore given by the Bardeen-model [35], which is illustrated in figure 2.2b. Here, the Fermi levels of tip and sample ($\epsilon_\text{F}^{\text{t/s}}$) are separated by the tunneling voltage and transitions from tip states ψ_ν to sample states φ_μ (and vice versa) are treated via Fermi's golden rule. Thus, the tunneling current yields

$$I_\text{T} \;=\; \frac{4\pi e}{\hbar} \sum_{\nu,\mu} |\underbrace{\langle \psi_\nu | \mathcal{H}^\text{int} | \varphi_\mu \rangle}_{\equiv\, M}|^2 \, \delta(\epsilon_\nu - \epsilon_\mu) \, \left(f(\epsilon_\nu - \epsilon_\text{F}^\text{t}) - f(\epsilon_\mu - \epsilon_\text{F}^\text{s}) \right) , \quad (2.5)$$

which may be written in a more convenient way introducing the respective densities of states $\rho^{\text{t/s}}(\epsilon)$ of tip and sample:

$$I_\text{T} \;=\; \frac{4\pi e}{\hbar} \int \text{d}\epsilon \; \rho^\text{t}(\epsilon) \; \rho^\text{s}(\epsilon) \; \left(f(\epsilon - \epsilon_\text{F}^\text{t}) - f(\epsilon - \epsilon_\text{F}^\text{s}) \right) \; |M|^2 \, . \quad (2.6)$$

This result is still rather inconvenient considering the transition matrix elements might in generel have a complicated energy dependence. Tersoff and Hamann therefore proposed a model in which they assume that the tip wave function can be described as a spherical symmetric s-wave [27, 36]. Therein, in the limit of low temperatures ($T \to 0$) and assuming a rarther flat tip density of states around the Fermi level, the tunneling current can be expressed as

$$I_\text{T} \;\propto\; \int_{\epsilon_\text{F}^\text{s}}^{\epsilon_\text{F}^\text{s}+eV} \text{d}\epsilon \;\; \rho^\text{s}(\epsilon) \; |\phi(\boldsymbol{r_0})|^2 \, . \quad (2.7)$$

The integrand is usually referred to as the *local density of states (LDOS)*, where $\boldsymbol{r_0}$ is the lateral tip position. The tunneling current hence depends strongly on the electronic structure of the investigated sample, which is why STM allows to probe the electronic properties of sample surfaces.

2.1.3 Differential Conductance

Equation 2.7 implies that the differential conductance, i.e. the derivative of the tunneling current with respect to the bias voltage, is proportional to the LDOS of the sample:

$$\left.\frac{\mathrm{d}I}{\mathrm{d}V}\right|_{V=V_0} \propto |\phi(\boldsymbol{r_0})|^2\, \rho^{\mathrm{s}}(\epsilon_{\mathrm{F}}^{\mathrm{s}} + eV_0)\ . \tag{2.8}$$

In principle, this allows to probe the LDOS around the Fermi level by just recording the tunneling current while sweeping the bias with the tip position fixed and calculating the numerical derivative of this so-called $I-V$-spectrum. A much more convenient way, however, is to directly measure the derivative using a lock-in amplifier. Thereby, a small AC voltage (with a frequency ν that is of the order of $\mathcal{O}(1\,\mathrm{kHz})$) is added to the tunneling voltage. Meanwhile, the resulting tunneling current is demodulated at the same frequency ν. It is easy to see that this demodulated signal is at least up to the second order proportional to the first derivative of the tunneling current:

$$\begin{aligned} I(V_0 + \bar{V}\sin(2\pi\nu t)) = I(V_0)\ &+\ \left.\frac{\mathrm{d}I}{\mathrm{d}V}\right|_{V_0} \bar{V}\sin(2\pi\nu t) \\ &+\ \frac{1}{2}\left.\frac{\mathrm{d}^2 I}{\mathrm{d}V^2}\right|_{V_0} \bar{V}^2\sin^2(2\pi\nu t) + \mathcal{O}(\bar{V}^3)\ . \end{aligned} \tag{2.9}$$

The reason for using a lock-in amplifier is that one gets a much better signal to noise ratio (SNR) due to so-called *flicker noise* ($1/f$-noise) [37]. Note, that the tunneling junction in general exhibits a finite capacitance and accordingly a finite AC impedance, which will cause an additional contribution to the lock-in signal. However, since this contribution is typically independent of the DC bias voltage, it can easily be removed by setting the lock-in phase properly. Usually this is achieved by setting the phase such that there is no

lock-in signal detectable, when the STM tip is withdrawn just out of the tunneling regime.

However, using a lock-in amplifier comes at a price, i.e. a lower energy resolution: By applying the modulation one adds uncertainty to the tunneling voltage, and hence to the energy of the tunneling electrons. Other parameters that limit the energy resolution in STS are voltage noise and the experiment temperature. The latter can be attributed to the temperature smearing of the Fermi levels of tip and sample, which is given by the Fermi functions in equation 2.6. Accordingly, the temperature-broadened differential conductance will result in a convolution of the LDOS with the derivative of a Fermi function. Since the latter exhibits a width of the order of $\mathcal{O}(k_\mathrm{B}T)$, the best energy resolution is of this order of magnitude. This, actually, is the most important reason for performing all experiments at low temperatures.
Analytically, one can derive an expression for the energy resolution for the differential conductance [38] which reads

$$\Delta\epsilon = \sqrt{(2e\bar{V}_\mathrm{RMS})^2 + (3.2\ k_\mathrm{B}T)^2}, \tag{2.10}$$

where $\bar{V}_\mathrm{RMS} = \bar{V}/\sqrt{2}$ is the root mean square of the lock-in modulation. As a common figure of merrit for the energy resolution of a specific setup, it is convenient to use the so-called *electronic temperature*, which is an effective temperature that accounts for all the broadening effects.

2.1.4 Inelastic Tunneling

So far, all the presented models for quantum tunneling only consider elastic tunneling, i.e. processes by which electrons have the very same energy before and after the tunneling process. What can happen though, is that an electron can sacrifice some of its energy to excite an inelastic excitation, if the tunneling energy (eV) is larger than the excitation energy ($\hbar\omega_0$). Such a process is illustrated in figure 2.3a. Such inelastic excitations can be phonons or other vibrational modes [39, 40], magnons [41], or even spin-flip inelastic excitations [42, 43].

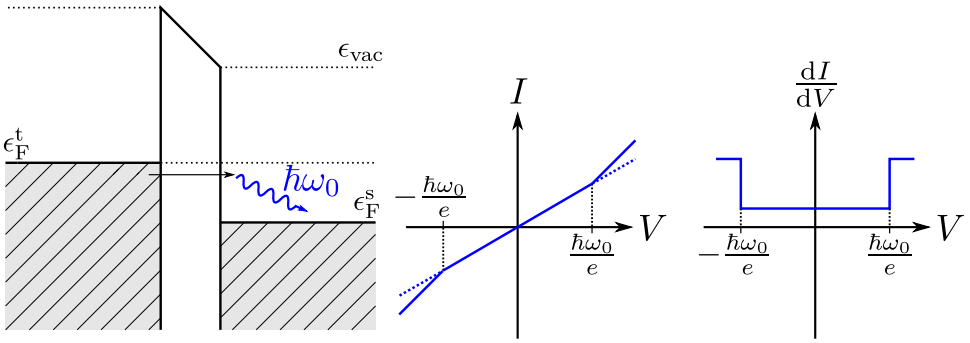

(a) Inelastic tunneling process **(b)** I-V characteristics of an inelastic excitation

Figure 2.3: Scheme of an inelastic tunneling process and the corresponding spectroscopic features.

Such an inelastic process yields an additional tunneling channel, which is why the tunneling probability and thus the tunneling current are enhanced above the threshold voltage. The result is a pair of kinks in the I-V-curve or a pair of steps in the differential conductance as illustrated in figure 2.3b. This technique is usually referred to as *inelastic electron tunneling spectroscopy* (IETS).
It should be mentioned, that it is very common to also measure the second derivative of the current with respect to bias, where an inelastic excitation features a peak-dip pair. However, it usually requires rather high tunneling currents in order to get a sufficiently high signal in the second derivative. Some molecules, however, tend to move, jump to the tip or even disintegrate when the tunneling current is too high. Therefore, the second derivative was not measured in this work.

2.1.5 Tunneling Magnetoresistance and Spin-Polarized STM

So far, using scanning tunneling microscopy to investigate both structural and electronic properties of a given sample surface, has been discussed very elaborately. An extension of this technique, that additionally enables one to probe the magnetic properties is the so-called *spin-polarized scanning tunneling microscopy* (sp-STM) [44]. Therein, the so-called *tunneling*

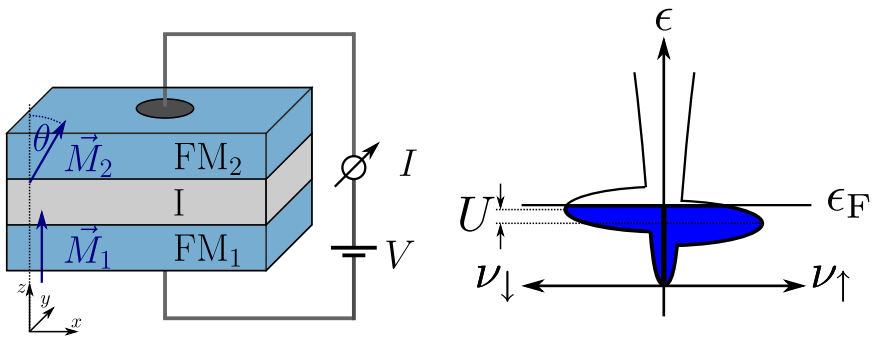

(a) Spin valve **(b)** Stoner model

Figure 2.4: Structure of a spin valve and spin-split DOS of the Stoner model for ferromagnetism. (a) With magnetization $\boldsymbol{M}_1$ being fixed, the conductance of the junction depends on the orientation of $\boldsymbol{M}_2$ given by the relative angle θ. (b) The spin-split DOS of the Stoner model for ferromagnetism for a simplified bandstructure. A net magnetization occurs because more spin up states are occupied (*majority spin*). In this example, the DOS at ϵ_F is higher for the opposite spin orientation. Both cases, though, $\nu_\uparrow(\epsilon_\mathrm{F}) \gtrless \nu_\downarrow(\epsilon_\mathrm{F})$ are possible, depending only on the band structure.

magnetoresistance effect (TMR) is exploited: Regarding a tunnel junction consisting of two ferromagnetic metals separated by a thin insulating layer as is depicted in figure 2.4a, the conductance through the junction depends directly on the relative orientation of the magnetizations. Thus, such a structure is usually referred to as magnetic valve or *spin valve*. This effect could first be observed in a layered structure of Fe/Ge/Co [45]. Julliere observed, that the conductance at low bias was very different for the cases of Fe and Co being magnetized either parallel or antiparallel.

This observation is easy to understand qualitatively within the framework of the Stoner model for itinerant ferromagnetism [46]. Therein, the 3d bands for spin up and down are split by the exchange parameter U, due to the exchange interaction (figure 2.4b). The result is - besides a net magnetization due to the different amounts of spin up and down electrons - also a spin polarization of the density of states (DOS) near the Fermi edge. The latter simply means, that there are more electrons of one spin orientation than the other near the Fermi edge, hence $\nu_\uparrow(\epsilon_\mathrm{F}) \neq \nu_\downarrow(\epsilon_\mathrm{F})$. It should be pointed out that for a given magnetization with majority spin up, both cases

$\nu_\uparrow(\epsilon_F) \gtrless \nu_\downarrow(\epsilon_F)$ can occur. This naturally depends on the ferromagnetic material and its band structure.
Figure 2.5 illustrates how the TMR effect can be understood in this picture. For small bias voltages and for elastic tunneling processes, where the electron spin is conserved, electrons can only tunnel from an occupied spin up (spin down) state of FM_1 to an unoccupied state of the same spin orientation of FM_2. Assuming that both ferromagnetic leads are made of the same material, it is plain that the sum of the two respective overlapps between $\left(\nu_\uparrow^{(1)}(\epsilon_F)\right.$ and $\left.\nu_\uparrow^{(2)}(\epsilon_F)\right)$ and between $\left(\left(\nu_\downarrow^{(1)}(\epsilon_F)\right.\right.$ and $\left.\left.\nu_\downarrow^{(2)}(\epsilon_F)\right)\right.$ and accordingly the tunneling current is largest for parallel orientations and lowest for antiparallel orientations. Accordingly, for a spin valve one can think of the first and second ferromagnet-insulator interface as a spin polarizer and a spin analyzer, respectively, where excess electrons of a certain spin orientations are reflected.

A more general consideration of this problem gives the following relation for the conductance [47]

$$G(\theta) = G_0 \left(1 + \sigma_1 \sigma_2 \cos(\theta)\right). \tag{2.11}$$

Here, θ is the relativ angle between the two magnetizations and $\sigma_{1/2}$ are the spin-polarizations for interface 1 and 2, respectively.

This concept now can be transferred easily to STM. In the most straightforward approach to sp-STM, a ferromagnetic material is used as tip material [48]. Analogue to the spin valve case, the tunneling current is then spin-polarized. For a magnetic sample, the tunnel conductance is then higher (lower) for the tip being located above a site of the same (the opposite) spin polarization. Therefore a spin contrast can occur for both topography and spectroscopy. Generally, this enables for instance imaging magnetic domains and domain walls [49], magnetic textures [50] or spin-polarized spectroscopy [51].

The easiest way to get an STM tip with spin polarization is to coat a non-magnetic tip with a ferromagnetic film [51]. Depending on the material and the layer thickness this can lead to a tip magnetization parallel (*in plane*) or perpendicular (*out of plane*) with respect to the sample surface or

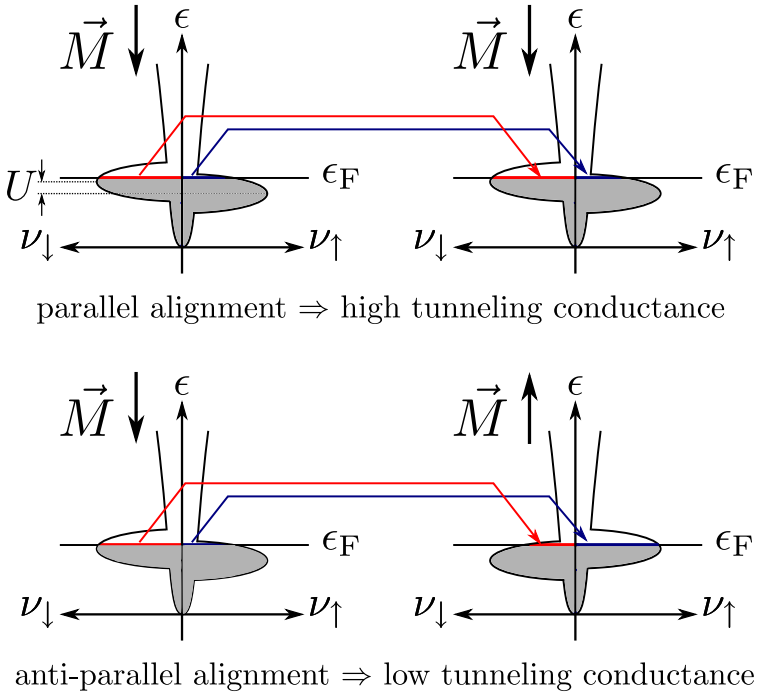

Figure 2.5: Tunneling Magnetoresistance. Assuming elastic tunneling only, the spin state of an electron is not changing during the tunneling process. Hence, the tunneling conductance is higher when the two ferromagnetic leads are aligned parallel.

something in between. From equation 2.11 it follows, that a spin contrast can only be observed, when the magnetization has a finite component parallel to the sample magnetization. Typical examples are iron coating for in plane and cobalt coating for out of plane contrast, respectively.
One crucial difficulty for this approach, however, is the magnetic stray-field that arises from the tip. This field can alter or polarize a soft magnetic sample that is supposed to be investigated [51]. As a solution to this problem, the use of antiferromagnets as tip material has been established [52]. An antiferromagnet does not exhibit a stray field, while it may still feature a spin polarization of the DOS. For this purpose, either antiferromagnetic thin films like chromium can be deposited on a non-magnetic tip [52] or even bulk antiferromagnetic tips can be used [53, 54].

Often during a measurement it is not directly obvious whether an observed effect or contrast is indeed of magnetic origin, or whether it is merely an electronic or structural feature [55]. Oftentimes, a direct comparison to a measurement with non-magnetic tip or a measurement of the effect as function of an external magnetic field may get things straight. In a more sophisticated extension of this method, a ferromagnetic ring containing a wound coil was used as STM tip [56, 57]. By high frequency reversal of the tip magnetization, the topography and spin signal could be recorded separately at the same time.

2.2 Molecule-Substrate Interaction and Lifetime Broadening

In the previous section quantum tunneling through a vacuum barrier was discussed elaborately. The objective of this work however, is to investigate single molecules adsorbed on a metal surface. Thus, in this context the question arises, how an adsorbed molecule in between the tip and substrate - or in between two metal leads in case of a break junction - can influence the tunneling process. For a start one could think of a simple model as it is shown in figure 2.6a: The molecule has discrete molecular orbitals, that are aligned energetically such that the substrate Fermi level is in between HOMO (*highest occupied molecular orbital*) and LUMO (*lowest unoccupied molecular orbital*). Applying a sufficiently high bias voltage between the two leads of the junction, additionally to the regular tunneling current, electrons can hop sequentially from the tip to an unoccupied MO below the Fermi level and subsequently to the substrate, as illustrated in figure 2.6b. The problem of this picture is however, that the molecule could only influence the tunneling process at sufficiently high tunneling voltage. As a consequence, at bias voltages smaller than the difference between Fermi level and HOMO/LUMO, one could not detect the molecule in STM at all. Luckily, though, this is not the case. The crucial point that was neglected in this picture is the electronic coupling between the molecule and substrate: Bringing a molecule in contact with a metallic surface results in overlaps of the molecular orbitals and the metallic states. Thus, it is possible for

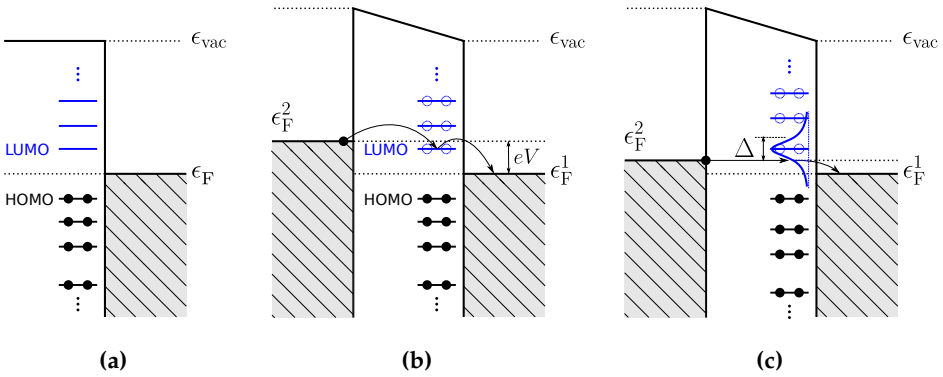

Figure 2.6: Energy landscapes for a molecule adsorbed on a metallic surface. (a) The molecular orbitals are sharp without molecule-substrate interaction. (b) In this model, in an STM experiment hopping from the tip to an unoccupied molecular state and subsequently to the substrate can occur provided the bias voltage is large enough. (c) The lifetime broadening is shown for the LUMO. Here, hopping to the LUMO is possible already at small bias.

electrons near the Fermi level to hop from substrate to molecule and vice versa. Illustratively, this yields a finite lifetime τ for the molecular states. From the uncertainty principle it follows, that such processes are possible within an energy interval of

$$\delta\epsilon \sim \frac{\hbar}{\tau}. \tag{2.12}$$

Effectively, the molecular orbitals are not infinitely sharp anymore but broadened, which is usually referred to as *lifetime broadening*. This broadening is the reason, why adsorbed molecules can already be detected at small tunneling voltages. This is illustrated in figure 2.6c. Additionally to the broadening, also energy shifts of molecular orbitals may occur due to mirror charging and screening effects.

A very simple theoretical description of this effect was given by Newns in the so-called *Anderson-Newns* model for chemiosorption [58, 59, 60]. This modell describes the coupling of an adsorbate or molecule with a single

state $|M\rangle$ to a metallic substrate with eigenstates $|\boldsymbol{k}\rangle$. For this the initial point is the following Hamiltonian

$$\hat{\mathcal{H}} = \underbrace{\epsilon_M \hat{c}_M^\dagger \hat{c}_M}_{\text{molecule}} + \underbrace{\sum_{\boldsymbol{k}} \epsilon_{\boldsymbol{k}} \hat{c}_{\boldsymbol{k}}^\dagger \hat{c}_{\boldsymbol{k}}}_{\text{substrate}} + \underbrace{\sum_{\boldsymbol{k}} \left(V_{M,\boldsymbol{k}} \hat{c}_M^\dagger \hat{c}_{\boldsymbol{k}} + \text{h.c.} \right)}_{\text{molecule-substrate coupling}}, \tag{2.13}$$

where the last term corresponds to a tight-binding-like coupling between the substrate states and the molecule. With this model the local density of states at the molecule ρ_{Mol}, which is given by the expression

$$\rho_{\text{Mol}}(\epsilon) = \sum_n |\langle n|M\rangle|^2 \delta(\epsilon - \epsilon_n), \tag{2.14}$$

was calculated. Here, $|n\rangle$ are the eigenstates of the complete Hamiltonian of equation 2.13. Newns could show, that

$$\rho_{\text{Mol}}(\epsilon) = \frac{1}{\pi} \frac{\Delta^2(\epsilon)}{(\epsilon - \epsilon_M - \Lambda(\epsilon))^2 + \Delta^2(\epsilon)}, \tag{2.15}$$

with

$$\Delta(\epsilon) = \pi \sum_{\boldsymbol{k}} |V_{M,\boldsymbol{k}}|^2 \delta(\epsilon - \epsilon_{\boldsymbol{k}}), \quad \Lambda(\epsilon) = \frac{1}{\pi} \mathcal{P} \int_{-\infty}^{\infty} \frac{\Delta(\epsilon')\mathrm{d}\epsilon'}{\epsilon - \epsilon'}, \tag{2.16}$$

where $\mathcal{P}$ denotes the principle value of the integral.
This rather general result can most easily be understood in the limit, where the substrate density of states only varies insignificantly in an energy interval larger than the matrix elements $|V_{M,\boldsymbol{k}}|$ around ϵ_M. In this case $\Delta(\epsilon)$ should be almost constant. It is straightforward to show that Λ vanishes in this case. Accordingly, the density of states at the molecule ρ_{Mol} will simply be a Lorentzian centered at ϵ_M with width Δ. Thus, this limit is exactly the lifetime broadening from the beginning of this section.

The STM tip, or alternatively the second electrode of a break junction, will have the same effect on the molecular states. However, in case of STM, the coupling to the tip will be significantly weaker than the molecule-substrate interaction. A corresponding model is presented in reference [61]. There the coupling of a single localized state to two electrodes (1/2) is

treated analogous with a tight-binding approach with hopping parameters $t_{1/2}$. Again the local density of states results in a Lorentzian, where the width Γ is simply given by the sum of the two contributions $\Gamma_{1/2}$ of the two electrodes. Meanwhile, the $\Gamma_{1/2}$ are proportional to the squares of the hopping parameters $|t_{1/2}|^2$.

Generally, this molecule-substrate interaction can have dramatic effects. Molecular properties may change upon adsorption and certain functionalities of a molecule may be quenched on a metallic substrate. This issue will be discussed more elaborately in chapter 6 for the example of spin crossover molecules.

2.3 Magnetic Interactions and the Kondo Effect

The emergence of magnetic order and remanent magnetism of solids relies utterly on the interaction of magnetic moments. When there are no interactions between the magnetic moments of the solid, the single moments are independent and can only be aligned by an external magnetic field. The net magnetization can easily be calculated as a thermal expectation value and is given by the *Brillouin function* [46, 62]. Though, in the absence of an external magnetic field the moments are aligned randomly and the remament magnetization is zero. The result is a paramagnet. Therefore, in a ferromagnet, it must be somehow energetically favorable for a magnetic moments to be aligned in the same direction as a neighboring moment. One could naively think, that the origin of this is simply a classical dipole-dipole interaction, where one magnetic moments minimizes its energy by aligning in the magnetic stray field of another moment. However, a rough estimation of the energy scale of such an interaction for two magnetic moments $\mu \sim \mu_B$ at a distance $r \sim 1$ Å yields only a few µeV. Therefore, such an interaction can hardly account for Curie temperatures of the order of 1000 K as it is found in many ferromagnetic compounds [46]. The underlying interaction is the so-called *exchange interaction* that was first described by Heisenberg in order to describe the term diagram of helium [63]. The underlying idea of this magnetic interaction will be discussed in the following section. There-

with, the Kondo effect, which will be crucial for the stability of atomic magnetic moments on surfaces, and its detection in STS will be explained.

2.3.1 Exchange Interaction

The exchange interaction is a result of Pauli's principle and the Coulomb repulsion. The easiest approach is to consider a system of two electrons in a solid or an atom with spin $\hat{\boldsymbol{s}}_1$ and $\hat{\boldsymbol{s}}_2$ that is described by the Hamiltonian $\hat{\mathcal{H}}$ [46, 62]. Since the two electrons are indistinguishable, the corresponding two particle wave function must be antisymmetric when exchanging the two electrons. Assuming the wave function can be written as a product of a spatial wave function $\phi(\boldsymbol{r}_1, \boldsymbol{r}_2)$ and a spin wave function χ

$$\psi_{\mathrm{S/T}} = \phi_{\mathrm{S/T}}(\boldsymbol{r}_1, \boldsymbol{r}_2) \otimes \chi_{\mathrm{S/T}}, \tag{2.17}$$

yields two possibilities: A symmetric spatial wave function with an antisymmetric spin wave function (singlet) or vice versa (triplet):

$$\begin{aligned} \phi_{\mathrm{S}}(\boldsymbol{r}_1, \boldsymbol{r}_2) &= +\phi_{\mathrm{S}}(\boldsymbol{r}_2, \boldsymbol{r}_1), \quad \chi_{\mathrm{S}} = \frac{1}{\sqrt{2}}\left(|\uparrow,\downarrow\rangle - |\downarrow,\uparrow\rangle\right) \\ \phi_{\mathrm{T}}(\boldsymbol{r}_1, \boldsymbol{r}_2) &= -\phi_{\mathrm{T}}(\boldsymbol{r}_2, \boldsymbol{r}_1), \quad \chi_{\mathrm{T}} = \left\{ |\uparrow,\uparrow\rangle \; ; \; \frac{1}{\sqrt{2}}\left(|\uparrow,\downarrow\rangle + |\downarrow,\uparrow\rangle\right) \; ; \; |\downarrow,\downarrow\rangle \right\}. \end{aligned} \tag{2.18}$$

Thereby, the respective energy values read

$$\epsilon_{\mathrm{S/T}} = \int \mathrm{d}^3 r_1 \int \mathrm{d}^3 r_2 \; \phi^*_{\mathrm{S/T}} \; \hat{\mathcal{H}} \; \phi_{\mathrm{S/T}}. \tag{2.19}$$

It's straightforward to show that

$$\langle \hat{\boldsymbol{s}}_1 \cdot \hat{\boldsymbol{s}}_2 \rangle = \begin{cases} -3/4, \text{ singlet} \\ +1/4, \text{ triplet} \end{cases}, \tag{2.20}$$

such that the Hamiltonian can be expressed as

$$\hat{\mathcal{H}} = -\underbrace{(\epsilon_{\mathrm{S}} - \epsilon_{\mathrm{T}})}_{\equiv \mathcal{J}} \; \hat{\boldsymbol{s}}_1 \cdot \hat{\boldsymbol{s}}_2 + \text{const} \tag{2.21}$$

with $\mathcal{J}$ beeing referred to as *exchange integral* or *exchange constant*. For $\mathcal{J} > 0$ ($\mathcal{J} < 0$) the triplet (singlet) state is energetically favored and the

exchange is called *ferromagnetic* (*antiferromagnetic*). It should be stressed, that the Hamiltonian in equation 2.21 is an expression of the Coulomb interaction of the two electrons with the cystal and each other. Usually, this result is generalized for larger spins or angular momenta and one writes:

$$\hat{\mathcal{H}}_{\mathrm{E}x} \;=\; -\mathcal{J}\;\hat{\boldsymbol{J}}_{\mathbf{1}} \cdot \hat{\boldsymbol{J}}_{\mathbf{2}}. \tag{2.22}$$

In addition to magnetic order and remanence, this exchange interaction is also important for spin-flip scattering processes in solids: Introducing the ladder operators

$$\hat{J}_{\pm} = \hat{J}_x \pm \mathrm{i}\hat{J}_y, \tag{2.23}$$

one can write the Hamiltonian as

$$\hat{\mathcal{H}}_{\mathrm{Ex}} \propto \hat{\boldsymbol{J}}_1 \cdot \hat{\boldsymbol{J}}_2 = \hat{J}_{1,z}\hat{J}_{2,z} + 1/2\left(\hat{J}_{1,+}\hat{J}_{2,-} + \hat{J}_{1,-}\hat{J}_{2,+}\right). \tag{2.24}$$

From this one can easily see, that via this exchange interaction one spin can transfer $1\hbar$ of angular momentum to another spin. Applying this result to a localized impurity spin in a non-magnetic metal, where the conduction electrons close to the Fermi surface can be scattered by the impurity via exchange interaction, will result in the Kondo effect. This phenomenon and its consequences will be discussed in the following section 2.3.2.

2.3.2 Kondo Effect

Historically the Kondo effect was first observed upon measuring the resistance of a non-magnetic metal at low temperatures. The resistance is expected to steadily decrease upon decreasing the temperature and in case the metal is no superconductor its behavior should follow

$$\rho(T) \;=\; a \;+\; b\;T^2 \;+\; c\;T^5. \tag{2.25}$$

Therein, the first term is a temperature-independent contribution related to electrons being scattered by non-magnetic impurities. The second term is due to electron-electron interaction and can be derived from Fermi liquid theory [64]. The third term is the Bloch-Grüneisen law for electron-phonon scattering [65, 66].
Surprisingly, a resistance minimum was found for many metals, for instance

gold [67], such that when cooling the sample below a characteristic temperature its resistance increases again.
Eventually, Kondo could provide a theoretical description of this effect. In his model, he explained the origin of this effect by the conduction electrons being scattered elastically by magnetic impurities [68]. Therein, he treated the scattering as a perturbation using the the so-called *sd-Hamiltonian* [69]

$$\hat{\mathcal{H}}_{sd} = \sum_{k,k'} \mathcal{J}_{k,k'} \left(\hat{S}_+ \hat{c}^\dagger_{k,\downarrow} \hat{c}_{k',\uparrow} + \hat{S}_- \hat{c}^\dagger_{k,\uparrow} \hat{c}_{k',\downarrow} + \hat{S}_z \left(\hat{c}^\dagger_{k,\uparrow} \hat{c}_{k',\uparrow} - \hat{c}^\dagger_{k,\downarrow} \hat{c}_{k',\downarrow} \right) \right), \quad (2.26)$$

where $S_\pm$ are the ladder operators of the magnetic impurity and the $\hat{c}_{q,\sigma}$ ($\hat{c}^\dagger_{q,\sigma}$) are the annihilation (creation) operators for a conduction electron with momentum q and spin σ. This Hamiltonian looks simply like a second quantization version of the Heisenberg exchange of equation 2.24. The first two terms describe spin-flip processes, where a conduction electron transfers $\pm 1\hbar$ to the impurity spin, while the third term describes a scattering process where spins are conserved. This s-d-interaction was first phenomenologically proposed by Zener [70, 71]. The corresponding Hamiltonian of equation 2.26 could be derived later in a more general form by Anderson from first principles in the so-called *Anderson impurity model* [69, 72]. Using third order perturbation theory, Kondo was able to derive an additional contribution to the resistivity of the form

$$\rho_K \propto \log\left(T/T^*\right) \quad (2.27)$$

that could explain the resistivity minimum in case of a negative exchange constant, i.e. an antiferromagnetic exchange. However, this result still had the problem of the logarithmic divergence at zero temperature. This so-called *Kondo problem* emerges because at very low temperatures compared to a characteristic temperature scale T_K - the so-called *Kondo temperature* - the perturbation terms of higher order become large, such that eventually perturbation theory breaks down. What happens physically is, that due to continuous spin-flip scattering of the conduction electrons with the magnetic impurity, at temperatures $T \ll T_K$ a new non-magnetic, many-body singlet ground state arises. This state can be regarded as a kind of bound state, where the magnetic moment of the impurity is effectively screened by the conduction electrons of the metal host. This limit, hence, cannot be described by perturbation theory anymore, but by alternative approaches

like the renormalization group formalism by Wilson [73].

Certainly, the Kondo effect plays a special role for this work, where single magnetic molecules adsorbed on a metallic substrate were investigated. Thereby, the molecules naturally act as the magnetic impurities of the Kondo model. Interestingly, the aforementioned Kondo scattering causes an additional contribution to the DOS, the so-called *Kondo resonance*, which occurs at the Fermi level. This resonance can readily be detected in STS, and thus represents a characteristic signature of this Kondo effect.

2.3.3 Kondo Effect in Scanning Tunneling Spectroscopy

This section aims to discuss how the Kondo resonance looks like in an STS experiment and which model functions exist to describe a measured spectrum. The precise shape of this Kondo resonance depends first of all on the regarded temperature and coupling regime [74]. Thereby, the characteristic energy scale for the coupling strength is given by the Kondo temperature T_K. Usually two limit cases are distinguished.

The case $T \ll T_K$

In this so-called *strong-coupling regime* the DOS shows a typical resonance shape that can be described by a Lorentzian or more precisely by a Frota function [75, 76]. Meanwhile, the following discussion on how a corresponding tunneling spectrum will look like including the nomenclature, is based on this review article [77]. First it shall be assumed, that the Kondo resonance in the DOS can be described by a simple Lorentzian. Then, there are two possible paths for electrons tunneling elastically from tip to sample (or vice versa): First, the electrons can tunnel into unoccupied bulk states of the substrate (with amplitude t_1), or second, electrons can tunnel directly into the Kondo resonance (with amplitude t_2). Since both processes are elastic and coherent, interference effects have to be taken into account,

since the total tunneling probability is given by $|t_1 + t_2|^2$. The result is the *Fano-lineshape*

$$\frac{\mathrm{d}I}{\mathrm{d}V} \propto \frac{(\varepsilon + q)^2}{1 + \varepsilon^2}, \quad \text{with } \varepsilon = \frac{eV}{\Gamma}. \tag{2.28}$$

Therein, the Kondo temperature is given by the half width af half maximum

$$\Gamma = k_\mathrm{B} T_\mathrm{K} \tag{2.29}$$

which is a measure for the strength of the coupling of the localized magnetic moment to the conduction electrons of the substrate. The so-called *Fano factor* q depends mainly on the ratio of tunneling amplitudes t_2/t_1. The limit, where electrons preferably tunnel into the Kondo resonance, i.e. $t_2 \gg t_1$ ($q \gg 1$) results approximately in a Lorentzian peak. Conversely the opposite limit, where electron tunneling in empty bulk states is favored, i.e. $t_1 \gg t_2$ ($q \ll 1$), yields a Lorentzian dip. In between, the Fano lineshape shows an asymmetric shape, as is illustrated in figure 2.7a.

It should be noted, that the parameters q and Γ can be expressed in terms of the parameters of the Anderson single impurity model [72, 77]. Since those parameters are not used here, this simple phenomenological description shall be sufficient. Moreover, the width Γ of the Kondo resonance at finite temperatures is given by

$$2\Gamma = \sqrt{(2k_\mathrm{B}T_\mathrm{K})^2 + (\alpha k_\mathrm{B} T)^2}. \tag{2.30}$$

This increase of the Kondo resonance width can be related to the temperature smearing of the Fermi distribution. A Fermi-liquid extension of this model yields $\alpha = 5.4$ [77].

This Fano lineshape, although relying on a simple Lorentzian shape of the DOS, has been established as a sort of go-to model function to fit to a measured Kondo spectrum, since it usually describes an asymmetric spectrum fairly well [78, 79].
However, Frota was able to show that the exact shape of a Kondo resonance

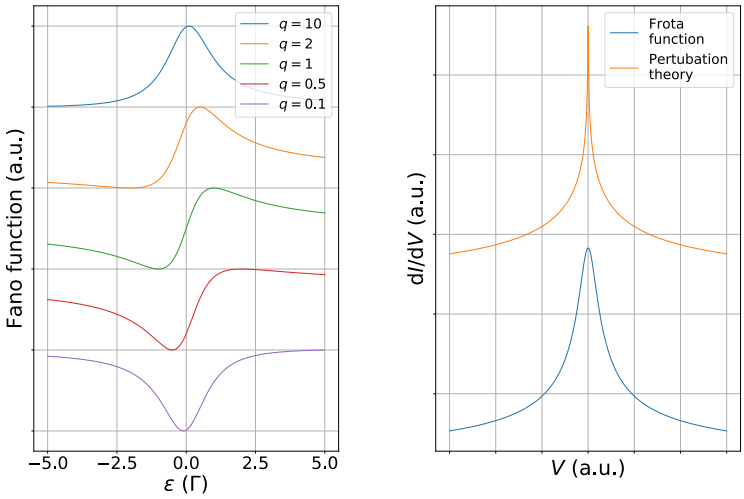

(a) Fano lineshape **(b)** Different model functions

Figure 2.7: Model functions for the shape of a Kondo spectrum in STS. (a) The Fano lineshape is plotted for various Fano factors q. (b) The Frota function (strong-coupling) and the result from third order perturbation theory (weak-coupling) are plotted. It should be pointed out, that these two spectra do not describe the same Kondo system, which hinders a direct comparison. They are plotted only to illustrate the logarithmic divergence in the latter case compared to the smooth peak in the former case.

in the DOS is not given by a mere Lorentzian, but by the after him named Frota function [75, 76]

$$\mathrm{DOS}(\epsilon) \propto \Re\left(\frac{\mathrm{i}\Gamma_\mathrm{K}}{\epsilon + \mathrm{i}\Gamma_\mathrm{K}}\right)^{1/2}. \tag{2.31}$$

This lineshape has also been used in some works to model a measured Kondo spectrum [80, 81]. Here, the Kondo temperature of the system is again given by the half width of the peak Γ_K at half maximum via

$$k_\mathrm{B} T_\mathrm{K} = \xi\ \Gamma_\mathrm{K}. \tag{2.32}$$

The prefactor, which in [76] is given as $\xi = 2\pi \cdot 0.103$, however, is still under debate.

Last, an extension to this Frota function exists analogue to the Fano model, where the interference of the two possible tunneling paths into the bulk states and a Fano-shaped resonance, are taken into account. The result is given by [82]

$$\frac{\mathrm{d}I}{\mathrm{d}V} \propto \Re\left(\mathrm{e}^{\mathrm{i}\phi_q}\frac{\mathrm{i}\Gamma_\mathrm{K}}{\epsilon+\mathrm{i}\Gamma_\mathrm{K}}\right)^{1/2}. \tag{2.33}$$

The phase ϕ_q is related to the Fano factor q by

$$q = \tan(\phi_q/2). \tag{2.34}$$

The case $\mathbf{T \gtrsim T_K}$

In this limit, the so-called *weak-coupling regime*, a perturbational approach analogue to one performed by Kondo is valid [68], which will result in a different shape of the Kondo resonance. Such an approach based on perturbation theory was performed by Applebaum [83, 84] and Anderson [85] in order to calculate the conductance near zero bias of planar tunnel junctions. A more general extension of this *Anderson-Applebaum* model was suggested by Ternes [86, 87]. There, tunneling spectra are calculated in third order perturbation theory in the exchange scattering parameter $\mathcal{J}$ (not the same as the exchange constant of equation 2.22) using second order Born approximation. In this extension also more complicated spin systems including magnetocrystalline anisotropy can be treated. Interestingly, in this model the Kondo resonance is a very sharp, logarithmically diverging function. Figure 2.7b shows the shape of the Kondo spectrum that results from this model for a spin 1/2 compared to a Frota function. It should be pointed out here, that these two spectra do not correspond to the same Kondo system, which hampers the direct comparison. Still this plot illustrates qualitatively well enough, how the the Frota function is a smooth peak in contrast to the arbitrarily sharp divergence that results from perturbation theory.

While the Kondo temperature was simply given by the width Γ of the resonance at half the peak height before in the Frota- and Fano model, it is less obvious here, since the peak width is very ill-defined for a diverging function. It should be pointed out, that in this perturbational model, the

Kondo temperature is no well defined quantity, but it is rather a temperature scale that indicates whether or not the perturbational approach is valid. The corresponding parameter in this model is the coupling strength $\mathcal{J}$ of the impurity spin to the conduction electrons of the host. The residual parameters used in the model are described elaborately in reference [86], and shall not be reiterated here.

Splitting the Kondo resonance by magnetic field

By applying a magnetic field, the Kondo resonance can be split [88, 89]. This can easily be understood with the following heuristic explanation. The Kondo model was considering the elastic spin-flip scattering between the spin up and spin down orientation of a localized spin 1/2. An applied magnetic field causes a Zeeman splitting, such that the spin-flip process becomes inelastic as is illustrated in figure 2.8. The splitting can be understood in this picture as the two steps one expects for an inelastic excitation (see chapter 2.1.4) that are superimposed with the original Kondo resonance [90].
Note, that in the weak-coupling regime of figure 2.8, technically any magnetic field splitting, no matter how small, should be observable, provided a sufficient experimental energy resolution is given. This can be attributed to the logarithmic divergence, which makes the peak arbitrarily sharp. Conversely, it could be shown, that in the strong coupling limit, a splitting can only be expected above a critical field [74, 91]

$$B_c \sim \frac{0.5 k_\mathrm{B} T_\mathrm{K}}{\mu_\mathrm{B}}. \tag{2.35}$$

In other words, the Zeeman energy must be at least of same order as the energy scale of the exchange scattering set by the Kondo temperature T_K, i.e. the width of the Kondo resonance.
Another interesting aspect of this is, that the two peaks of the split Kondo resonance are utterly spin-polarized [90]. This point will be picked up more elaborately in chapter 4.

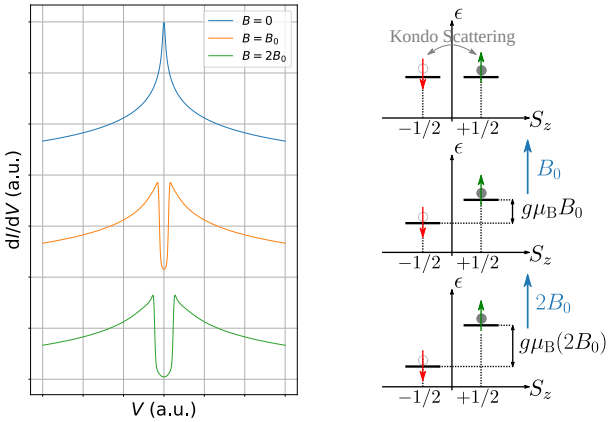

Figure 2.8: Splitting of the Kondo resonance. Some model spectra using the perturbational approach are plotted (left). A cartoon illustrates the origin of the Kondo splitting (right).

2.4 Quantum Mechanics of Single Magnetic Molecules

In this work so-called single-molecule magnets (SMM) and spin crossover (SCO) molecules were investigated. Special emphasis was placed on the question, whether the magnetic degrees of freedom of these molecules are suitable to serve as single magnetic bits. All investigated molecules are metal-organic complexes, that consist of a central, magnetic metal ion that is surrounded by organic ligands. The bonds between the ion and the ligand crucially affect the magnetic properties of the molecules. In this section this crystal field interaction and its consequences for the molecule's spin spectrum is discussed. In the next step, this will help to derive the criteria to get a molecule with a stable spin, when it is adsorbed on a metallic surface. There, the symmetry of the crystal field and the Kondo effect discussed in the previous section will play prominent roles. Finally, spin crossover molecules as a special case of functional magnetic molecules will be described.

2.4.1 Crystal Fields

Ions and atoms can posses a non-vanishing angular momentum. For free ions or atoms, the ground state is a multiplet of spin-orbit eigenstates $|J, L, S, m_J\rangle$ which can be determined by Hund's rules. In this case all the (2J+1) states of this multiplet are degenerate and the magnetic moment is given by

$$(\mu_J)_J = - g_{JLS} \frac{\mu_B}{\hbar} \hat{\boldsymbol{J}} \tag{2.36}$$

with the the Landé factor $g_{JLS} = 1 + \frac{J(J+1)-L(L+1)+S(S+1)}{2J(J+1)}$ and the Bohr magneton $\mu_B = \frac{e\hbar}{2m_e}$ [46].
Atoms or ions in a solid or an metal-organic molecule, however, additionally experience the electric field caused by the surrounding atoms. Note, that due to spin-orbit coupling this crytal field not only couples to the orbital angular momentum, but also affects the spin. The new ground state is determined by the competition of the crystal field and spin-orbit interaction and in the general case is not the one predicted by Hund's rules. Therefore, some qualitatively different cases have to be distinguished [46, 62].

Lanthanides (4f)

In the case of rare earth elements the 4f electrons are the origin of the magnetic properties. Since rare earth elements exhibit a rather large proton number, spin-orbit coupling is relatively strong compared to the rather weak crystal field effects. Typically, the crystal field has only weak influence on 4f electrons since the 4f orbitals are rather localized near the nucleus, meaning that the radial part of the wave function is much less extended compared to the 5p or 6s orbitals [92]. Hence, for describing the spin spectrum of 4f electrons one usually starts with the spin-orbit eigenstates $|J, L, S, m_J\rangle$ of the ground state multiplet determined by Hund's rules. Then, the crystal field can be considered a weak perturbation that lifts the degeneracy of the (2J+1) states in the multiplet, which is usually called *zero field splitting (ZFS)*. According to first order degenerate perturbation theory, one finds the new energy levels and states by diagonalizing the crystal field operator inside of the (2J+1)-dimensional manifold that is spanned by the initial

spin-orbit eigenstates $|J, L, S, m_J\rangle$. The result will be superpositions of states of different m_J and therefore m_J is not necessarily a good quantum number anymore. Which states get mixed depends on the crystal field Hamiltonian and - as will be argued in the following sections - on the symmetry of the crystal field.

Transition Metals (3d)

In the case of transition metals of the third period the magnetic properties arise from the 3d electrons. Unlike in the case of 4f electrons the radial part of the wave function of a 3d electron is typically rather extended. For instance, 3d electrons are often delocalized in a metal or participate in the complex bond in a metal-organic molecule. The consequence is a rather strong interaction with the crystal field, that is typically much stronger than spin-orbit coupling. Thereupon, Hund's rules to determine the many-electron ground state do no longer apply and the situation gets somewhat more subtle.
If one starts from a one-electron picture [62] and neglects SOC for the moment - it shall be treated as a perturbation in the end - the crystal field couples to the orbital angular momenta of the electrons only, while the spins remain good quantum numbers. Consequently, the degeneracy of the $|l, m_l\rangle$ single-electron states gets lifted, as these states mix up upon diagonalizing the crystal field Hamiltonian within the manifold spanned by the $|l, m_l\rangle$. The arising linear combinations correspond to the irreducible representations of the point symmetry group of the crystal. Often these crystal field eigenfunctions $|\varphi_{\mathrm{CF}}\rangle$ are real linear combinations of the $|l, m_l\rangle$. A prominent example is cubic symmetry that includes the cases of tetrahedral and octahedral environment, which will be discussed later. Since the angular momentum operator $\hat{\boldsymbol{l}} = -\mathrm{i}\hbar\, \boldsymbol{r} \times \boldsymbol{\nabla}$ is utterly imaginary in spatial representation, the resulting expectation values $\langle \varphi_{\mathrm{CF}} | \hat{\boldsymbol{l}} | \varphi_{\mathrm{CF}} \rangle$ should also be imaginary. However, since $\hat{\boldsymbol{l}}$ is hermitian, and therefore its expectation values must be real, this is only possible if all expectation values $\langle \varphi_{\mathrm{CF}} | \hat{\boldsymbol{l}} | \varphi_{\mathrm{CF}} \rangle$ vanish. The orbital angular momentum is said to be *quenched* and this phenomenon is usually referred to as *orbital quenching*. In this case the magnetic properties of the ion will only be determined by the total

electron spin $\hat{S}$.
It should be noted, though, that real 3d systems may not always be as simple. Spin-orbit coupling may mix the crystal field eigenstates $|\varphi_{\mathrm{CF}}\rangle$, such that orbital angular momentum may only be partially (or not be) quenched in the end. Moreover, electron-electron interactions have been totally neglected so far in this simplified one-electron picture. This will be discussed in section 2.4.4 for the example of cubic symmetry in spin crossover molecules.

Kramers degeneracy

One important aspect of crystal field theory is time reversal symmetry. Since the crystal field is merely an electric field, it cannot be affected by time inversion. Accordingly, the crystal field Hamiltonian $\hat{\mathcal{H}}_{\mathrm{CF}}$ must commute with the time inversion operator $\hat{\mathcal{T}}$:

$$\left[\hat{\mathcal{H}}_{\mathrm{CF}}, \hat{\mathcal{T}}\right] = 0. \tag{2.37}$$

As a result, the time inversion of an eigentstate $|\psi\rangle$ of $\hat{\mathcal{H}}_{\mathrm{CF}}$ with energy ϵ will also be an eigenstate of $\hat{\mathcal{H}}_{\mathrm{CF}}$ with the same energy:

$$\hat{\mathcal{H}}_{\mathrm{CF}}\left(\hat{\mathcal{T}}|\psi\rangle\right) = \hat{\mathcal{T}}\hat{\mathcal{H}}_{\mathrm{CF}}|\psi\rangle = \epsilon\left(\hat{\mathcal{T}}|\psi\rangle\right). \tag{2.38}$$

This result is part of the more general *Kramers theorem* [93]. Given time reversal symmetry, it states that in a system with an odd number of electrons all eigenstates of $\hat{\mathcal{H}}$ are at least twofold degenerate. In contrast, what happens in systems with an even number of electrons is that singlet states occur, which are their own time inversion. All other states will still be at least twofold degenerate according to equation 2.38.

2.4.2 Single-Molecule Magnets and Zero Field Splitting

As described above, free atoms exhibit a degenerate ground state multiplet of $(2J+1)$ spin-orbit eigenstates. One could naively imagine to store information in the m_J quantum number, simply by initializing the atom in the

desired state $|J, L, S, m_J\rangle$. Since this state is - as every state of the ground state multiplet - an eigenstate of the ions Hamiltonian $\hat{\mathcal{H}}_{\text{free}}$, the time evolution is just a phase factor and the system will remain in the initialized state forever. However, for practical applications the atoms cannot be free, but it is crucial to contact them electronically for manipulation and readout. For example this is readily achieved by depositing the atoms or molecules containing a magnetic ion on a metallic substrate to investigate or manipulate them using an STM. As a result, the ion's full Hamiltonian will additionally feature the perturbations caused by the interaction with its environment, i.e the metallic substrate and or the ligands. Hence, the degeneracy of the multiplet may get lifted as described above and transitions between the different spin states may occur due to thermal fluctuations and electron scattering processes.
The idea of SMMs is now to use organic ligands - not only to screen the ion from interactions with the metallic substrate - but mainly to control the ion's environment in such a way, that the crystal field eigenstates feature a certain desired spin spectrum. For a classical bit this would merely be a doublet of two states that are separated by an energy barrier. The easiest example to illustrate this idea is an angular momentum J with uniaxial anisotropy. The crystal field Hamiltonian in this case reads

$$\hat{\mathcal{H}}_{\text{CF}} = D\hat{J}_z^2. \tag{2.39}$$

Figure 2.9 shows the corresponding spectrum for the spin $J = 3/2$. The degeneracy of the four initial states is lifted and the spectrum contains of two so-called *Kramers doublets*. This splitting, that occurs even in the absence of an external magnetic field, is the aforementioned ZFS and is the base of SMMs. In the case of $D < 0$ ($D > 0$), the state with larger (smaller) J_z is favored. The spin is said to exhibit out-of-plane (in-plane) anisotropy. The first case ($D < 0$) is well-suited for a bit, since the two orientations with $m_J = \pm 3/2$ are separated by an energy barrier. Therefore, one expects no transitions between the two states of the ground state doublet for temperatures $k_{\text{B}}T \ll 2D$. Moreover, elastic spin-flip scattering - that means without energy transfer - like in a Kondo system is not possible, since every scattering process can only transfer $1\hbar$ of angular momentum. To overcome the barrier by tunneling through it, a third order process was necessary, which is very unlikely. Therefore, one expects this case to represent a stable

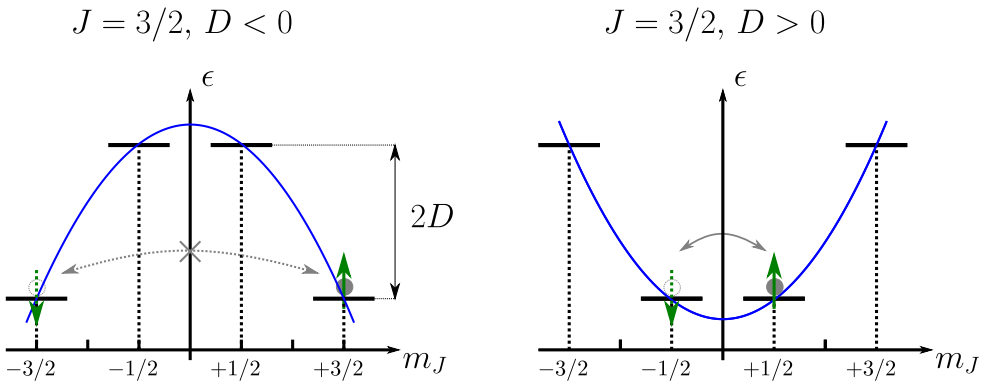

Figure 2.9: Energy diagram for a spin J = 3/2 with uniaxial anisotropy. (Left) For out of plane anisotropy the spin cannot be reversed by elastic scattering. Therefore, the states with $m_J = \pm 3/2$ are stable. (Right) In the case of in plane anisotropy this is possible, such that this represents a Kondo system.

bit. In the latter case ($D > 0$), however, there is no barrier and a single (elastic) scattering event can already flip the spin. Thus, one would expect this to be a Kondo system, where the magnetic moment is screened by the conduction electrons of the metal substrate. In STS one would expect to see an inelastic excitation at the energy $2D$ for both cases and a Kondo resonance at zero bias only for the latter case.

In reality, however, it is not easy to get a system with uniaxial anisotropy, but ions on surfaces or in molecules rather do only exhibit discrete rotational symmetry in the x-y-plane. The result will be, that m_J will not be a good quantum number anymore and the crystal field eigenstates will be superpositions of the $\hat{J}_z$ eigenstates. This can easily be illustrated by following a simple heuristic approach for the crystal field Hamiltonian analogue to reference [94] as a quadratic form:

$$\hat{\mathcal{H}}_{\mathrm{CF}} = \hat{\boldsymbol{J}} \cdot \underline{\underline{\boldsymbol{D}}} \cdot \hat{\boldsymbol{J}}. \tag{2.40}$$

Note, that due to time inversion symmetry, the Hamiltonian must not include odd powers of $\hat{\boldsymbol{J}}$. Since $\underline{\underline{\boldsymbol{D}}}$ is hermitian we can choose the coordinate system such that

$$\hat{\mathcal{H}}_{\mathrm{CF}} = D_{xx}\hat{J}_x^2 + D_{yy}\hat{J}_y^2 + D_{zz}\hat{J}_z^2 \tag{2.41}$$

$$= D\hat{J}_z^2 + E(\hat{J}_x^2 - \hat{J}_y^2) + \text{const}, \tag{2.42}$$

with the coefficients being

$$D = D_{zz} - 1/2(D_{xx} + D_{yy}), \quad E = 1/2(D_{xx} - D_{yy}). \tag{2.43}$$

The constant in equation 2.41 can be omitted such that we get

$$\hat{\mathcal{H}}_{\mathrm{CF}} = D\hat{J}_z^2 + E/2(\hat{J}_+^2 + \hat{J}_-^2) \tag{2.44}$$

with the ladder operators

$$\hat{J}_\pm = \hat{J}_x \pm \mathrm{i}\hat{J}_y. \tag{2.45}$$

In the case of uniaxial anisotropy, i.e. $D_{xx} = D_{yy}$, the second term vanishes and one gets back the Hamiltonian of equation 2.39.
With this, the former spin $J = 3/2$ system with $D < 0$ shall be revisited in the case of lower symmetry, for instance twofold rotational symmetry in the x-y-plane. In this case the Hamiltonian will mix two states with $\Delta m_J = 2$, such that there will be two sets of eigenstates. The result is sketched in figure 2.10. The crucial point now is, that because of this mixing the matrix element $\langle\alpha|\hat{\boldsymbol{J}}\cdot\hat{\boldsymbol{\sigma}}|\delta\rangle$ is non-zero. Consequently, a single elastic spin-flip scattering event can already cause transitions between the two states $|\alpha\rangle$ and $|\delta\rangle$ of the lowest doublet. The spin is said to tunnel through the barrier and this effect is usually referred to as *quantum tunneling of magnetization* (QTM). Consequently, this case again represents a Kondo system.
Yet another example would be the case of fourfold symmetry ($D_{xx} = D_{yy}$). From equation 2.43 follows directly that $E = 0$ - and analogue to the case of uniaxial anisotropy - that the spin $J = 3/2$ will be stable again. These easy examples illustrate that a spin's stability, in general, crucially depends on the crystal field symmetry [95]. This issue will be tackled in the next section 2.4.3.

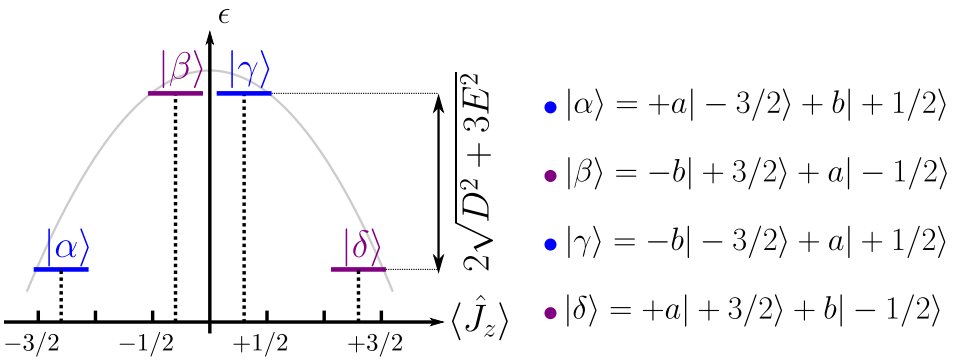

Figure 2.10: Energy spectrum for a spin J = 3/2 with twofold rotational symmetry. In this case first order transitions from one subset to the other are possible via Kondo scattering.

2.4.3 Stevens Operators

The previous section illustrated, that the crystal field symmetry is crucial for the spin Hamiltonian and therefore for a spin's stability. A very convenient method to exploit the point symmetry of the crystal field is using Stevens operators [62, 93, 94, 96]. The underlying idea is to treat the crystal field of the spin's environment as an assembly of point charges and expand the resulting crystal field potential in terms of spherical harmonics:

$$V(r,\theta,\phi) = \sum_{k=0}^{\infty} \sum_{q=-k}^{k} \tilde{B}_k^q \, r^k \, Y_k^q(\theta,\phi). \tag{2.46}$$

Given the symmetry group of the environment, only certain expansion coefficients $\tilde{B}_k^q$ can be non-zero. In the next step the Stevens operator equivalents $\hat{O}_k^q$, that are combinations of $\hat{\boldsymbol{J}}^2$, $\hat{J}_+$, $\hat{J}_-$ and $\hat{J}_z$, are introduced. These operators are equivalent in the sense, that they yield the same matrix elements as their corresponding combination of spherical harmonics. In this respect the Wigner-Eckart theorem was used. With this the Hamiltonian can be written as

$$\hat{\mathcal{H}}_{\mathrm{CF}} = \sum_{k} \sum_{q=0}^{k} B_k^q \hat{O}_k^q. \tag{2.47}$$

Therein, an operator $\hat{O}_k^q$ involves only terms with the components $\hat{J}_i$ to the power k, while the ladder operators $\hat{J}_+$ and $\hat{J}_-$ occur precisely to the power

of q. Consequently, the sum only includes even numbers k due to time reversal symmetry. Moreover, all terms with $k > 2J$ or $k > 2l$ vanish, where $l = 2$ or $l = 3$ for 3d- or 4f electrons, respectively. A list of these operators can be found for instance in [62, 93].
The convenience of this formalism is that all the non-zero coefficients B_k^q are directly given by the symmetry group of the molecule. For instance, in the case of n-fold rotational symmetry only the coefficients with $q = z \cdot n$ (with $z \in \mathbb{N}_0$) are non-zero. As a result, the crystal field eigenstates will be superpositions of states with $\Delta m_J = z \cdot n$ (with $z \in \mathbb{N}_0$).
Applying these rules for instance to the spin $J = 3/2$ in twofold symmetry from the previous section, one gets

$$\hat{\mathcal{H}}_{\mathrm{CF}} = B_2^0 \hat{O}_2^0 + B_2^2 \hat{O}_2^2 = B_2^0 \ \left(3\hat{J}_z^2 - J(J+1)\right) + B_2^2 \ 1/2 \left(\hat{J}_+^2 + \hat{J}_-^2\right), \qquad (2.48)$$

which is equivalent to the heuristic approach of equation 2.44.

2.4.4 Spin Crossover Molecules

Spin crossover complexes are a special kind of magnetic molecules where transitions between a non-magnetic state and a paramagnetic state occur [26, 97, 98]. These transitions, which are usually referred to as *spin crossover* (SCO), are driven thermally. However, a SCO can also be triggered by various external perturbations, such as light or x-ray irradiation [99, 100, 101], pressure [102] or electrical currents [103], making these molecules interesting candidates for multifunctional spintronic devices. In the following, the underlying physics of these type of molecules and the SCO transitions shall be discussed briefly.

The prototypical SCO molecule consists of a central transition metal ion with the electronic configuration $[\mathrm{Ar}]3d^6$ (e.g. Fe^{2+} or Co^{3+}) surrounded by organic ligands with 6-fold octahedral coordination, as illustrated in figure 2.11. Following the procedure described in section 2.4.1, the degeneracy of the 3d orbitals is lifted and one ends up with two sets of states. These so-called t_{2g} and e_g states correspond to irreducible representations of the

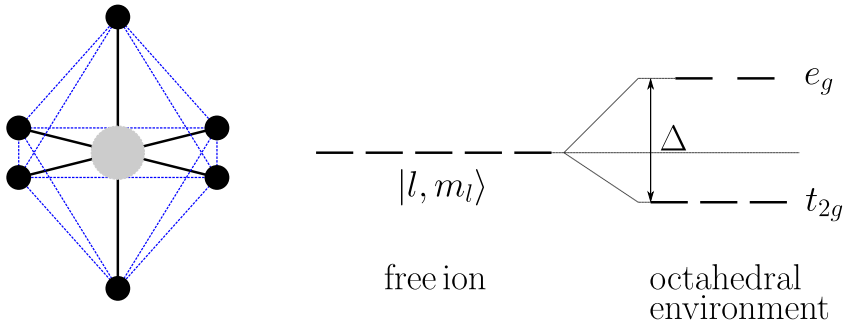

Figure 2.11: Octahedral geometry and crystal field splitting. In the octahedral environment, the 3d orbitals split in two sets of t_{2g} and e_g orbitals.

octahedral symmetry group. Their spatial representations are depicted in figure 2.12. Indeed, these wave functions are real functions such that the orbital angular momenta of the 3d electrons are quenched:

$$\langle \{e_g\} | \hat{\boldsymbol{l}} | \{e_g\} \rangle = \langle \{t_{2g}\} | \hat{\boldsymbol{l}} | \{t_{2g}\} \rangle = 0. \tag{2.49}$$

In figure 2.12 it strikes right away that the e_g orbitals are oriented along the coordinate axes, i.e. in the direction of the coordinating atoms sitting on the corners of the octahedron, while the t_{2g} orbitals avoid these directions. Accordingly, an e_g electron will experience a stronger electrostatic repulsion due to the ligand atom than a t_{2g} electron. Hence, the latter orbital is expected to be energetically favorable in this picture.
In the next step these orbitals have to be occupied by the six 3d-electrons. Depending on the competition between the splitting Δ on the one hand and the pairing energy of two electrons occupying the same orbital on the other hand, two cases can occur. This issue is illustrated in figure 2.13. Firstly, if the splitting Δ is large, it will be energetically favorable for the electrons to simply pay the pairing energy in oder to occupy the lower lying t_{2g} orbitals. The result is a non-magnetic ground state with $S = 0$. Conversely, if Δ is relatively small, it will be favorable for the electrons to simply follow Hund's first rule to minimize electron-electron repulsion by maximizing the total spin. Thus, the total spin will yield $S = 2$. The first case is usually

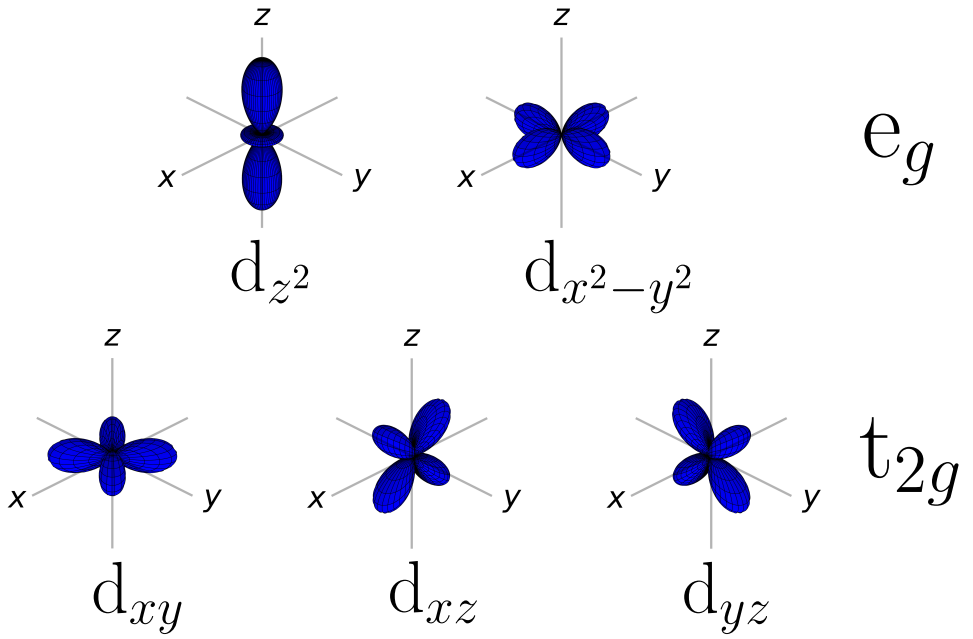

Figure 2.12: Spatial representation of the e_g and t_{2g} orbitals. The distance to the origin gives the absolute values of the wave function for every orientation (θ, ϕ).

referred to as *low spin* (LS) or *strong field* case, while the latter is called *high spin* (HS) or *weak field* case.

A more advanced approach, than simply treating the metal ion's environment as an assembly of point charges, is *ligand field theory*. Here, the orbtial structures of the ligands and their overlap with the 3d, 4s and 4p orbitals of the transition metal ion is taken into account [104]. The result is a set of molecular orbitals (MO). Those MOs with a bonding character will be fully occupied and are therefore rather not interesting for the magnetic properties of the molecule. Overlooking these bonding orbitals, one ends up in a situation that is qualitatively equivalent to the previous result, where six residual electrons have to be distributed to three non-bonding t_{2g} and the two lowest lying anti-bonding e_g^* orbitals. Thus, the result is qualitatively the same, that was obtained by the more simplified picture of crystal field theory. Still, one expects a weaker metal-ligand bond and

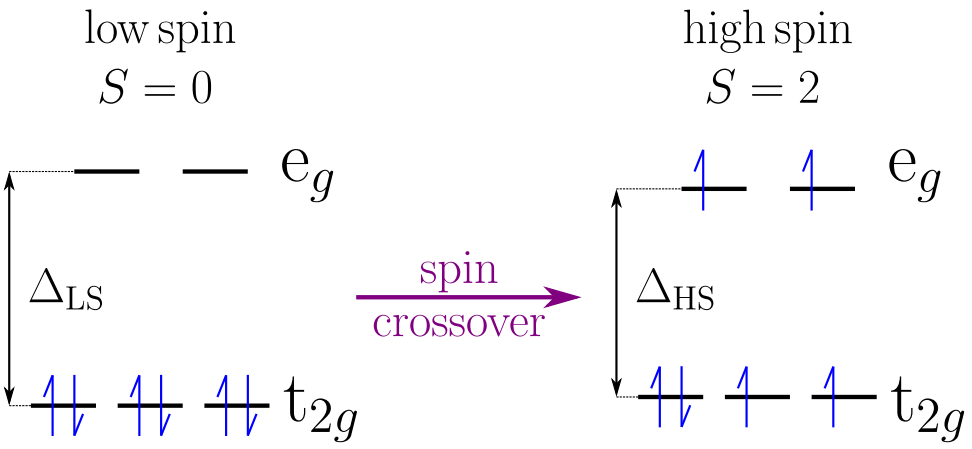

Figure 2.13: Electron configuration for high spin and low spin state of a spin crossover molecule.

therefore a slightly larger metal-ligand distance for the HS case, because of the anti-bonding character of the e_g orbitals.

For a SCO molecule both, LS and HS case, exist and transitions between the two states occur. For this to happen, it is crucial that HS and LS state have very similar energies, with the LS state having a slightly lower energy at 0 K. Then, the thermal SCO must occur due to simple thermodynamic reasons: Considering that the Helmholtz free energy $F = U - TS$ must be minimal in equilibrium, at low temperatures the ground state, i.e. the non-magnetic LS state, is favored. With increasing temperature, however, eventually the state with the higher entropy will be favored. This is the paramagnetic HS state mainly because of two reasons. First of all because of its additional spin degree of freedom. Secondly, the density of states for vibrational excitations is higher for the high spin state, which is a result of the slightly longer and weaker metal-ligand bond [26].

The possibility to trigger the SCO by applying pressure also follows from the difference in the metal-ligand bond between LS and HS state. At high pressures the state with the shorter bond and hence the smaller volume

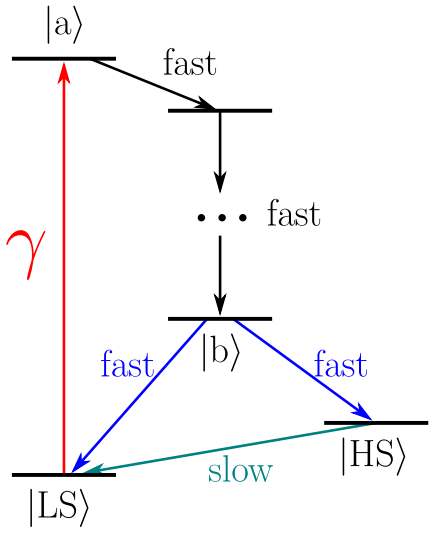

Figure 2.14: Scheme of the mechanism underlying the LIESST effect

should be preferred. Accordingly, upon increasing the ambient pressure, eventually a $HS \rightarrow LS$ transition should occur.

In contrast, the light induced SCO is not a thermodynamic transition, but relies on the metastability of the HS state. The underlying process is called *light induced excited spin state trapping* (LIESST) and is depicted in figure 2.14 in a very simplified manner. By absorption of a photon, the molecule can be excited from the initial LS state to a higher energy state $|a\rangle$. The relaxation - usually consisting of many steps - eventually ends up with the molecule in a state $|b\rangle$, that can decay either to the LS or the HS state. Since the decay back to the LS state is fast and the direct transition from HS to LS state is suppressed and therefore slow, one will eventually end up in the HS state. The x-ray induced SCO works analogously and is called *soft x-ray induced excited spin state trapping* (SOXIESST).

2.5 X-ray Absorption Spectroscopy and Magnetic Dichroism

X-ray absorption spectroscopy (XAS) refers to the measurement of the absorption coefficient of a sample as function of photon energy. As the latter is gradually increased while acquiring a spectrum, a sudden increase in the absorption occurs every time the photon energy is high enough to excite a core electron above the Fermi level into the conduction band [105, 106]. These jumps are usually referred to as absorption edges. As the respective edge energies depend on the binding energies of the core electrons, this technique is highly element-specific. Using x-ray sources with high brilliance like modern synchrotron facilities, sensitivities way beyond one monolayer of atomic or molecular coverage are readily achieved, which makes XAS a very convenient and powerful tool in surface science and in particular in order to investigate SMMs on metal surfaces.

Generally, for samples containing 3d transition metals the L_3 and L_2 absorption edges are particularly interesting. As illustrated in figure 2.15a, those two edges correspond to the transitions from $2p_{3/2}$ and from $2p_{1/2}$ to the empty 3d states, respectively. In this respect, one simple application, which is very relevant for this work, is the distinction of the spin state of spin crossover molecules [101], where the d-orbitals of the central divalent iron ion are split as elaborated in section 2.4.4: In the HS case excitations to both, the lower t_{2g} levels and e_g levels are possible, while in the LS state only transitions to the higher e_g levels are possible. The absorption edges measured for HS and LS molecules will therefore differ in shape and position. This specific example is also shown later in chapter 6.3 for Fe-Pyrz molecules.

In an extension of XAS, circularly polarized photons are used, which additionally enables to probe the sample's magnetic properties. For this purpose, the magnetic dichroism, i.e. the difference in absorption for left- and right-handed circularly polarized photons is measured. In such an experiment, the sample magnetization is oriented along the x-ray propagation vector $\boldsymbol{k}$. This experimental technique is called x-ray magnetic circular dichroism

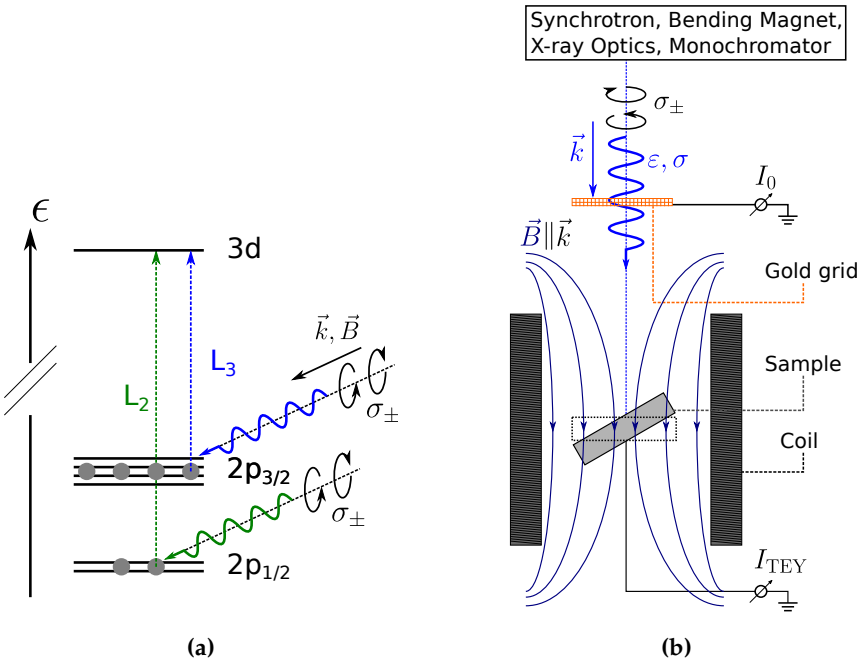

Figure 2.15: Schematics and experimental setup of an XAS or XMCD measurement. (a) The electronic transitions referring to L_2 and L_3 absorption edges are shown. (b) A typical experimental setup for XAS or XMCD measurements is shown.

(XMCD) spectroscopy and allows the element specific analysis of spin and orbital contributions to the magnetic properties of a sample [105, 107, 108, 109]. The origin of this difference in absorption for right- (σ_+) and left-handed (σ_-) polarization in magnetic materials can easily be understood for the XMCD of the L_3 and L_2 edges of 3d transition metals in a simple one-electron picture, where the absorption process is divided into two steps [107, 109].

In the first step, the photons with polarization $\sigma_\pm$ transfer $\pm 1\hbar$ of angular momentum to the 2p electrons. Such an absorption process corresponds to a transition with $\Delta m_l = \pm 1$. Because of spin-orbit interaction, though, the photon's angular momentum is partially transferred to the electron spin. To be specific, both, $|2p_{1/2}\rangle$ and $|2p_{3/2}\rangle$ states, are spin-orbit eigenstates, such that the spin orientation is coupled to that of the orbital angular momentum. As a consequence, a dipole transition with a given Δm_l favors one spin orientation over the other, such that the excited electrons are spin-polarized. In

the second step, the 3d band acts as a spin analyzer, since for a ferromagnet the density of states at the Fermi level is different for spin up and spin down electrons. Hence, according to Fermi's golden rule, different transition rates are expected for $\Delta m_l = +1$ and $\Delta m_l = -1$ transitions. Altogether, this results in different absorption coefficients for the two opposite polarizations. Naturally, reversing the sample magnetization has the same effect as using the opposite polarization.
With more elaborate theoretical considerations the so-called *sum rules* can be derived. These very simple rules describe quantitative relations between the total intensities of the XMCD of the L_2 and L_3 edges with the components of the spin and orbital magnetic moments along the sample magnetization, i.e. the beam direction [105, 107]. This even allows to probe the magnetic anisotropy by measuring the XMCD at various sample orientations with respect to the beam [110]. A more elaborate discussion of these sum rules, however, is beyond the scope of this work, since such an analysis was not performed. The XMCD measurements in chapter 6.3 could merely be interpreted in a qualitative way.

A typical experimental setup of such an x-ray absorption measurement is schematically depicted in figure 2.15b. A synchrotron is used as x-ray source. The synchrotron radiation is produced either by a bending magnet or as it is common in more modern synchrotrons by an undulator [106, 109]. In the former case, the polarization needs to be determined by the opening position of the beam line's aperture: While the synchrotron radiation is linear polarized in the plane of the storage ring, it is partly circularly polarized above or below this plane [106, 109]. After passing some x-ray optics, the beam hits the monochromator, which is usually a grating, i.e. a textured surface, where the beam is diffracted. By correctly setting the diffraction angle, the energy of that part of the beam, that is used to probe the sample, can be determined.
Before the beam hits the sample, it has to pass a gold grid first, where the initial intensity I_0 is measured as a photocurrent. This signal is used to normalize the absorption signal in order to eliminate irradiation fluctuations. The sample is located inside a coil, which is able to magnetize it along the beam direction, such that $\boldsymbol{B} \| \boldsymbol{k}$ inside the coil. For measuring the sample absorption, the most straightforward way is to measure either

the sample current or the sample fluorescence, which is referred to as *total electron yield* (TEY) and *fluorescence yield* (FY), respectively. The underlying principle is simple: The absorption of an x-ray photon results in an empty core state. The relaxation of an electron to this core level will either emit fluorescence light, or Auger electrons [111]. The fluorescence signal can directly be measured by an additional detector. Auger electrons are usually high in energy (several hundert eV), such that their inelastic mean free path is rarther short (of the order of nm) [112]. Accordingly, one Auger electron will excite a whole bunch of secondary electrons, that is able to leave the sample. As a result, a photocurrent that is proportional to the x-ray absorption can be measured in TEY.
In the end, the surface sensitivity of XAS depends on the detection method [106, 113, 114]: Typically the penetration depth of soft x-rays is of the order of some 100 nm. The highest surface sensitivity (roughly 1 nm) is achieved by detecting Auger electrons only, which would require an additional detector with energy analyzer. Thus, it is more convenient to measure the total number of photoelectrons, i.e. the TEY, which results in probe depths of roughly 10 nm. Conversely, a FY measurement is more bulk sensitive with probe depths of the order of 100 nm. In this work, all measurements were performed in the TEY mode.

2.6 Magneto-Optic Kerr Effect

The magneto-optic Kerr effect (MOKE) refers to the phenomenon, that the plane of polarization of light is rotated upon reflection from a ferromagnetic surface [115]. This effect is closely related to the Faraday effect, which describes the change of polarization upon transmission. Both effects rely on a different dielectric response of a ferromagnet on the right- and left-handed circularly polarized components of light. The microscopic cause of this lies in the spin-orbit coupling: Illustratively, right- and left-handed circularly polarized light excite opposite electron movements. Due to spin-orbit interaction, these orbital movements are coupled directly to an electron's spin orientation. Since opposing spin orientations are not energetically equivalent in a ferromagnet, a different dielectric response results for the two

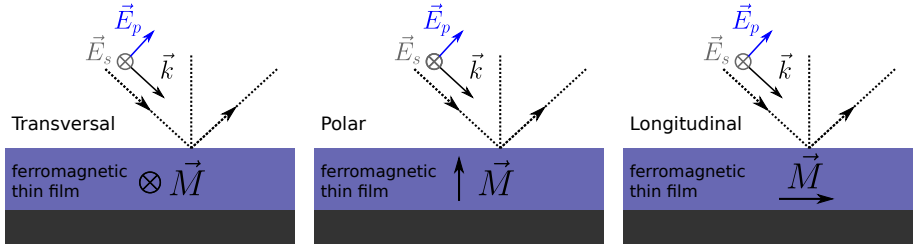

Figure 2.16: Different MOKE geometries. The different MOKE geometries are characterized by the orientation of the sample magnetization. Moreover, the direction of the electric field vector for p- and s-polarization is shown.

circular polarizations [46, 116, 117]. The Kerr effect is usually quantified by the *Kerr angle* Θ_K. Since also the absorption is different for the two circular polarizations, in general, the Kerr angle is complex, such that

$$\Theta_K = \Theta'_K + i\Theta''_K, \tag{2.50}$$

where Θ'_K is the *Kerr rotation* and Θ''_K is referred to as the *Kerr ellipticity*. Both quantities depend linearly on the sample magnetization [117].

Both, Kerr and Faraday effect can be described phenomenologically for an isotropic material by a dielectric tensor of the form

$$\underline{\underline{\epsilon}} = \epsilon \begin{pmatrix} 1 & iQ_z & -iQ_y \\ -iQ_z & 1 & iQ_x \\ iQ_y & -iQ_x & 1 \end{pmatrix}, \tag{2.51}$$

where the vector $\boldsymbol{Q}$ points along the sample magnetization and is usually referred to as *Voigt-Vector* [46]. For MOKE, three different experimental geometries exist, namely polar, longitudinal and transversal MOKE. For the different geometries, which are illustrated in figure 2.16, different components of $\boldsymbol{Q}$ are probed.

The most straightforward way to perform MOKE measurements in order to characterize a magnetic sample would be to simply measure the Kerr rotation. Such a setup is schematically shown in figure 2.17. A laser together with a polarizer provides linear polarized light, which is reflected from the magnetic sample. The reflected light is detected by a photodetector after it

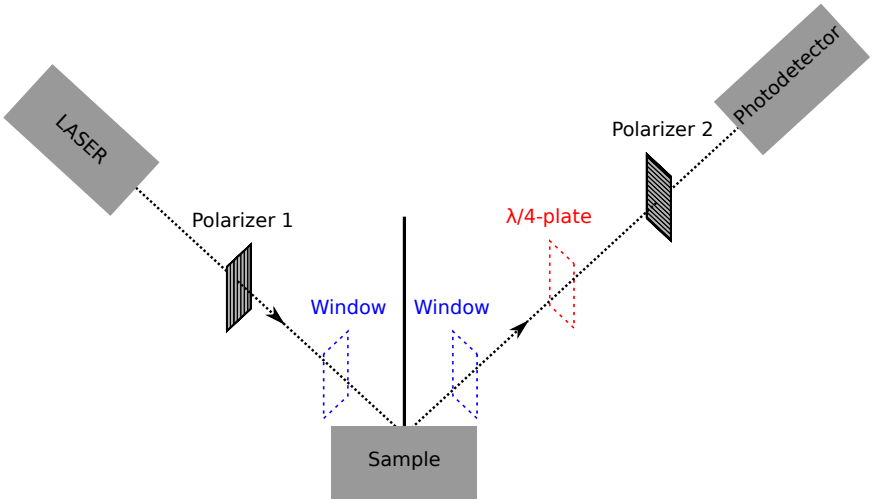

Figure 2.17: A prototypical MOKE setup. For MOKE measurements on an in-situ sample, an additional quarter-wave plate is used to compensate for the effects of the windows of the UHV chamber.

passed a second polarizer, which is perpendicular with respect to the first one. Like this all the signal in the detector originates from the Kerr rotation. For instance, if the incident light was p-polarized, then the reflected beam would be partly s-polarized and the Kerr rotation was merely given by

$$\Theta_\mathrm{K} \approx \tan\left(\Theta_\mathrm{K}\right) = \frac{E_s}{E_p}. \tag{2.52}$$

Hence, the measured intensity depends quadratically on the Kerr angle. Because of this, it is convenient, to not set the second polarizer exactly perpendicular with respect to the first one, but to offset its rotation by a small angle δ [116, 117]. Then, the measured intesity will be given by

$$I = |E_p \sin\delta + E_s \cos\delta|^2 \approx I_0 \left(1 + \frac{2\Theta'_\mathrm{K}}{\delta}\right), \quad \text{with } I_0 = |E_p|^2\delta^2. \tag{2.53}$$

Like this, small changes in the Kerr rotation, that occur for instance while ramping an external magnetic field in order to acquire a hysteresis loop, are easily detectable.

Another difficulty arises for MOKE measurements on samples in UHV.

There, the laser beam needs to pass two windows in and out of the UHV chamber, as indicated in figure 2.17. Oftentimes, these windows are birefringent, which would contribute to the MOKE intensity. It is therefore convenient to include a quarter-wave plate such that the window effects are canceled [116, 117]. The MOKE setup used in this work, too, works according to this principle. The initialization of the MOKE setup before the experiment hence included setting both, the quarter-wave plate and the second polarizer such that the measured intensity was minimum, and afterwards adding a small offset to the polarizer orientation.
Because of the insertion of the quarter-wave plate, though, in this configuration the Kerr ellipticity is measured rarther than the Kerr rotation. This can easily be seen in the above mentioned example of an incident p-polarized beam [116, 117]. The wave plate adds a phase shift of 90° between the p- and the s-polarization. Using equation 2.52 yields, that this is equivalent to $\Theta_K \rightarrow e^{i\pi/2}\Theta_K$, i.e. the Kerr rotation and the Kerr ellipticity swap roles.

3 Experimental Setups and Methods

This chapter gives an overview of the experimental setups and methods used. This includes the sample preparation methods and the measurement facilities. A total of three different setups including low-temperature STMs were used. These setups, that operate in ultra high vacuum (UHV) at base temperatures of 4.2 K, 700 mK and 25 mK, respectively, will be referred to as *4K STM*, *Joule-Thomson STM* (JT) and *dilution STM*. All of these cryostats including the scanning tunneling microscopes are homebuilt and were designed and assembled in the group of Prof. Wulf Wulfhekel [118, 119, 120]. In this chapter, first the common arrangements of the UHV chambers of those three setups will be discussed, following a short description of the cryostats and microscope heads. This will also include a short discussion of the underlying principles of a ^{3}He/^{4}He dilution refrigerator. The following sections will then describe sample and STM tip preparation. Finally, the last section gives a short overview of the WERA beamline, where the XAS and XMCD measurements were performed. There, also the sample transfer from the 4K setup to the beamline using a vacuum suitcase will be discussed.

3.1 Ultra High Vacuum Setups

Both, the sample preparation and STM measurements were performed in ultra high vacuum (UHV) in order to prevent pollution of the samples by adsorbates from the gas phase. Thereby, typical base pressures are of the order of 10^{-10} mbar. The basic arrangement, which is very similar for the three used setups, is depicted schematically in figure 3.1. The basic setup consists of three individually pumped chambers - an *air lock*, a *preparation chamber* and an *STM chamber* including the cryostat, that are connected via gate valves. Using different kinds of manipulators, the sample plates can

be transferred between neighbouring chambers *in-situ*, i.e. without ever leaving UHV conditions.

The UHV is created by using turbo molecular pumps (TMP). The necessary pre-vacuum is generated by rotary vane pumps evacuating buffer volumes (barrel), which make up the back sides of the three TMPs. The pressure of each chamber can be monitored by ionization gauges. Since STM measurements are very susceptible to mechanical vibrations, all mechanical pumps must be shut down during the measurement process. In order to still maintain the vacuum conditions during the measurement, both STM and preparation chambers possess ion getter pumps. Additionally, in the preparation chambers there are titanium sublimation pumps, while the STM chambers contain adsorption pumps made from a commercially available getter material (*SAES* pump).

The majority of the sample preparation takes place in the preparation chambers. There, sputter guns are mounted to clean a sample, which during operation are differentially pumped via the air locks. To anneal a sample by electron bombardment, the manipulators contain tungsten filaments for thermionic emission. Moreover the chambers feature devices for *low energy electron diffraction* (LEED) and *Auger electron spectroscopy* (AES), a *quadrupole mass spectrometer* (QMS) for residual gas analysis and various metal evaporators for *molecular beam epitaxy* (MBE). A detailed description of the used devices and methods for the sample preparation will be given in section 3.3. Moreover, the preparation chamber of the 4K setup features a *magneto optic Kerr effect* (MOKE) setup, that works according to the principles discussed in chapter 2.6.
The airlocks are used to transfer samples and STM tips in and out of the vacuum and contain the molecular evaporator used for the molecule deposition. Finally, the STM measurements take place in the STM chambers. In order to isolate the measurements from mechanical vibrations, every setup is mounted on a platform, which is borne by a pneumatic vibration isolator support by the company *Newport*.

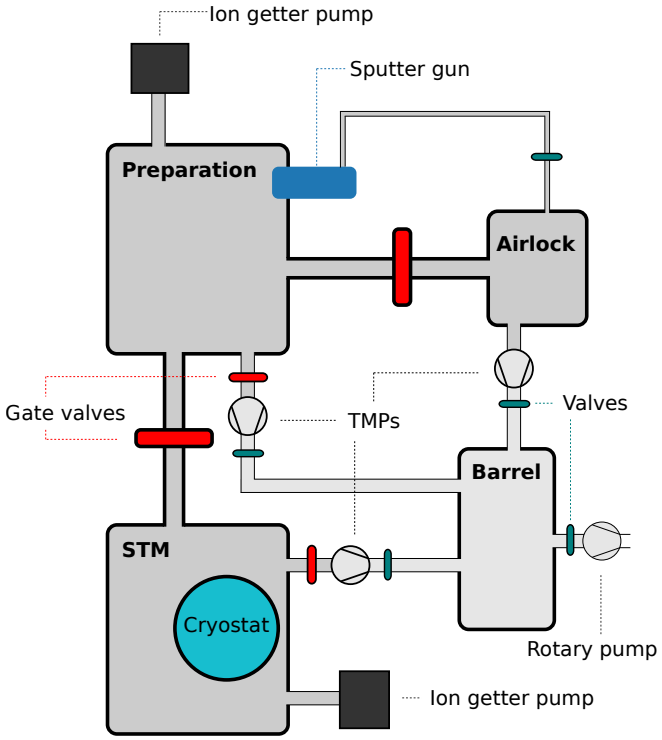

Figure 3.1: Basic arrangement of the UHV setups. This corresponds to the exact UHV setup of the JT setup. Small differences occur at the dilution and the 4K setup, where there are additional gate valves to separate the ion getter pumps from the STM and preparation chambers. Moreover, in the 4K setup the sputter gun is differentially pumped not by the air lock, but by an additional chamber that includes the molecular evaporator and is connected to the preparation chamber by another gate valve.

3.2 Cryostats and Scanning Tunneling Microscopes

Cryostats

All STM measurements of this work were performed at low temperatures. For most of the experiments this is necessary in order to have a sufficient energy resolution in spectroscopy as discussed in chapter 2.1. Additionally, thermal fluctuations will strongly influence the stability and coherence of a spin system. Furthermore, thermally activated diffusion of molecules on surfaces and even atoms of the STM tip is hampered at low temperatures, which yields much more stable measurement conditions. Last, due to the cryo pump effect, better experimental pressures are reached.
The three homebuilt cryostats of 4K, JT and dilution setup are wet cryostats, which means that cryogents such as liquid nitrogen (LN_2) and liquid Helium (LHe) are necessary. In figure 3.2a the JT cryostat structure is exemplified [118]. In case of the 4K and JT setup, the LHe tank is inside the tank for LN_2. Both tanks are thermally isolated from the external and each other by vacuum and contain a radiation shield from silver-coated copper, that are supposed to minimize the heat input by thermal radiation. Additionally, heat exchangers are located inside the LHe supply pipe at the shield positions, such that the shields are additionally cooled by the cold exhaust gas from the helium bath. In case of the 4K setup, the STM head is directly thermally coupled to the LHe bath, such that the experiment temperatures are close to the boiling point of helium at 4.2 K. The cryostat of the JT setup additionally contains a closed-cycle JT stage with ^{3}He as cooling refrigerant. When the circulation is activated, compressed and filtered ^{3}He gas is introduced to the cycle. The gas is then pre-cooled stepwise by countercurrent heat exchange with the cold gas from the backside of the JT stage and direct heat exchange with the LHe bath. Finally, the gas expands through a narrow capillary into the JT pot. Thereby the ^{3}He cools down due to the Joule-Thomson effect. The STM head is thermally coupled to this JT pot by gold wires, such that experiment temperatures below 700 mK can be achieved [118, 119].

The structure of the dilution setup is more subtle and elaborated in reference [120]. There the LHe tank is located below the LN_2 tank but inside

the nitrogen shields for space reasons. Inside the LHe tank is a commercial ^{3}He/^{4}He dilution fridge insert by *BlueFors Cryogenics*. With this, temperatures as low as 25 mK can be reached at the STM head. The underlying principles of a ^{3}He/^{4}He dilution refrigerator will be discussed later in this section.

Scanning Tunneling Microscopes

The STM heads are hanging freely from the cryostats by three springs made from beryllium-copper or phosphor-bronce. This is supposed to mechanically decouple the STMs from the external in order to minimize vibrations. In order to transfer samples and tips, every STM can be parked, that means fixed in a high, accessible position using a lever mechanism. In the unparked state during measurements, every STM head hangs in a lower position inside a superconductive coil from niobium-titanium, which can provide magnetic fields in z-direction, i.e. perpendicular with respect to the sample surface. The maximum possible fields are 200 mT, 3 T and 7.5 T for 4K, JT and dilution setup, respectively. The current supplies of the coils are high temperature superconductors (HTS) from *REBCO* (Rare Earth elements with Barium Copper Oxide). At the JT setup, the maximum magnetic field is additionally constraint by the Joule heating caused at the ohmic contacts between HTS and coil. Thus, in this work the maximum magnetic field accomplished at this setup was 1.7 T. Figure 3.2b shows the basic structure of the STM heads again using the example of the JT STM: The sample holder plate is located inside a stage, which can be moved in x-direction using a piezo motor. The motor consists of stacks of shear piezos and works according to the slip-stick principle. The tip holder is located on a piezo tube scanner [28], which is mounted on a copper prism. The prism again is supported by piezo stacks that allow a coarse motion in z-direction, which is used to approach the tip to the sample into the tunneling regime. Most of the constituent parts are made from copper or beryllium-copper in order to provide high thermal conductivity, which enables fast thermalization of STM and sample. In the parked state, the sample stage is directly accessible through doors in the radiation shields in all setups. This enables simple in-situ sample and tip transfers. The tip transfer procedure is described

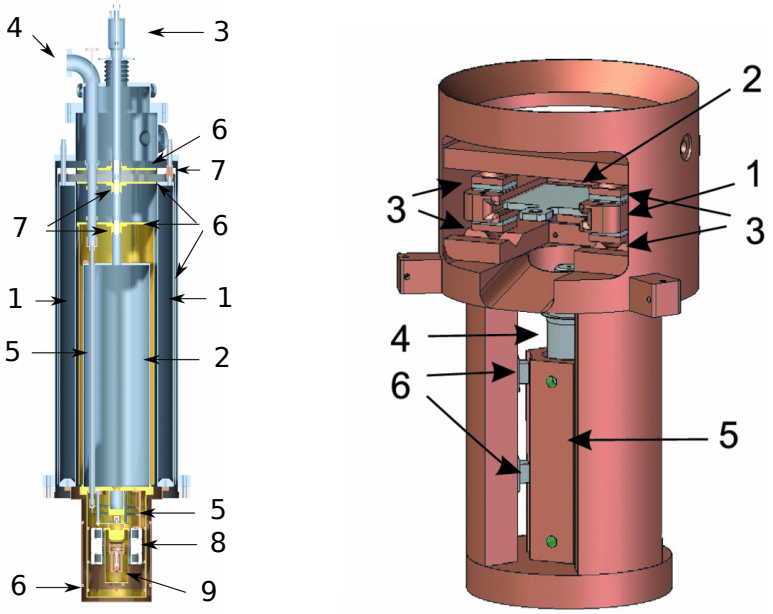

(a) JT cryostat **(b)** JT STM head

Figure 3.2: Cryostat and STM head of the JT setup. (a) The JT cryostat: LN_2 tank (1), LHe tank (2), LHe supply/exhaust pipe (3), in and out let of ^{3}He (4), countercurrent heat exchangers for ^{3}He (5), radiation shields (6), heat exchangers (7), superconductive coil (8) and STM head (9). (b) The JT STM: Sample stage (1), sample holder plate (2), piezo motor (x coarse motion) (3), piezo scanner with tip (4), copper prism (5) and piezo motor (z coarse motion) (6). Both images are adapted from reference [118]. Reuse was permitted by W. Wulfhekel.

elaborately in [118]. The STM heads of dilution [120] and 4K setup are designed similar and work according to the same principles.

Electronics

For executing all measurements and controlling all functions commercial *Nanonis* controllers with the corresponding software interface by *SPECS* were used. This includes all the relevant STM control procedures including (x, y, z)-positioning of the STM tips and scanning, the feedback loop, tunneling voltage, spectroscopy experiments, all data acquisition, the STM heaters

and the piezo motor control. In order to measure the tunneling current of the order of a few pA, commercial low noise current amplifiers by *Femto* are used. These amplifiers provide amplification factors up to 10^9 V/A at bandwidths of the order of 1 kHz. The output voltages are directly connected to the Nanonis systems and analogue lock-in amplifiers by *Princeton Applied Reasearch*. The latter are used for STS measurements as discussed in section 2.1. At the dilution system, the built-in lock-in module of the Nanonis system was used for STS measurements. Finally, the magnetic fields are controlled by commercial controllers by *Oxford Instruments*.

^{3}He/^{4}He Dilution Refrigeration

A ^{3}He/^{4}He dilution refrigerator is based on the thermodynamical properties of mixtures of the two isotopes at low temperatures [121, 122, 123]. Figure 3.3a illustrates schematically the most important features of the corresponding phase diagram: At low enough temperatures and ^{3}He concentrations the mixture is in a superfluid state, while on the right-hand side of the so-called λ-line, i.e. at high ^{3}He concentrations, it behaves like a normal Fermi liquid. The crucial point is, that below a critical temperature of $T_C = 870\,\text{mK}$ the two isotopes are not truly mixable. The phase separation yields on the one hand a phase with very high ^{3}He concentration, and on the other hand a ^{3}He-poor phase, the so-called *diluted phase*. Since the ^{3}He-rich phase has a lower density, it will float on top of the heavier diluted phase. Another specific feature occurs in the limit $T \to 0$: While the concentrated phase results in practically pure ^{3}He, the diluted phase approaches a finite ^{3}He concentration of roughly $x_0 = 6.5\,\%$, which is rather temperature-independent at low temperatures.

A dilution fridge exploits, that the transition of a ^{3}He atom from the concentrated phase through the phase boundary into the diluted phase is endothermic, such that thermal energy is drawn from the environment during the process. This process is similar to an evaporation process as the enthalpy of a ^{3}He atom is higher inside the diluted phase. Figure 3.3b shows a simplified schematic of a structure of a dilution refrigerator similar to the one of the dilution setup [120, 121]. First, the purified, compressed

mixture is stepwise pre-cooled by heat exchange with the LN_2 bath, the helium radiation shield and finally the LHe bath. Before the mixture enters a Joule-Thomson expansion stage in the next step, it is further cooled by heat exchange of return gas or the still. Due to the JT expansion the mixture condenses and accumulates in the mixer. In the steady-state operation, i.e. when enough mixture is condensed, the mixer contains both phases, the concentrated phase and the diluted phase, while the latter even reaches the still. The mixer is the coldest part of the cycle, since the cooling process, where ^{3}He passes the phase boundary, happens there. In the still the mixture can evaporate and is further pumped and fed back into the cycle. Since the vapor pressure of ^{3}He is significantly larger than the one of ^{4}He, the evaporating gas is almost pure ^{3}He. Consequently, as this evaporation process would lower the ^{3}He concentration in the diluted phase, new ^{3}He is drawn through the phase boundary in order to maintain a dynamic equilibrium. Thus, the circulating gas will be almost pure ^{3}He. It is now apparent, why it is beneficial, that the diluted phase maintains a finite, temperature-independent concentration of ^{3}He when approaching zero temperature. Like this the cooling power, which is determined by the rate of ^{3}He atoms passing the phase boundary, remains constant in this limit. Finally, it should be stressed, that the issue of heat exchange of the incoming mixture to several stages of the cycle is more subtle than this simplified picture and that this is very essential for the performance of a dilution refrigerator.

3.3 Sample Preparation

3.3.1 Subrate Preparation

Before growing the molecules that are supposed to be investigated, a clean, well-defined substrate surface has to be prepared first. This section describes the corresponding methods and procedures, that were used in this dissertation.

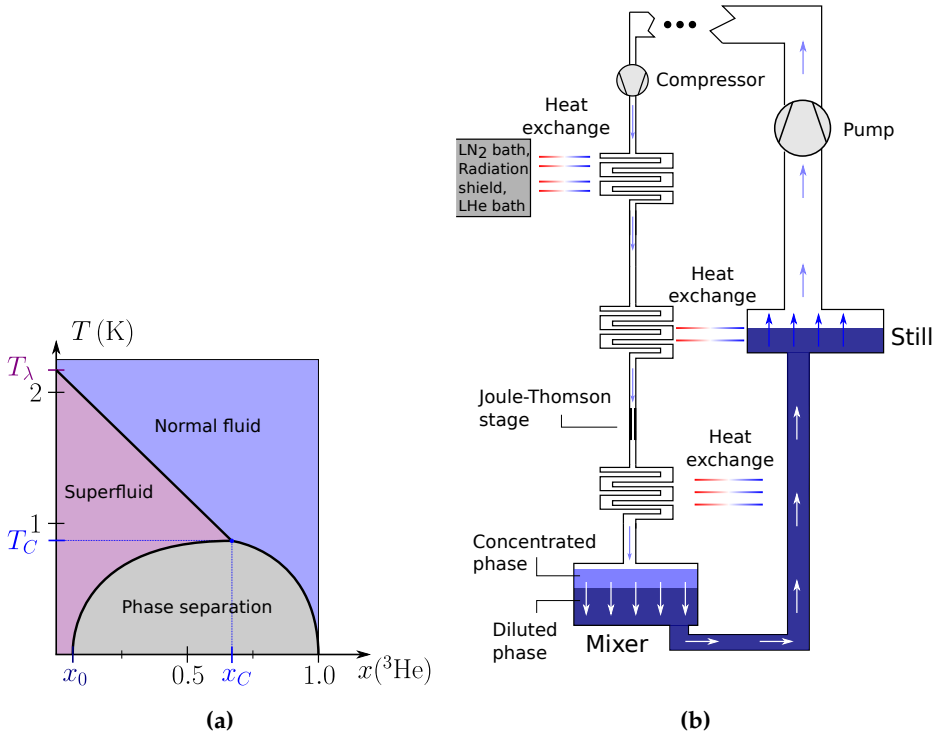

Figure 3.3: Helium phase diagram and structure of a dilution refrigerator. (a) A cartoon schematically shows the most important features of the phase diagram of a mixture of ^{3}He and ^{4}He. The axes correspond to the temperature T and the ^{3}He concentration x. The transition to a superfluid for ^{4}He occurs at $T_\lambda = 2.17\,\mathrm{K}$, while the critical point occurs at $T_C = 870\,\mathrm{mK}$ and $x_C = 0.67$. The smallest ^{3}He concentration in the diluted phase is $x_0 = 6.5\,\%$ [122, 123]. (b) A simplified structure of a dilution refrigerator is illustrated.

Single Crystals

Using a metallic single crystal as substrate, a clean and well-defined sample surface is usually achieved by several cycles of argon sputtering and annealing. Thereby, argon gas is introduced into the preparation chamber (pressures $\lesssim 1.0 \times 10^{-7}\,\mathrm{mbar}$). In the sputter gun the argon atoms are ionized and accelerated towards the sample surface by a high voltage (HV) of the order of $3\,\mathrm{kV} - 4\,\mathrm{kV}$. Due to the impact of the argon ions, their momentum is transferred to the atoms in the substrate surface, such that these may

be ejected. Typical parameters for one sputtering cycle are 30 min at a sputter current, i.e. the ion current reaching the sample surface, of about 2 µA. Thereby, eventually several atomic layers can be removed off the substrate surface. In order to maintain a low pressure in the preparation chamber during this process, the sputter gun is differentially pumped via the air lock when operated. After sputtering the sample surface is typically very rough. Therefore, the sputtered sample needs to be annealed, i.e. heated to several hundred degree Celsius, such that a smooth surface is regained by diffusion. Moreover, impurities are able to diffuse from the bulk to the surface, such that they can be removed by subsequent sputtering cycles. The sample heating is achieved by electron bombardement. For this purpose, a tungsten filament at the sample manipulator is heated by a current in order to achieve thermionic emission. The emitted electrons are accelerated towards the backside of the substrate by a high voltage, where they transfer their kinetic energy to the crystal so that the latter is heated. While the annealing procedure, the surface temperature of the crystal can be monitored using an infrared pyrometer. The used single crystals Au(111), Cu(111) and Cu(100) all were cleaned and prepared by several cycles of sputtering and subsequent annealing to 450 °C − 500 °C.

Fe_2N/Cu(100)

Before the preparation of a monolayer of iron nitride (Fe_2N/Cu(100)), the Cu(100) crystal first needs to be cleaned according to the aforementioned procedure. After the crystal is cooled down following the last annealing, nitrogen needs to be implanted into the copper surface first. This was achieved by sputtering the crystal with nitrogen at low energies such as 650 eV. In the next step, approximately one monolayer of iron was deposited on the sample surface using an iron evaporator. In the last step, the crystal is mildly annealed to about 325 °C. Thereby, the implanted nitrogen diffuses to the surface and together with the deposited iron the desired monolayer of iron nitride is formed. It turns out that both, the precise annealing temperature as well as the amount of iron deposited are crucial for the result. In fact, too low temperatures can result in a rather rough surface or numerous defects. Too high temperatures presumably cause too much desorption of

nitrogen, while excess iron may diffuse underneath the iron nitride layer and aggregate [124]. Unfortunately, during the course of this work, the rather complex growth of $Fe_2N/Cu(100)$ could not be fully understood. However, the monolayer iron nitride exhibits a very characteristic atomic reconstruction which can be identified in topography scans with atomic resolution. Figure 6.5b in chapter 6.2 shows such an image for a successfully prepared sample. Thereby, the quality of the iron nitride film could still be ensured for those samples whose results are presented in chapter 6.2. The properties of $Fe_2N/Cu(100)$ and why it is interesting as a substrate shall also be discussed in this chapter.

It should be mentioned, that there were problems regarding the temperature measurement using the pyrometers. Since the measured temperatures are determined by the measured intensity of thermally emitted infrared radiation of one certain wavelength, the result can be different for different sample pyrometer geometries, for instance, when the sample is not exactly in the focus plane of the pyrometer. Unfortunately, since especially in the JT setup both, sample and pyrometer position and alignment are not fixed, the measured temperatures during an annealing process are not fully reproducible. Moreover, the minimum emissivity that can be set for the used pyrometers is still too high for the used single crystals. These issues not only complicate the comparison to temperatures measured at different setups, but also hamper the replication of simple recipes from literature. While these problems are rather unimportant for preparing the single crystal surfaces, it did cause problems for the preparation of the monolayer $Fe_2N/Cu(100)$, such that the latter could not be achieved in a reproducible manner. Here, another approach where a constant HV and constant emission current are applied over a fixed amount of time, turns out to be more reproducible. Applying 850 V at an emission current of 1.6 mA for 3 min was used for the successfull Fe_2N sample presented in figure 6.5b in chapter 6.2.1.

Lanthanum Strontium Manganate Thin Films

The lanthanum strontium manganate ($La_{1-x}Sr_xMnO_3$, short LSMO) thin film samples used in this work were prepared at Fudan University in the group of Prof. Jian Shen. They consist of roughly 30 monolayers of LSMO, epitaxially grown on niobium-doped strontium titanate (STO) using pulsed laser deposition (PLD). The strontium ratio is close to the optimal concentration of $x = 0.3$ [125], while the surface is oriented along the $\langle 001 \rangle$ direction. The epitaxial layer-by-layer growth was monitored using a *reflection high energy electron diffraction* (RHEED) system. Since LSMO is an oxide, its surface is expected to be rather inert and robust, such that the ex-situ transfer to the 4K setup was not considered a problem. After introducing the LSMO samples into the 4K setup, they were degassed by annealing, using only the manipulator filament without HV. Thereby, a constant current of 1.5 A was applied for 30 min, such that the manipulator reached a temperature of roughly 118 °C. It is estimated, though, that the actual sample temperature was significantly higher than this.
Both, Kerr measurements and the growth of Fe-Pyrz molecules on this LSMO substrate were performed at the 4K setup. Unfortunately, it was not possible to perform STM measurements to characterize the LSMO sample and its molecular coverage, because its surface was too rough. At last, the finished Fe-Pyrz/LSMO sample was transferred to the WERA beamline at the ANKA synchrotron using a vacuum suitcase. This procedure is described in more detail in section 3.5.

3.3.2 Molecule Deposition

The molecular deposition is typically the last step of the sample preparation. For this purpose the molecules, that are available as powder, are sublimed using a molecular evaporator and deposited on the previously cleaned sample surface from the gas phase. Typically, deposition rates smaller than 1 ML/min are chosen, such that sub-monolayer coverages can easily be achieved. Before the deposition, however, the molecule powder needs to be degassed in order to get rid of impurities. Usually this is achieved by heating the crucible to temperatures below the deposition temperature for

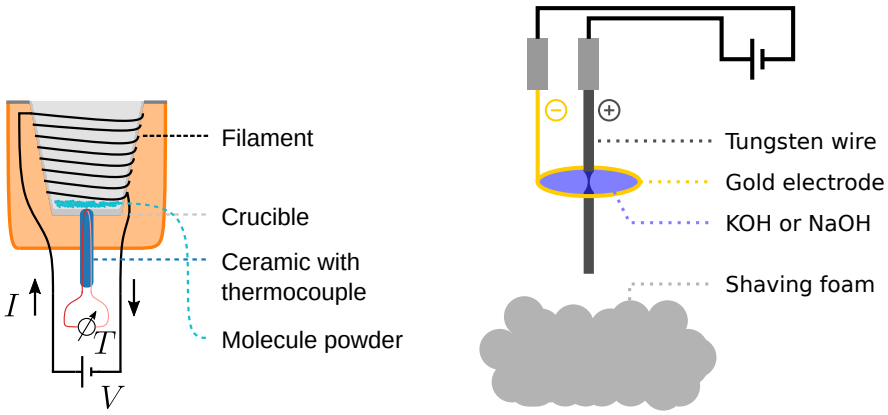

(a) Molecular evaporators **(b)** Tip etching process

Figure 3.4: Structure of the molecular evaporators and tip etching process

awhile.

The working principle of the used evaporators is sketched in figure 3.4a: A crucible containing the molecule powder is heated by a filament up to the sublimation temperature of the molecule powder. The temperature measurement is carried out by a thermocouple on which the crucible stands. Usually, the crucible temperature is controlled by a PID controller, that regulates the heating power according to the discrepancy of the measured temperature compared to the given setpoint. Also, heating the filament with a constant current for awhile until the crucible reaches a stable temperature is possible. In either case, an accurate temperature control, such that the crucible temperature is higher than the required sublimation temperature, but lower than any dissociation temperature, is crucial for this process. One basic difficulty here is, that the exact sublimation temperature of a compound is often unknown. Furthermore, a direct comparison with literature or temperatures measured in other evaporators is often hindered, since this kind of temperature measurement appears to be not very accurate.

Concerning the two molecular evaporators, that were used during the majority of this work, two additional issues occurred: Firstly, the crucibles made from Al_2O_3 are comparatively wide, which hinders their thermaliza-

tion and therefore the temperature stabilization. Moreover, the relatively large crucible surface gives rise to a higher amount of impurities.
Secondly, the way bigger challenge was, that the measured temperatures did not seem to be very reproducible. Arguably, this originates from the non-rigid thermal contact between the crucible and the thermocouple, that may be different any time the crucible is removed for being cleaned and loaded.
In the final stages of this work, when a whole new evaporator with a thinner crucible form quarz glass and a well-defined crucible geometry was used, both of theses issues improved significantly. Nevertheless, it should be pointed out, that the temperatures used for the deposition, that are given in table 3.1, should be treated with caution and give merely an idea for the correct order of magnitude.

Table 3.1: Deposition and degassing parameters

Compound	$T_{\text{Deposition}}$ (°C)	T_{Degas} (°C)	Evaporator type*
$DyPc_2$	400	350	2,3
Fe-Phen	170	150	2
Fe-Pyrz	175	125	3
$Cr(acac)_3$	48-62	62-70	1
$Co(acac)_3$	44	44	1

*Evaporator 1 is homebuilt. Evaporator 2 is a commercial evaporator by *CreaPhys*. Evaporator 3 is a commercial evaporator by *Kentax* (point source $Q5_L$).

3.4 Tip Preparation

The STM tips used in this work were all made from tungsten and were prepared according to the following protocol: In the first step, the tip is etched from a tungsten wire using an alkaline solution of NaOH or KOH ($c \sim 1\,\text{mol/L}$). For this purpose, a setup like the one illustrated in figure 3.4b

was used, where the wire is placed inside a ring-shaped counter electrode from gold. The applied DC voltage is of the order of 5 V. By short-time immersion into the etching solution, a thin meniscus in formed, such that the wire is only etched within this thin region. While the wire is getting thinner gradually due to the etching process, there is additionally a constant tensile force caused by the weight of the tungsten wire, until eventually the latter is split into two very sharp parts. Meanwhile, the falling part is safely caught by shaving foam.
After transferring the tip into UHV using a suitable tip holder, in the next step the insulating oxide layer needs to be removed. This so-called *flash* process works analogue to the sample annealing by electron bombardement: Electrons are emitted from a heated filament and hence accelerated towards the tip apex by a HV. Typical parameters for this procedure are a HV of 1 kV at emission currents of $50 - 100$ mA for short times smaller than 1 s. Thereby, the tip is heated to several thousand degree Celcius for a very short time, such that the oxide layer evaporates and possibly the tip even melts partially. Due to this heating, however, impurities such as carbon may diffuse from the bulk to the surface, where insulating tungsten carbides may be formed. The latter can be removed by subsequent argon sputtering. Usually, several cycles of back-to-back flashing and sputtering are performed, before eventually the tip can be transferred in-situ to the STM after a final mild flash.

The ferromagnetic tips with out of plane anisotropy, that were used for sp-STM, were first prepared according to this protocol, too. After a last moderate flash, additionally 20 ML of cobalt were deposited on the tungsten tip. Last, the tip was *soft-annealed* by applying only a moderate current to the filament of the manipulator without any HV (roughly 30 s with the filament glowing in orange). Analogously, for the antiferromagnetic tips with out of plane anisotropy an estimated 33 ML of chromium were deposited on the cleaned tungsten tip, which was soft-annealed subsequently for 90 s. In fact, the success rate of getting an actual spin-polarized tip, which is suitable for the experiments presented in chapter 4, is not too high, such that several preparation attempts were necessary. Thus, before the actual spin-polarized measurement the tips were tested on a well-studied reference system of Co/Cu(111) [55] first.

3.5 WERA Beamline and Sample Transfer

The x-ray absorption measurements on SCO molecules (Fe-Pyrz/LSMO), that are presented in chapter 6.3 were performed at the WERA beamline of the ANKA synchtrotron in Karlsruhe. This beamline operates according to the principles described in chapter 2.5: The synchrotron radiation is provided by a bending magnet. Accordingly, the beam polarization is chosen by the vertical position of the beamline aperture. A grating, i.e. a textured surface, where the x-rays are diffracted, serves as a monochromator. By choosing the correct diffraction angle, the energy of the beam that reaches the sample can be determined. Additionally, it is possible to vary the widths of the entrance and exit slit of the monochromator: A larger opening yields higher x-ray intensities, however, at the expense of a worse energy resolution. Furthermore, in order to avoid any kind of hystersis effects of the monochromator fine motors, a fast reference spectrum of a well-known sample is acquired as energy calibration, before every measured spectrum. The end station consists of a vacuum setup including an air lock. During a measurement, the sample is located in UHV in the center of a superconductive fast-ramping coil, that can provide $\pm 7\,\mathrm{T}$ of magnetic field along the beam direction. Finally, the sample manipulator can be cooled down to roughly 20 K by continuous flow cooling using liquid helium. All measurements in this work were performed in the total electron yield mode.

The outstanding feature of these experiments was, that the investigated sample was prepared in the 4K setup and subsequently transferred to the beamline using a vacuum suitcase. The structure of this suitcase is depicted in figure 3.5. It consists of a sample manipulator mounted on a small hollow space with a UHV valve. In the process, the suitcase is flanged to the air lock and pumped first. After the pre-pumping process, the sample can be transferred from the UHV setup into the suitcase. After closing the valve, the suitcase including the sample can be unmounted an transferred to another vacuum setup. In the meantime, an adsorption pump made from a commercial getter material (SAES pump) is supposed to uphold the pressure inside the suitcase.
The sample transfer of the Fe-Pyrz/LSMO sample presented in chapter

6.3 required roughly 1.5 h. At the beamline, the valve to the suitcase was opened at an airlock pressure of 3.7×10^{-7} mbar. Since the airlock pressure dropped upon opening the valve, it is reasonable to assume, that the pressure inside the suitcase during the transfer was lower and of the order $p \lesssim 1.0 \times 10^{-7}$ mbar.

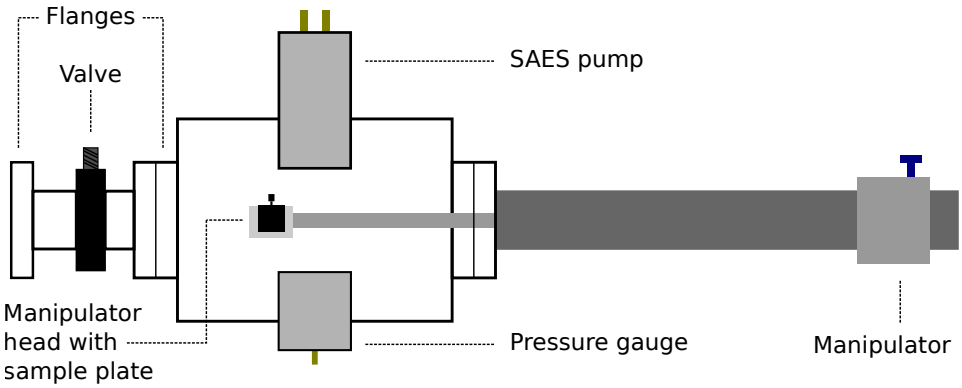

Figure 3.5: Structure of the vacuum suitcase. An adsorption pump is supposed to uphold the pressure during the transfer. A cold cathode ionizatiaon gauge is mounted to monitor the pressure.

4 Bis(phthalocyaninato)dysprosium Molecules

Rare earth systems are particularly interesting prospects for single-molecule magnets, because the 4f electrons are rather localized, meaning that the radial part of their wave function decays faster compared to 5p or 6s orbitals [92]. As one consequence, one expects on the one hand, that the 4f magnetic moment experiences less external perturbations and hence that it is in general rather stable. Another advantage is that the orbital angular momentum is not quenched, since spin-orbit interaction is stronger than the crystal field in these systems. This often results in larger magnetic moments and often larger zero field splittings. Therein however, also lies one inherent difficulty. Just because of this localized character of 4f electrons, they hardly participate in electronic transport through the molecule, which makes them invisible to STM. Therefore, it is usually not possible to address or read out the 4f moment of a molecule just like that.
This project, though, aims just exactly at the readout of the 4f magnetic moment of *bis(phthalocyaninato)dysprosium* double-decker molecules ($DyPc_2$) [126]. The basic idea of how to address the 4f moment of the dysprosium spin in STM nevertheless originates from previous reports on the analogue $TbPc_2$ molecules [16, 127, 128]. Following a brief introduction of the $DyPc_2$ molecules and their magnetic properties, a short review on those reports on $TbPc_2$ will be given, from which it directly follows the idea for this project. Afterwards the experimental results will be presented.

4.1 The Molecule Properties

The investigated $DyPc_2$ molecules consist of a central dysprosium ion sandwiched by two phthalocyanine (Pc) rings, that are rotated against each other by roughly 45° [129, 130]. Its structure is shown in figure 4.1a. Assuming, that the dysprosium ion is trivalent (Dy^{3+}) and exhibits the electron configuration of [Xe]$4f^9$, the magnetic ground state is given by the multiplet with quantum numbers $|J, L, S, J_z\rangle = |15/2, 5, 5/2, J_z\rangle$ according to Hund's rules. Accordingly, this is a Kramers system with half-integer total angular momentum. It should be noted, that the total angular momentum J of dysprosium will be simply referred to as dysprosium spin in the following. The ligand field parameters and the corresponding spin spectrum of $DyPc_2$ were determined in [129] by susceptibility and NMR measurements. The resulting spectrum is plotted in figure 4.1b. The quantization axis (z-axis) is chosen perpendicular to the Pc rings. The Kramers doublet with $J_z = \pm 13/2$ is energetically lowest, while the two respective states are separated from each other by an energy barrier of roughly 68 meV, which makes the $DyPc_2$ an interesting prospect for a SMM [126].
It should be noted, though, that some idealized assumptions were made in this respect. In addition to the fourfold rotational symmetry of the $DyPc_2$ molecules, the higher symmetry group D_{4d} was assumed. This corresponds to the case that the two Pc rings are parallel to each other and are skewed by exactly 45°. The consequence is that the spin Hamiltonian consists only of terms with Stevens operators $\hat{O}_k^q$ with $k \in \{2, 4, 6\}$ and $q = 0$ (see section 2.4.3). Consequently, J_z remains a good quantum number such that the lifetime of the two states $|\pm 13/2\rangle$ is expected to be very long.

In reality though, the D_{4d} symmetry is only almost fullfilled, such that the coefficients of the operators $\hat{O}_4^4$ and $\hat{O}_6^4$ are indeed very small, but finite. Consequently, the states $|J_z\rangle$ get mixed with states $|J_z \pm 4\rangle$. Another crucial aspect concerning the stability of the dysprosium spin J is the hyperfine interaction with its nuclear spin I. Interestingly, several stable dysprosium isotopes exist, that may exhibit a nuclear spin of either $I = 0$ or $I = 5/2$, such that two qualitatively different cases need to be distinguished [15, 131]: The nuclear spin singlet ($I = 0$) on the one hand, corresponds to the above

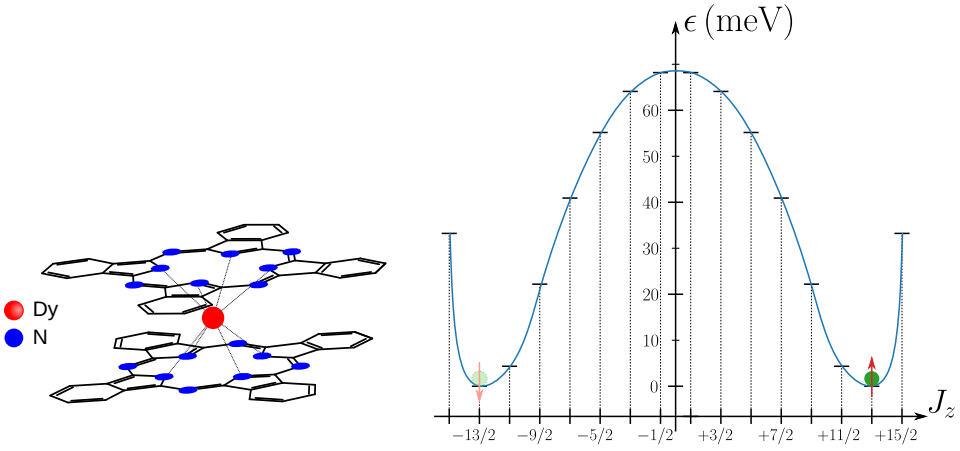

(a) $DyPc_2$ structure **(b)** Zero field splitting of $DyPc_2$

Figure 4.1: Structure and zero field splitting of the $DyPc_2$ molecules. The energies of the Kramers doublets were determined in [129] assuming that the molecule exhibits D_{4d} symmetry.

discussed simplified case. Here the two states $|\pm 13/2\rangle$ must remain degenerate in the absence of an external magnetic field due to Kramers theorem, regardless of the off-diagonal elements in the crystal field Hamiltonian (see figure 4.2a). Thus, no avoided crossing, where the two states mix, occurs and long lifetimes are expected for the two ground states.
In the case of a finite nuclear spin of $I = 5/2$, however, the hyperfine interaction yields a qualitatively different situation. The coupling $13/2 \otimes 5/2$ results in an integer total spin, such that some degeneracy points feature an avoided crossing due to the operators $\hat{O}_4^4$ and $\hat{O}_6^4$, which in turn enables quantum tunneling of magnetization (QTM). This is illustrated in figure 4.2b. Since these operators may only mix states with $\Delta J_z = 4, 8, 12, ...$, five such transitions with $J_z = -13/2 \rightarrow J_z = +13/2$ occur, where also the nuclear spin changes by one unit $I_z \rightarrow I_z - 1$ [131]. Accordingly, the lifetime of the electronic spin should become small every time the external magnetic field hits such a degeneracy point.
In fact, this qualitatively different behavior was reported for two samples of isotopically enriched $DyPc_2$, containing either ^{163}Dy ($I = 5/2$) or ^{164}Dy ($I = 0$). For the nuclear spin singlet ($I = 0$) longer relaxation times and

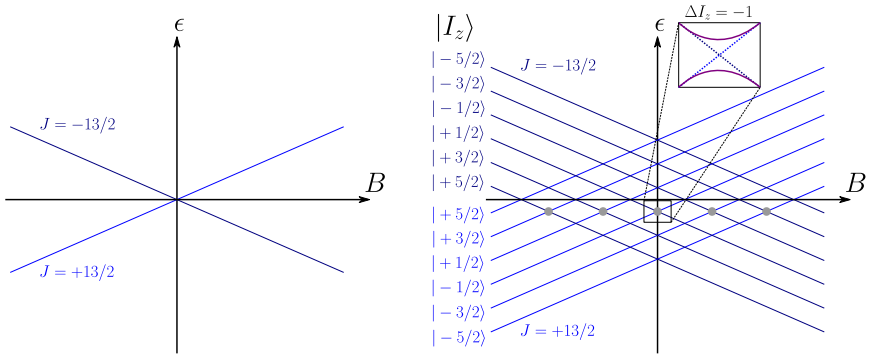

(a) $I = 0$ **(b)** $I = 5/2$

Figure 4.2: Zeeman diagram for the ground state doublet of $DyPc_2$. (a) Without nuclear spin the two states of the ground state doublet remain degenerate at zero magnetic field. (b) With a finite nuclear spin of $I = 5/2$ five points occur, where QTM is possible with $\Delta m_I = -1$ [15, 131]. In reality, the hyperfine levels are not equidistant due to the quadrupole interaction.

wider hysteresis curves were observed [15]. The same behavior was reported for a different SMM based on dysprosium [132]: Again the molecules from enriched dysprosium with no nuclear spin (^{164}Dy) showed slower relaxation than those with $I = 5/2$ (^{161}Dy). Thus, SMMs containing only isotopes with $I = 0$ generally seem to be more suitable to serve as classic bits. Though, even in this case non-thermal spin relaxation processes occur due to either dipolar interactions or hyperfine coupling to nitrogen nuclei from the ligands [15, 132]. On the other hand, though, the case of a finite nuclear spin offers intriguing prospects for applications as qubits [15]. This issue will be picked up again later in this chapter.

4.2 Previous Works on $TbPc_2$ and Project Idea

The underlying idea for this project of how to address the 4f magnetic moment of dysprosium originates from two previous reports on the analogue $TbPc_2$ molecules [16, 127], where the dysprosium is substituted by a terbium ion. In contrast to Dy^{3+}, the Tb^{3+} exhibits an even number of 4f electrons, such that it is not a Kramers system. Nevertheless, the $TbPc_2$ features a

ZFS that is quite suitable for the use as SMM [129]. Effectively, this system behaves similar to an Ising system, where the magnetic properties at low temperatures entirely depend on the two states $|\pm 6\rangle$, that are roughly 54 meV lower in energy than the residual states in the multiplet.

Firstly, Komeda et al. investigated these $TbPc_2$ molecules with STM on Au(111) at roughly 4.7 K [127]. They found that the molecules show a very characteristic shape in topography (figure 4.3a) and arrange in islands in a checkerboard-like pattern of alternative skewing angles of the top Pc ligands. Interestingly, those molecules with a 45° angle show a clear Kondo resonance (figure 4.3b). This resonance however, cannot be observed in the molecule's center, where the terbium ion is located, but it occurs only on the lobes of the top Pc ligand. Therefore, it was concluded in this report, that this Kondo resonance does not originate from the terbium magnetic moment being screened by the conduction electrons of the gold substrate, but that it originates from one unpaired electron on one of the Pc ligands. This unpaired spin 1/2, was referred to as *singly occupied molecular orbital* (SOMO). Hence, the molecules behave like a quantum dot with an uneven number of electrons. Moreover, it was observed, that by applying too high tunneling currents, the Kondo resonance disappears upon a rotation of the top Pc ligand. This is presumably caused by a change of the molecule's charge state that accompanies the rotation.

Secondly, Vincent et al. investigated this $TbPc_2$ in a break junction [16]. Using a gate electrode, they were able to tune the molecule's charge state. Thereby, depending on the gate voltage, they would either end up with the molecule in a Coulomb blockade regime - which reflects an even number of electrons on the quantum dot - or in the Kondo regime with an unpaired spin 1/2 equivalent to the molecules on Au(111).
Interestingly, they observed a ferromagnetic exchange interaction between the unpaired spin of the SOMO and the 4f moment of the terbium. This could be exploited to detect spin flips of the terbium magnetic moment as function of the magnetic field (figure 4.4) and even distinguish the different nuclear spin transitions of terbium. Since the terbium nuclear spin is $I = 3/2$, there are transitions only at four different values for the applied magnetic field, corresponding to the four crossing points with $\Delta m_I = 0$.

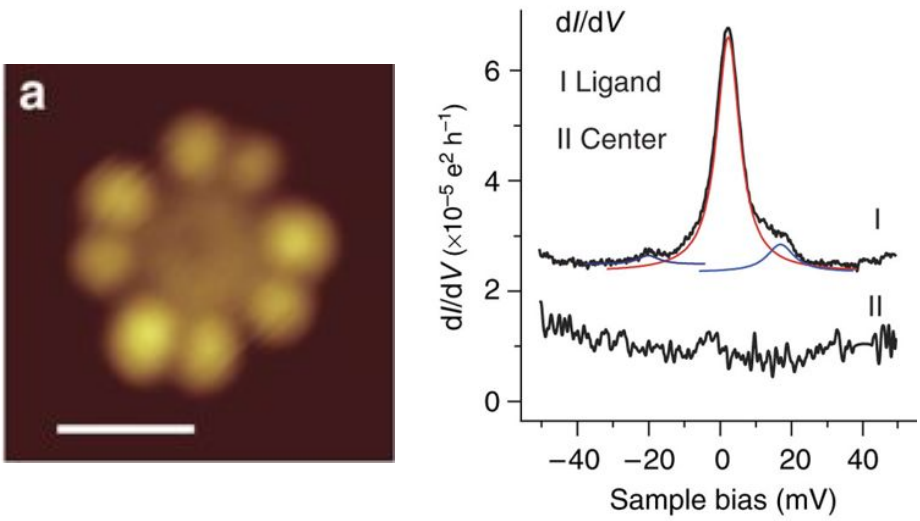

(a) Topography of $TbPc_2$ **(b)** Kondo resonance of $TbPc_2$

Figure 4.3: A single $TbPc_2$ molecule on Au(111). (a) The topography of a $TbPc_2$ molecule on Au(111) is shown. The scale bar corresponds to 1 nm. (b) Differential conductance spectra are shown. The Kondo resonance only occurs on the lobes of the top Pc ligand but not in the center of the molecule. Both images are adopted from [127].

Moreover, it was shown that the lifetimes of the terbium nuclear spin states are of the order of several tens of seconds [133] with coherence times of the order of milliseconds [19] such that they could even serve as qubits for implementing Grover's algorithm [19]. Finally, this readout method for the terbium electronic spin for $TbPc_2$ in a gated break junction was demonstrated again in the same group [128].

From these reports it directly follows the underlying idea of this project, which is illustrated in figure 4.5. With STM one can only observe the SOMO via the aforementioned Kondo resonance, when the molecules are deposited on Au(111). The SOMO S now should exhibit an exchange interaction with the dysprosium magnetic moment J. So if S and J interact, this can be exploited in order to address J indirectly via S. If these assumptions all hold true, one expects the Kondo resonance to be split because of this exchange interaction, that should have the same effect on the spin 1/2 as an external magnetic field. How this scheme could be exploited in order to read out

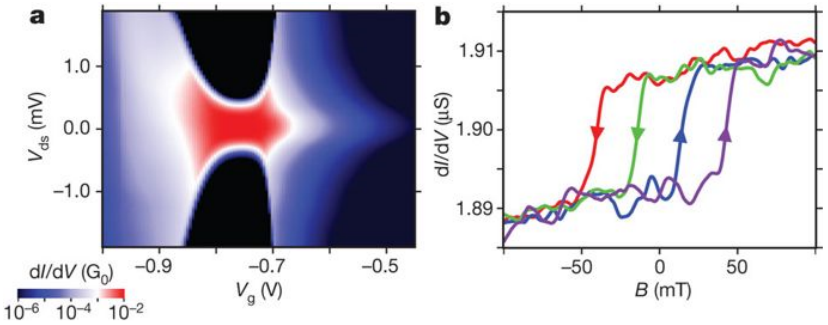

Figure 4.4: Transport through the $TbPc_2$ molecule in a gated break junction. Depending on the gate voltage, the molecule is either in a Coulomb blockade regime or a Kondo regime (left). The conductance as function of applied magnetic field with both gate voltage and source-drain voltage being fixed is shown on the right. Jumps in the conductance correspond to spin flips of the terbium moment. The four different transitions correspond to the four different nuclear spin transitions of terbium. Both images are adopted from [16]. Reuse was permitted by W. Wernsdorfer.

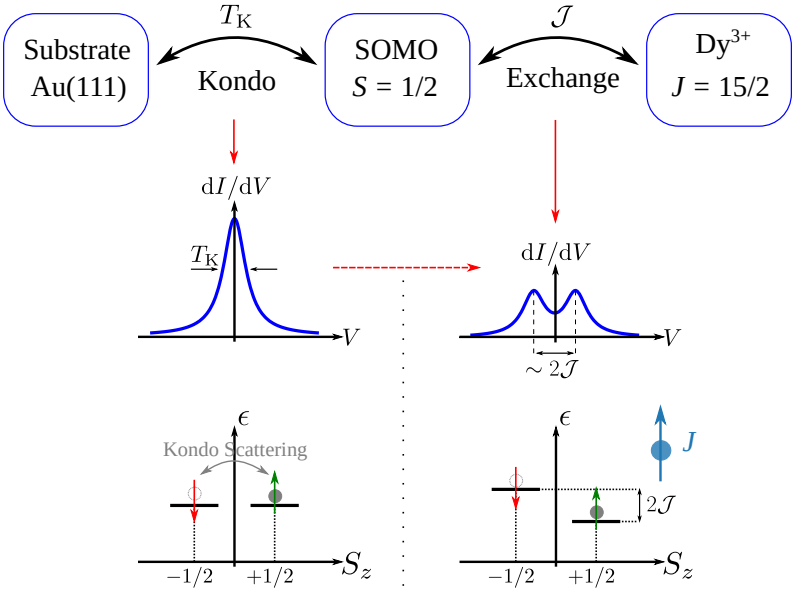

Figure 4.5: Basic idea of how to address the dysprosium magnetic moment in STM.

the dysprosium spin J using sp-STM will be shown later in this chapter in section 4.4.

4.3 Kondo Effect of $DyPc_2$/Au(111) and Exchange Splitting

Results from the JT STM

First of all, the $DyPc_2$/Au(111) system was investigated in the JT STM at roughly 850 mK. Figure 4.6 shows topography scans of a typical sample and a single $DyPc_2$ molecule. Similar to normal phthalocyanine molecules the $DyPc_2$ molecules show the typical flower-like shape.

In spectroscopy the molecules show a clear Kondo resonance as shown in figure 4.7. In accordance with the previous reports on $TbPc_2$/Au(111) [127], this resonance can only be observed on the lobes of the top Pc ligand, while the spectrum in the center of the molecule shows no real feature and resembles the one acquired on the gold substrate. Furthermore, a Frota function (see section 2.3.3) was fitted to the resonance. From the fit, the half width at half maximum of the peak Γ yields

$$\Gamma = (0.52 \pm 0.01)\,\text{meV}. \tag{4.1}$$

It should be mentioned, though, that this width is presumably dominated by the experimental broadening, as will be seen later. Therefore, the Kondo temperature of this system cannot simply be derived from this fit using equation 2.32. This issue will be discussed more elaborately later in this section.

The measurement in figure 4.8 is supposed to illustrate the localization of the Kondo resonance. For that matter, $\mathrm{d}I/\mathrm{d}V$-spectra were measured on a molecule inside a molecular island along the superimposed line. Clearly, the resonance is very localized on the two lobes, while it is absent in the molecule's center.

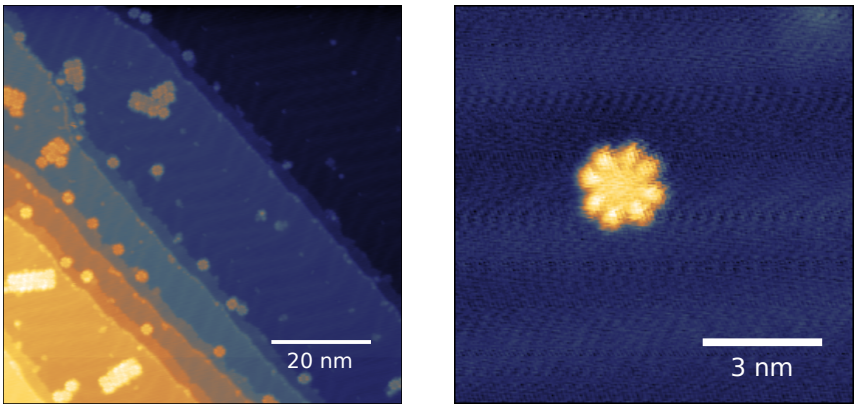

(a) $-1\,\mathrm{V},\ 100\,\mathrm{pA}$ **(b)** $1\,\mathrm{V},\ 5\,\mathrm{pA}$

Figure 4.6: Topography scans of $DyPc_2$/Au(111).

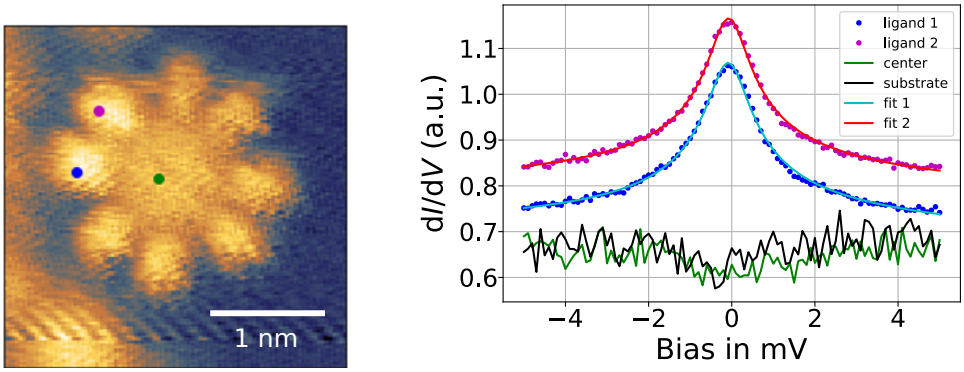

(a) **(b)**

Figure 4.7: STS on a single $DyPc_2$ molecule. (a) The location of the acquired spectra is shown. (b) The Kondo resonance only occurs on the lobes of the top Pc ligand. Frota functions were fitted to the resonance. Topography parameters: $(0.1\,\mathrm{V},\ 5\,\mathrm{pA})$, $3\,\mathrm{nm} \times 3\,\mathrm{nm}$. Lock-in parameters: $0.1\,\mathrm{mV}$ modulation at $2.55\,\mathrm{kHz}$.

Finally, the behavior of the Kondo resonance inside of molecular islands was investigated. As illustrated in figure 4.9, there are some molecules that do not show the Kondo effect. It seems like molecules on the border show the Kondo effect, while it is absent for molecules in the inside. However, a more elaborate study would be necessary for any reliable conclusion. One possible explanation for the absence of the Kondo effect might be, that the unpaired spin 1/2 of neighboring molecules pair up to singlets.

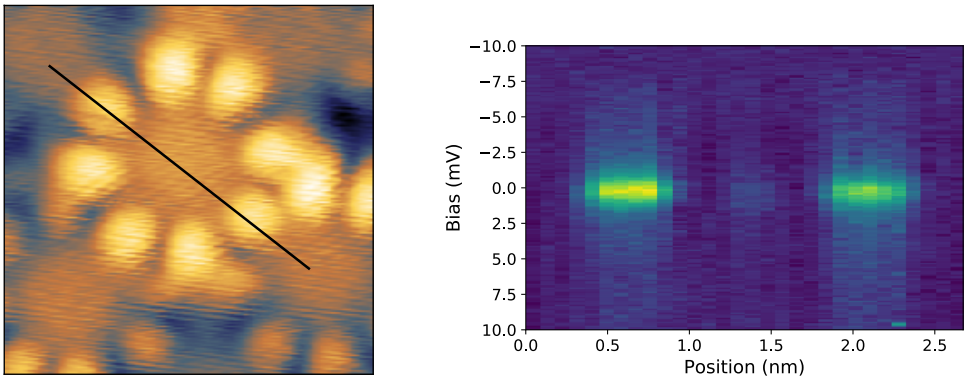

Figure 4.8: Localization of the Kondo resonance. $\mathrm{d}I/\mathrm{d}V$-spectra were measured along the black line in (a) and are plotted as function of position in (b). Topography parameters: $(0.1\,\mathrm{V},\ 10\,\mathrm{pA},\ 3\,\mathrm{nm} \times 3\,\mathrm{nm})$. Lock-in parameters: 0.5 mV modulation at 1.44 kHz.

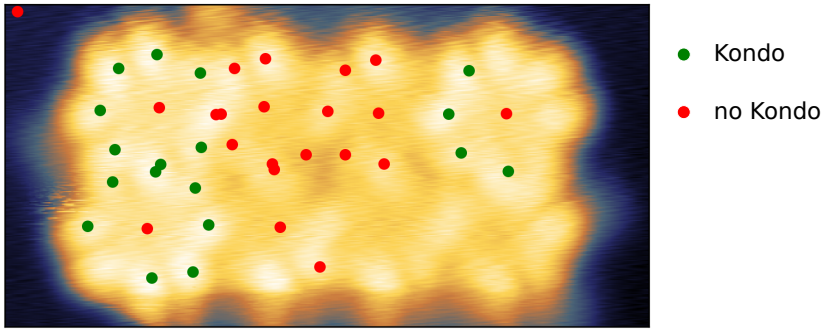

Figure 4.9: Kondo effect inside a molecular island. A Kondo resonance was measured only at the spots marked in green. At the spots marked in red no Kondo resonance was observed. Topography parameters: $(1\,\mathrm{V},\ 10\,\mathrm{pA},\ 8\,\mathrm{nm} \times 4\,\mathrm{nm})$.

Results from the dilution STM

Since the experimental broadening of the presented spectra is too large to observe a possible exchange splitting of the Kondo resonance, this system was subsequently investigated in the dilution STM at roughly 40 mK, where the energy resolution is almost one order of magnitude better. Figure 4.10 shows the resulting enhanced spectrum where indeed a splitting of the Kondo resonance can be observed. It should be pointed out that this is in the absence of any external magnetic fields, such that this splitting indeed originates from the ferromagnetic exchange interaction between the SOMO and the dysprosium spin J. Revisiting the scheme in figure 4.5 reveals, that these results are exactly what had been expected in the first place: First, the Kondo effect because of the screening of the unpaired spin 1/2 on the Pc ligand, and then at sufficiently high energy resolution, the splitting of the Kondo resonance because of its exchange with the dysprosium magnetic moment J.

In the next step it is shown, that what was observed is indeed the Kondo effect by measuring the splitting as function of the applied magnetic field (in z-direction). The result is shown in figure 4.11a. Since a few hundred mT are already enough to fully align the dysprosium spin J along the external magnetic field at such low temperatures, the energy difference between spin up and spin down configuration of the SOMO spin S and simultaneously the width of the splitting are expected to gradually increase as the magnetic field increases, as illustrated in the cartoon in figure 4.11b. Indeed, the splitting gradually increases upon the increase of the applied magnetic field. These spectra can be fitted to the model of Ternes [86], that calculates the shape of the tunneling spectra by third order perturbation theory (see section 2.3.3). Thereby, a single spin 1/2 system was assumed, where the exchange splitting was treated as an offset B_0 in the z-component of the magnetic field. Like this the fit yields for the exchange field, the Landé factor and the effective temperature

$$B_0 = (422 \pm 20)\,\mathrm{mT} \tag{4.2}$$

$$g_S = (1.85 \pm 0.02) \tag{4.3}$$

$$T = (206 \pm 10)\,\mathrm{mK}. \tag{4.4}$$

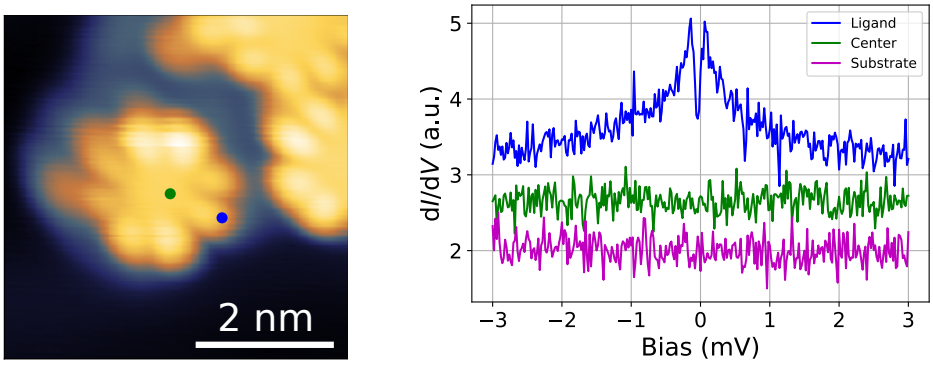

(a) (b)

Figure 4.10: Exchange splitting of the Kondo resonance. (a) The locations of the acquired spectra are shown. (b) The Kondo resonance is split. Topography parameters: (1 V, 10 pA). Lock-in parameters: 50 µV modulation at 1.4 kHz.

The small deviation of the Landé factor from the value of $g_{JLS} = 2$ is expected for a delocalized spin 1/2, that is smeared over the Pc ligand. Still small deviations might also be related to the calibration of the coil. The fitted temperature of roughly 200 mK corresponds to the experimental broadening due to the relatively high lock-in modulation.

It is apparent that the analysis, that uses the perturbative model by Ternes [86], is contradictory to the fit of the Frota function, that was applied before to the data acquired at the JT STM. In fact, the assumption that this Kondo system is in the strong coupling regime, where the DOS can be described by the Frota function (chapter 2.3.3), may therefore not be justified. Accordingly, there is not really a physical justification for this previously performed Frota fit and it should be merely regarded as a means to determine the width of the peak.

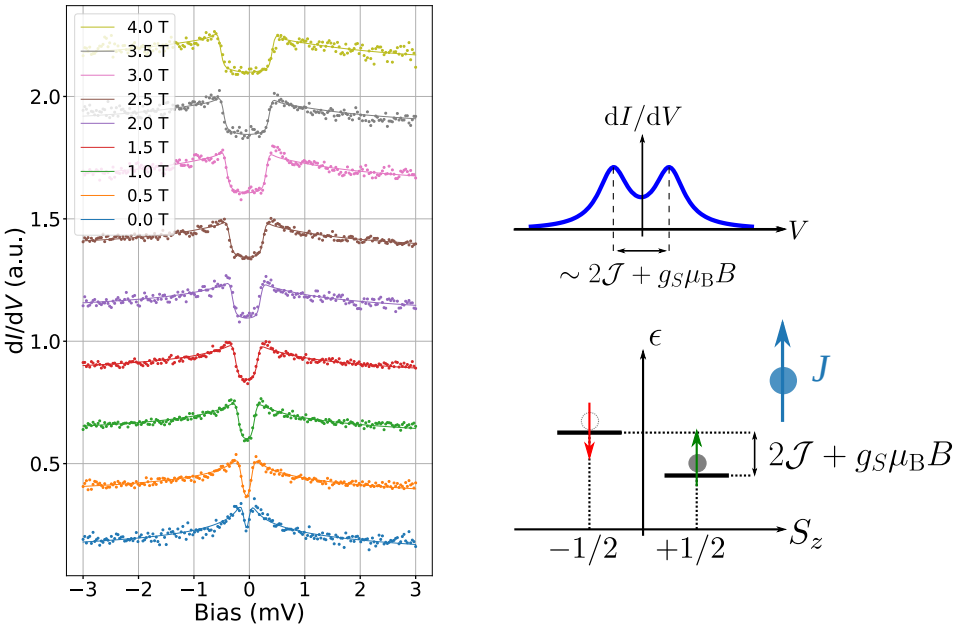

(a) **(b)**

Figure 4.11: Splitting as function of the applied magnetic field. (a) The measurements (points) including the fits (solid lines) for various applied magnetic fields are shown. (b) The cartoon illustrates how the width of the splitting increases gradually as the magnetic field increases. Lock-in parameters: 80 µV modulation at 1.4 kHz.

4.4 Spin-Polarized Measurements and Spin Readout

With these results, it is apparent, that the readout of the dysprosium angular momentum J should be possible using spin-polarized STM. Thereby, one would exploit that the two peaks of the split Kondo resonance are fully spin-polarized [134], as illustrated in the left column of figure 4.12. The basic idea of how the readout works is also depicted in this figure. Assuming the STM tip is spin-polarized with spin up being the majority spin, the respective peak with $S_z = +1/2$ is expected to be higher than the one of opposite spin orientation with $S_z = -1/2$. For instance, if the

applied magnetic field points in the positive z-direction (middle column), the state with $S_z = +1/2$ will be higher in energy and accordingly the peak above the Fermi level (i.e. at positive bias) will be higher. Conversely, if the magnetic field direction is inverted (right column), the opposite spin orientation with $S_z = -1/2$ will be higher in energy and the two peaks swap roles, such that now the peak below the Fermi level (i.e. at negative bias) is higher.
Accordingly, the asymmetry of the two peaks directly shows the orientation of the spin 1/2 and due to the strong ferromagnetic exchange interaction also that of the dysprosium magnetic moment. Therefore, by measuring this asymmetry as function of the applied magnetic field, one can directly acquire the magnetization curve of dysprosium. Interestingly, it should be possible to measure the lifetime of the dysprosium spin state as function of applied magnetic field, since a spin flip could be detected for instance as a sudden change in differential conductance when the tunneling voltage is fixed on one of the peaks. Measuring the magnetic field dependence of this lifetime might even offer some signatures of hyperfine transitions, which will be explained in more detail in the last section of this chapter.

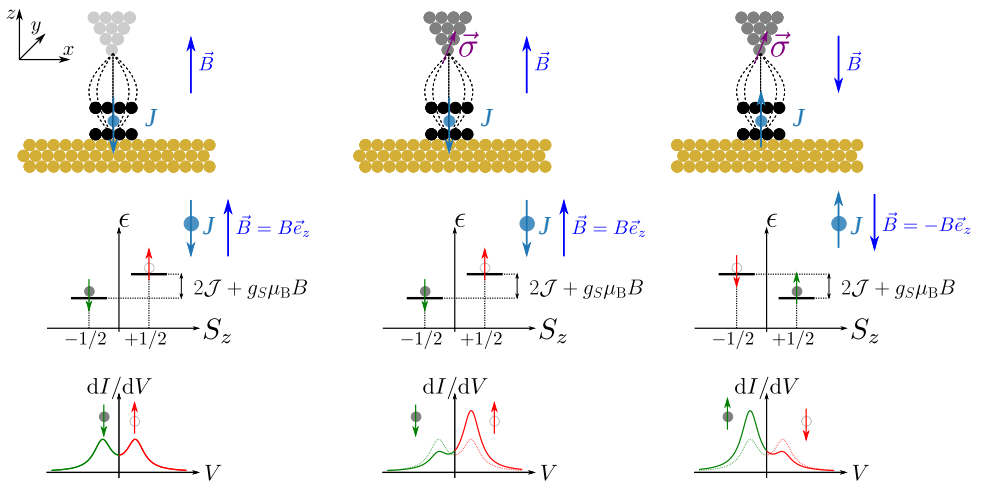

Figure 4.12: Scheme of how to read out the dysprosium spin. The spin polarization of the two peaks of the split Kondo resonance and the expected tunneling spectra for a spin-polarized tip are depicted.

Results of the spin-polarized measurements

The spin-polarized measurements presented in the following were acquired with an antiferromagnetic, chromium-coated tungsten tip at roughly 100 mK at the dilution STM. The tip thereby was prepared according to the procedure described in chapter 3.4. Compared to a ferromagnetic tip, such a probe offers the advantage, that there is no magnetic stray field, which may interfere with or alter the $DyPc_2$. Moreover, the tip spin-polarization is rather independent of the external magnetic field. The first successful spin-polarized measurements of this work on $DyPc_2$ were in fact performed with a ferromagnetic cobalt-coated tungsten tip. However, the interpretation of that set of data, which is presented in appendix 1, turned out to be very difficult and hence less conclusive.

First of all, figure 4.13a shows some exemplary tunneling spectra of the split Kondo resonance with spin contrast for various magnetic fields, acquired with the AFM tip on one molecule. As described schematically in figure 4.12, this results in an asymmetry of the peak heights, due to the TMR effect. Since the z-position of the STM tip was stabilized at the same positive bias voltage and tunneling current for all the spectra, slightly different shapes occur for positive and negative polarization. This peak asymmetry after all corresponds to the spin-polarization of the spin 1/2 on the phthalocyanine ligand. Because of the ferromagnetic exchange with the dysprosium spin J, this also reflects the polarization of the latter, provided that the applied field is weak ($\mu_B B \ll \mathcal{J}_{ex}$) and the temperature is low enough ($k_B T \ll \mathcal{J}_{ex}$). In the next step, figure 4.13b shows the extracted peak asymmetries for the investigated molecule as function of magnetic field. Thereby, every measured point corresponds to one spectrum measured at the respective magnetic field.

The asymmetry was determined by the following protocol: First, the conductance value at maximum (minimum) bias was substracted from every

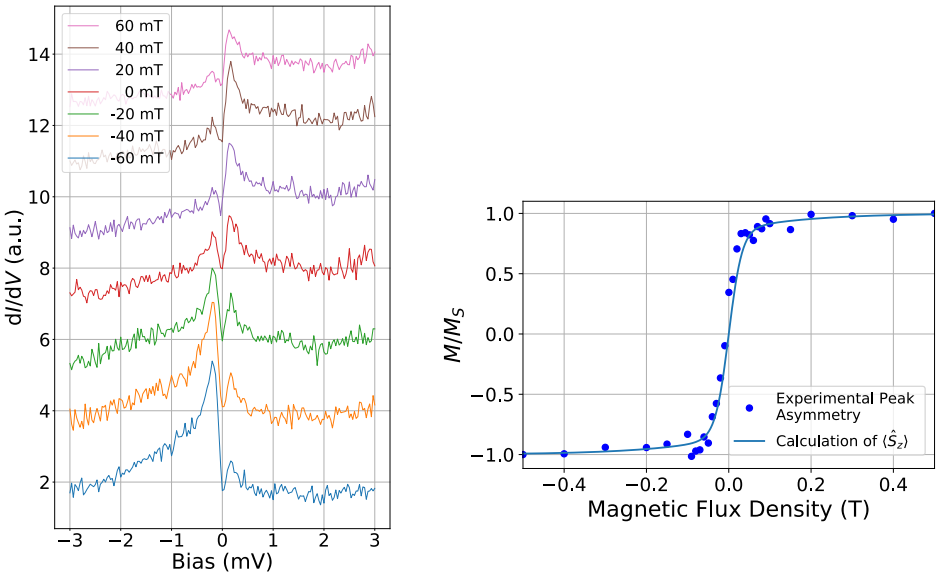

(a) **(b)**

Figure 4.13: Spin-polarized scanning tunneling spectroscopy on $DyPc_2$ as function of applied magnetic field. (a) Some exemplary spectra are shown. Lock-in parameters: 80 µV modulation at 2.32 kHz. (b) The extracted peak asymmetry is plotted as function of applied magnetic field (points). The solid line represents the calculated thermal expectation value $\langle \hat{S}_z \rangle$ with $\mathcal{J}_{ex} = (g_S/2)\mu_B \cdot 422\,\mathrm{mT}$, $g_S = 1.85$ and $T = 206\,\mathrm{mK}$ according to the fit in figure 4.11. The dysprosium g-factor was chosen to be $g_J = 4/3$.

spectrum at negative (positive) magnetic field as a constant offset. Then, the asymmetry A is given by

$$A = (B_1 - B_2)/(B_1 + B_2), \tag{4.5}$$

where $B_{1/2}$ are the highest value of peak one and peak two, respectively. The normalization of the asymmetry with respect to its saturation value, was chosen $\pm 0.5\,\mathrm{T}$ for positive and negative magnetic fields, respectively. It is apparent, that the spin polarization is already completely saturated at roughly 100 mT. The solid line in figure 4.13b, that simply corresponds to the calculated thermal expectation value $\langle \hat{S}_z \rangle$, is in good agreement with the

experimental data points. The calculation of $\langle \hat{S}_z \rangle$ was done in the framework of a very simplified model, that is described in the following.

Model calculation

In order to calculate the thermal expectation value of the polarization of the spin $\hat{S}$ on the Pc ligand, the eigenenergies of the $DyPc_2$ must be calculated first. The corresponding Hamiltonian - without the interaction to the gold substrate and omitting the hyperfine interaction - is given by

$$\hat{\mathcal{H}} \;=\; \hat{\mathcal{H}}_{\mathrm{CF}} \;+\; \mu_{\mathrm{B}} B \left(g_S \hat{S}_z + g_J \hat{J}_z \right) - \tilde{\mathcal{J}}_{\mathrm{ex}} \, \hat{\boldsymbol{S}} \cdot \hat{\boldsymbol{J}}. \tag{4.6}$$

The crystal field Hamiltonian in fourfold symmetry reads [15, 129]

$$\hat{\mathcal{H}}_{\mathrm{CF}} = B_2^0 \hat{O}_2^0 + B_4^0 \hat{O}_4^0 + B_6^0 \hat{O}_6^0 + B_4^4 \hat{O}_4^4 + B_6^4 \hat{O}_6^4. \tag{4.7}$$

As described before, the idealized D_{4d} symmetry of the molecules, which corresponds to a skewing angle of 45° between the two phthalocyanine ligands, would implicate $B_4^4 = B_6^4 = 0$. For this simplified scenario, the residual three crystal field parameters were determined in [129]. The result was, that J_z remains a good quantum number and the ground state doublet with $J_z = \pm 13/2$ is separated from the next highest states with $J_z = \pm 11/2$ by roughly 4.3 meV. Since all energy gaps between the ground state and the respective crystall field eigenstates are hence large compared to $\mu_{\mathrm{B}} B$ and $k_{\mathrm{B}} T$ at roughly 100 mK, the states other then $|\pm 13/2\rangle$ will hardly contribute to any thermal expectation value at such low fields and temperatures. Therefore, the following simplified model, takes the zero field splitting implicitly into account by restricting to the ground state doublet only.

Choosing the basis

$$\begin{aligned} |S_z, J_z\rangle = \{ &|+1/2, +13/2\rangle, |-1/2, +13/2\rangle, \\ &|+1/2, -13/2\rangle, |-1/2, -13/2\rangle \}, \end{aligned} \tag{4.8}$$

the resulting Hamiltonian reads

$$\hat{\mathcal{H}} \;=\; \mu_{\mathrm{B}} B \left(g_S \hat{S}_z + g_J \hat{J}_z \right) - \tilde{\mathcal{J}}_{\mathrm{ex}} \, \hat{S}_z \hat{J}_z, \tag{4.9}$$

such that both, S_z and J_z, remain good quantum numbers. The corresponding energies are

$$\epsilon = \left\{ \begin{array}{ll} \mu_B B\ (1/2\ g_S + 13/2\ g_J) - \mathcal{J}_{ex}, & \mu_B B\ (-1/2\ g_S + 13/2\ g_J) + \mathcal{J}_{ex}, \\ \mu_B B\ (1/2\ g_S - 13/2\ g_J) + \mathcal{J}_{ex}, & \mu_B B\ (-1/2\ g_S - 13/2\ g_J) - \mathcal{J}_{ex} \end{array} \right\} \tag{4.10}$$

with $\mathcal{J}_{ex} = 13/4\tilde{\mathcal{J}}_{ex}$. The corresponding Zeeman diagram is shown in figure 4.14a.

With this, it is straightforward to calculate the thermal expectation values in the next step. First of all, the partition function reads

$$Z = \sum_m \mathrm{e}^{-\beta\epsilon_m}. \tag{4.11}$$

The measured asymmetry of the split Kondo resonance corresponds to the expectation value $\langle \hat{S}_z \rangle$ of the unpaired spin 1/2. This is easily derived by using Maxwell-Boltzmann statistics. Finally, this yields the expression

$$\begin{aligned} \langle S_z \rangle &= \sum_m p_m s_z^m = 1/Z \sum_m \mathrm{e}^{-\beta\epsilon_m} S_z^m \\ &= 1/Z \left(+1/2\ \mathrm{e}^{-\beta\epsilon_1} - \ 1/2\mathrm{e}^{-\beta\epsilon_2} + 1/2\ \mathrm{e}^{-\beta\epsilon_3} - 1/2\ \mathrm{e}^{-\beta\epsilon_4} \right). \end{aligned} \tag{4.12}$$

This model function is the solid line plotted in figure 4.13b. For this plot, the parameters g_s, T and $J_{ex} = (g_S/2)\mu_B B_0$ were chosen according to the results from the fit in figure 4.11a.

Discussion

First of all, it seems that the experimental data of the investigated molecule are very well reproduced by the presented thermal model. The generally smooth course of the asymmetry even for small fields is nicely replicated. Additionally, it can be observed for single spectra, that both peaks become gradually more aligned as the magnetic field decreases. Even spectra, where the two peaks have the same height were observed. The fact, that this did not occur at precisely 0 T is arguably related to the remanence of the coil. The conclusion of this analysis would be, that the dysprosium moment

J of the investigated molecule is not stable, but switches back and forth between the two possible orientations. Otherwise a thermal population is not possible. In the process the switching rate appears to be faster than the typical timescale of one spectrum, that is of the order of several minutes.

In order to further illustrate this conclusion, figure 4.14a shows the corresponding Zeeman diagram of the simplified four state model for small external fields including the possible electronic transitions one can detect in STS. In the most simple case of a stable, non-fluctuating dysprosium moment only the transition $|-1/2,-13/2\rangle \leftrightarrow |+1/2,-13/2\rangle$ (transition **1**) occurs. This case would correspond to thermal fluctuations of the SOMO spin only, while the state of the dysprosium spin remained unchanged. Thus, the spin $1/2$ would mostly feel the constant exchange field of the dysprosium ion at small external fields. Conversely, in the above discussed model of a thermal population of all four states, however, additionally the transition $|+1/2,+13/2\rangle \leftrightarrow |-1/2,+13/2\rangle$ (transition **2**) must be possible. Accordingly, transitions between all four states occur, where also the dysprosium moment fluctuates.

In the next step, in order to verify, that the simplified analysis of the peak heights is justified, the differential conductance spectra were simulated using the perturbative model from reference [86] for these two limit cases. Subsequently, the asymmetry of the peak heights of these simulated spectra were determined analogous to the experimental asymmetries. The result of these simulations is shown in figure 4.14b together with experimental results and the corresponding model functions for the spin polarizations $\langle \hat{S}_z \rangle$ of the spin $1/2$.
The first case (blue dots) simulates the full spin system (without hyperfine interaction) consisting of the dysprosium angular momentum $J = 15/2$ with the ligand field parameters from [129] and a spin $1/2$, that is exchange coupled to J. In this simulation, the exchange field and all the model parameters were chosen according to the results of the fit from figure 4.11. It is apparent, that this case coincides fairly well with both, the presented model function $\langle \hat{S}_z \rangle$ from the last section (blue solid line) and the experiment (crosses). Conversely, the second case (violet dots) simulates the tunneling spectra for the limit where the dysprosium spin is stable at finite external

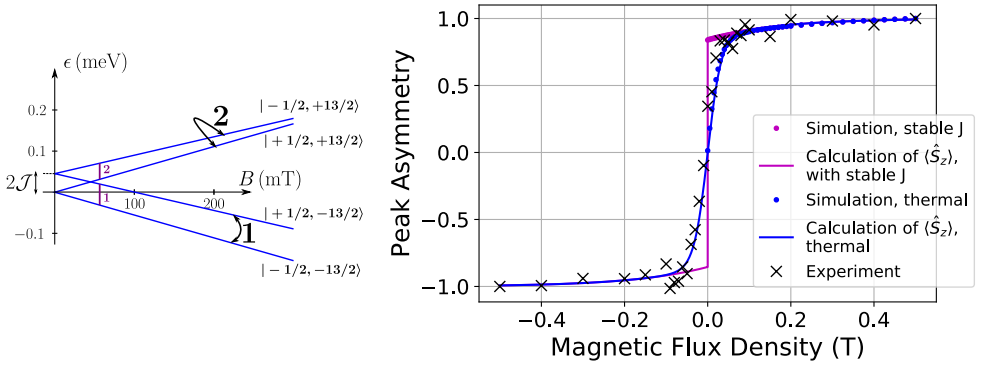

(a) **(b)**

Figure 4.14: Energy diagram of the ground state doublet of $DyPc_2$ and simulation of Kondo peak asymmetry. (a) The energy diagram as function of magnetic field is shown for the ground state doublet with $J_z = \pm 13/2$ and the SOMO spin $S_z = \pm 1/2$. (b) The asymmetry of the split Kondo peaks was simulated using the model from [86] for two limit cases: The thermal limit uses the full Hamiltonian containing a spin 1/2 exchange-coupled to the dysprosium spin J with the ligand field parameters from [129]. The second limit assumes, that the dysprosium spin is stable and simply adds an offset field to the spin 1/2 system.

fields and only switches at zero magnetic field. For this case, which is equivalent to the assumptions made for the analysis of section 4.3, the tunneling spectra of a spin 1/2 were simulated, using a constant offset in the z-component of the magnetic field, which represents the exchange interaction with J. Again, the model parameters were chosen according to the results from the fit in figure 4.11. The expectation for this limit is, that the peak asymmetry follows a shifted Brillouin function (violet solid line) of the shape

$$\langle \hat{S}_z \rangle_{\text{stable } J} = A \cdot \tanh\left(\frac{g_S \mu_B (B + B_0)}{2 k_B T}\right). \tag{4.13}$$

This is the exact result for the thermal expectation value of the SOMO spin polarization, when only the two states $|-1/2, -13/2\rangle$ and $|+1/2, -13/2\rangle$ are considered. Again the simulated peak asymmetry of the peak heights coincides fairly well with the expected model function. However, it seems that the first case of a thermal behavior of J fits better to the experimental data in the low field limit. Nevertheless, these simulations show, that the

extracted peak asymmetry indeed represents the spin polarization of the spin 1/2.

In conclusion, this analysis strongly suggests, that the dysprosium electronic angular momentum J is not stable near vanishing magnetic fields on the timescale of a single measurement, but that it switches back and forth. This raises the question whether a direct signature of such switching events should be observable in the experiments. First of all, one might expect that a tunneling spectrum would not only feature the two Kondo peaks corresponding to transition **1**, but that two additional peaks occur that represent transition **2**. The intensity of the additional peaks of transition **2** would scale with the thermal population of the states with $J_z = +13/2$, and their spin polarization would be opposite to the peaks of transition **1** for small fields. The two energy gaps, that are marked as violet bars in figure 4.14a for one exemplary field value, would correspond to the peak distances to zero bias. These energies are very similar for the two transitions at very small fields, though. As the magnetic field is increased the intensity of transition **2** decreases exponentially due to the thermal occupation, which is saturated at roughly 100 mT. This might be the reason, why the tunneling spectra only feature two identifiable peaks corresponding to transition **1**.
In the next step single switching events were supposed to be detected. Setting the bias voltage to one peak position of the split Kondo resonance at constant lateral tip position, a dysprosium switching event should be visible as a sudden change in tunneling conductance. If the feedback is turned on in the process, the tip should change back and forth between two discrete z positions corresponding to the two possible spin orientations $\pm 13/2$ of dysprosium. Such a random telegraph noise, however, was not observed at zero field, which corresponds to case where the two peaks are of the same height. This in turn would mean that the switching rate is faster than the typical acquisition rate of some kHz. Since the switching rate is expected to be fastest at zero field, this experiment was then performed while the magnetic field was slowly ramped ($\sim 5\,\mathrm{mT/s}$) around zero field. The tip position was controlled by the *atom tracker* module of the Nanonis system in the process. Still no telegraph noise was observed.

Altogether these measurements suggest, that the spin state of the inves-

tigated molecule was not stable on the time scale of the experiment. The cause is not directly apparent. One could argue that whole system consiting of dysprosium spin and SOMO, thus $13/2 \otimes 1/2$, exhibits an integer total spin, such that the Kramers degeneracy at zero magnetic field may be lifted. This in turn would enable QTM. Furthermore, it is not clear how the adsorption on Au(111) affects the symmetry of the molecule. Additionally, the investigated molecule was adsorbed on a step edge which can further reduce its symmetry and thus promote QTM. One important aspect, which has been neglected so far in this whole discussion, is the nuclear spin of dysprosium. Unfortunately, all experiments used $DyPc_2$ molecules with the natural abundance of dysprosium isotopes, such that the nuclear spin of the presented molecule is unknown. Further experiments using isotopically enriched samples might therefore provide more insights.

4.5 Conclusion and Outlook: Hyperfine Transitions

In conclusion, $DyPc_2$ molecules on Au(111) were investigated. A clear Kondo resonance can be observed on the top Pc ligand due to a single spin 1/2. At sufficiently high energy resolution the resonance is split due to a ferromagnetic exchange interaction between this unpaired spin and the dysprosium magnetic moment. Using spin-polarized spectroscopy, the asymmetry of the two peaks of the split resonance was measured as function of the external magnetic field for one molecule in order to track its dysprosium spin orientation. The results suggest a thermal behavior with a non-stable dysprosium spin on the time scale of the experiments.

However, the effects of the dysprosium nuclear spin need to be included in the debate. The thermal spin behavior might suggest a singlet nuclear spin for the investigated molecule. As argued above, the resulting $13/2 \otimes 1/2$ system would be a non-Kramers system. Perhaps the opposite case of a finite nuclear spin of $I = 5/2$, that results in a half-integer total spin via $13/2 \otimes 1/2 \otimes 5/2$, might result in more stable spin states. In case this holds true, the whole of the presented experiments offers intriguing perspectives for detecting signatures of the dysprosium nuclear spin in STM. For in-

stance it is expected, that the spin lifetime drops significantly every time the applied magnetic field value hits one of the forbidden crossing points of the two hyperfine multiplets. Accordingly, it seems conceivable to even distinguish different isotopes of dysprosium in STM. In order to get further insight, though, the next step should be to investigate samples that feature only one isotope of dysprosium.

5 3d Metal Acetylacetonates

A much more straightforward approach towards SMMs are 3d transition metal systems. Since the 3d electrons are less localized and even contribute to the coordinative bonds between the ligands and the central metal ion, they are usually readily accessible by STS. The drawback is, however, that the stability and coherence of the molecular spin states are expected to be smaller compared to the 4f systems, due to the rather strong coupling of the spin system to its environment. As described in chapter 2.4.1, the orbital angular momentum is quenched in 3d systems, such that their magnetic properties arise merely from the total electron spin S.
In this work, two different transition metal acetylacetonate compounds, namely $Co(acac)_3$ (*Cobalt-(III)-Acetylacetonate*) and $Cr(acac)_3$ (*Chromium-(III)-Acetylacetonate*), were investigated when adsorbed on a Cu(111) single crystal at the JT-STM at roughly 720 mK. This chapter is organized as follows: First, the structure and magnetic properties of the two compounds are discussed and a short review of previous investigations of the $Cr(acac)_3$ system is given. Then, the observations on the two compounds are presented. Finally, a simple model of how to understand these results is proposed.
It should be pointed out, though, that during this study, problems with the deposition temperatures of the molecular evaporator occurred. Here, only the results of those samples are presented, where a large number of equivalent objects could be observed on the sample surface in order to ensure, that these observed objects are indeed the deposited molecules or its derivatives and not just pollutions or fractured molecules.

5.1 The Molecule Properties

The trivalent transition metal acetylacetonates are chelate complexes, where the central metal ion is surrounded by six oxygen atoms in octahedral symmetry. While the metal ion is threefold positively charged, one negative charge is assigned to each of the acetylacetonate ligands. Figure 5.1 shows the molecule structure and the spin configurations in the gas phase. As elaborated in chapter 2.4.4, the 3d orbitals split into e_g and t_{2g} orbitals. Accordingly, $Cr(acac)_3$ is a $S = 3/2$ system [135], while the $Co(acac)_3$ was reported to be diamagnetic with $S = 0$ [136].
Using ESR measurements, the ZFS could be determined for crystalline $Cr(acac)_3$. The crystal field parameters of the model Hamiltonian

$$\mathcal{H} = g\mu_B \boldsymbol{B} \cdot \hat{\boldsymbol{S}} + D\left(\hat{S}_z^2 - 1/3\hat{\boldsymbol{S}}^2\right) + E\left(\hat{S}_x^2 - \hat{S}_y^2\right) \tag{5.1}$$

were determined to be $g = 1.983 \pm 0.002$, $|D| = (0.592 \pm 0.002)\,\mathrm{cm}^{-1}$ and $|E| = (0.052 \pm 0.002)\,\mathrm{cm}^{-1}$ assuming an isotropic g-factor [137]. Under the assumption of a positive value for D [135], the ground state doublet would consist mainly of the states with $S_z = \pm 1/2$. Hence, in STS one would expect a Kondo system with one inelastic excitation at $2D \approx 150\,\mu\mathrm{eV}$.
However, it seems very likely that the geometry of the molecules is distorted due to the molecule-substrate interactions, such that the crystal field parameters - and hence the magnetic properties - change drastically for adsorbed molecules. Additionally, it was reported, that $Cr(acac)_3$ can be sublimed without any molecular decomposition [138].
Conversely, for the cobalt system it was reported, that the molecules can decompose at temperatures of around 220 °C, such that divalent $Co(acac)_2$ is generated [139, 140]. This is not necessarily a problem, since for the sample preparation of this work only vapor pressures of the order of 1.0×10^{-8} mbar are needed, which may be achieved at way lower temperatures.

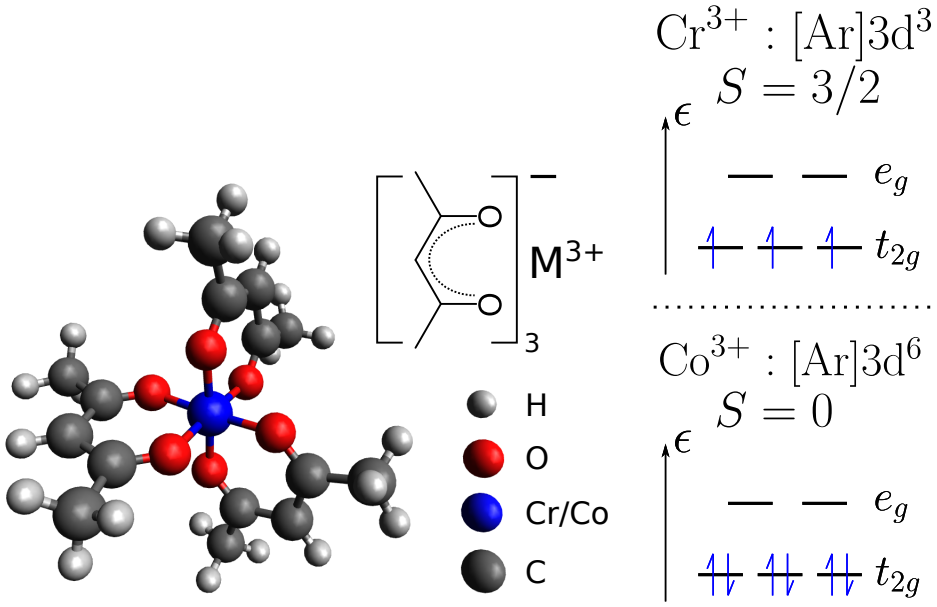

(a) Molecular structure **(b)** Electron configuration

Figure 5.1: Structure and electronic configuration of the trivalent acetylacetonates. (a) The molecule is a chelate complex, where the central transition metal ion (M = Cr,Co) is surrounded by 6 oxygen atoms in octahedral symmetry. (b) In the gas phase, Cr(acac)$_3$ is paramagnetic with a Spin 3/2, while the Co(acac)$_3$ is reported to be diamagnetic with $S = 0$.

5.2 Previous Results on Cr(acac)$_3$/Cu(111)

The Cr(acac)$_3$/Cu(111) system has already been investigated within the framework of the PhD theses of Lei Zhang [119] and Stefan Schmaus [141]. These previous measurements were performed at the 4K STM. Both were able to observe chains consisting of equal objects in the shape of dumbbells on their samples (figure 5.2). From this it was concluded, that the molecules are adsorbed such that they are standing on one of the acetylacetonate ligands. Additionally, a Kondo resonance could be measured in the center of these objects. This result is indeed well-expected for a twofold symmetric system with a half integer spin and is independent of the exact values of the crystal field parameters (chapter 2.4). The Kondo temperature was

determined to be roughly $T_K = (151 \pm 5)$ K [141] or $T_K = (34 \pm 2)$ K [119]. This enormous discrepancy is most likely related to a different experimental broadening due to different lock-in modulations. Farther, a coupling of the Kondo state to the surface state of the copper substrate was observed, such that a Kondo resonace could also be detected at distances corresponding to multiples of half the Fermi wavelength [141].

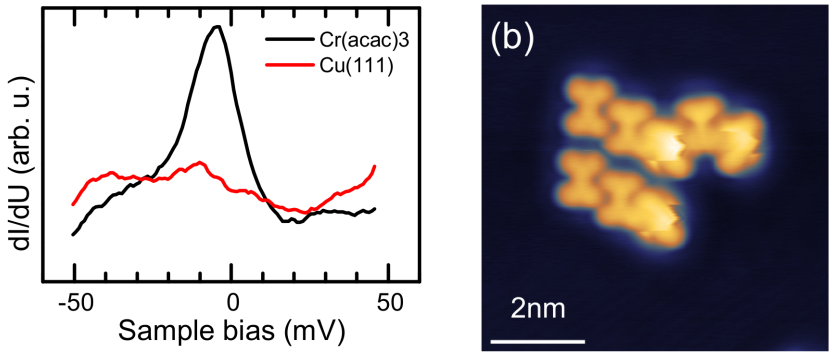

Figure 5.2: Previous results on the Cr(acac)$_3$/Cu(111) sytem. (a) In the center of the molecules a Kondo resonance occurs. (b) In topography, chains consisting of equal dumbbell-shaped objects can be observed. Both images are adopted from [119].

5.3 Results on Cr(acac)$_3$ and Co(acac)$_3$

In this work, a total of three reliable samples of Cr(acac)$_3$ on Cu(111) and one sample of Co(acac)$_3$ on Cu(111) are presented. The deposition temperatures for the presented samples are given in Table 1 in appendix 2.

5.3.1 Cr(acac)$_3$

On the samples of Cr(acac)$_3$ on Cu(111) two different species of objects could be observed. On two samples (sample 1 and 2) only threefold symmetric molecules consisting of three lobes in triangular shape were observed, while on one sample (sample 3) both, these triangles and additionally twofold

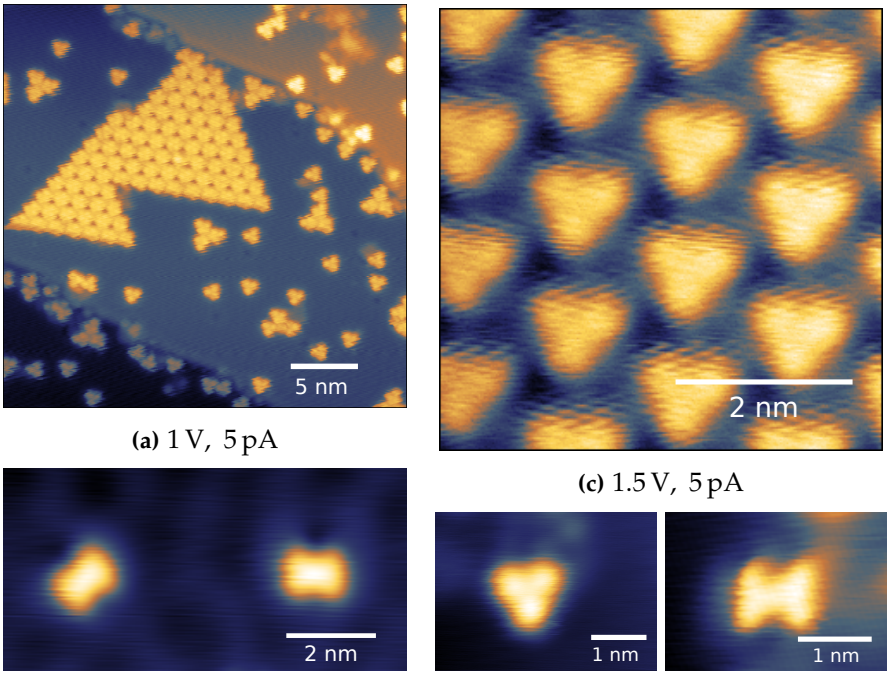

(a) 1 V, 5 pA **(c)** 1.5 V, 5 pA

(b) 40 mV, 1 nA **(d)** 1 V, 100 pA **(e)** 1 V, 100 pA

Figure 5.3: Topography scans of the triangular and dumbbell-shaped molecules observed on the $Cr(acac)_3$/Cu(111) samples. (a), (c) and (d) show the triangular molecules including their island structure. (b) and (e) show the dumbbell-shaped molecules, that presumably are analogue to the objects observed in [119, 141].

symmetric dumbbell-shaped objects occurred. Figure 5.3 shows some topography scans of these different observed geometries. While on sample 3 only isolated dumbbell molecules were found, for the triangles, even hexagonally ordered islands could be observed at sufficiently high coverage. The first notion might be, that every lobe corresponds to one individual acetylacetonate ligand and that the triangles and dumbbells represent $Cr(acac)_3$ and $Cr(acac)_2$, respectively. Clearly, this would require, that the molecules can decompose during the deposition procedure. Assigning one negative charge to each acetylacetonate ligand, this would result in different charge states and hence different total spins for the two objects.

Interestingly, in spectroscopy the two different objects show very different

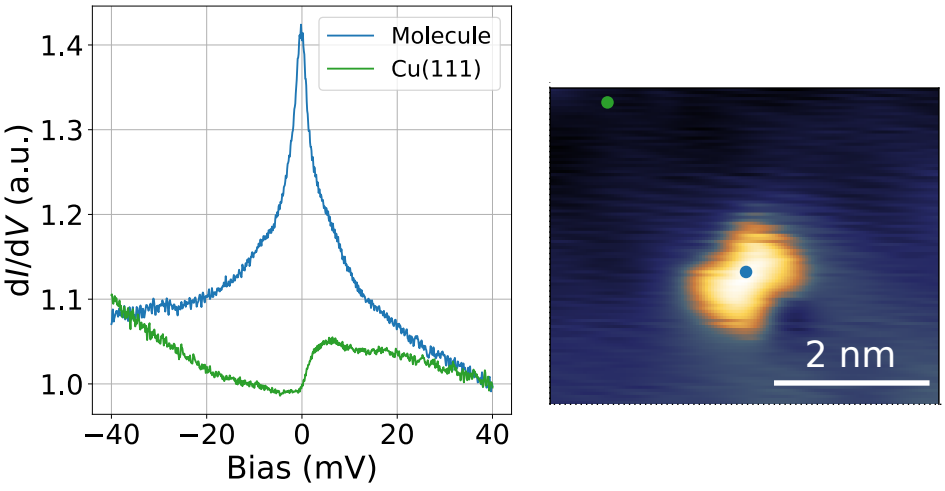

(a) STS on twofold objects **(b)** Respective locations

Figure 5.4: STS on the dumbbell-shaped objects of the Cr molecules. (a) A clear resonance occurs, including two shoulders. (b) The topography shows the tip locations during these spectra. Topography parameters: (40 mV, 13 nA). The spectra were measured at a lock-in modulation of 0.1 mV and a temperature of roughly 720 mK.

behavior. While no spectroscopic features - such as a Kondo resonance or inelastic excitations - could be observed on the triangular shaped objects, the dumbbells show a clear resonance with two shoulders, which might represent a Kondo resonance and one inelastic excitation. A typical spectrum obtained on the center of these dumbbells is shown in figure 5.4.
The observed resonance is very located in the molecular center, where the chromium ion is expected. This is illustrated by figures 5.5a and 5.5b, where the zero bias differential conductance is mapped. Moreover, this spectrum was fitted using the following model function

$$\frac{\mathrm{d}I}{\mathrm{d}V}(\epsilon) = c + m\cdot\epsilon + A_K\cdot f(\epsilon, q, \Gamma_\mathrm{F}) + A_S\cdot\left(\Theta\left(\epsilon_\mathrm{ex}+\epsilon, T\right) + \Theta\left(\epsilon_\mathrm{ex}-\epsilon, T\right)\right), \tag{5.2}$$

that contains a linear background, a Fano-Frota function $f(\epsilon, q, \Gamma_\mathrm{F})$ and two thermally broadend step functions $\Theta(\epsilon_\mathrm{ex} \mp \epsilon, T)$ with

$$\Theta(\epsilon) = \frac{1+(x-1)\exp(x)}{(\exp(x)-1)^2} \quad \text{and} \quad x = \epsilon/(k_\mathrm{B}T) \tag{5.3}$$

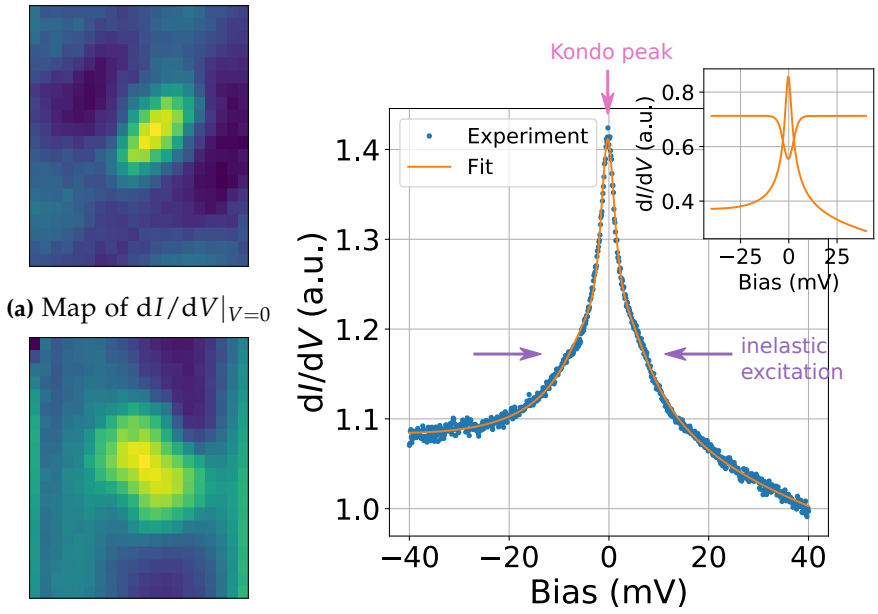

(a) Map of $\mathrm{d}I/\mathrm{d}V|_{V=0}$

(b) Topography

(c) Fano-Frota Fit

Figure 5.5: Localization of the Kondo resonance and Fano-Frota fit. The differential conductance at zero bias is mapped in (a). The corresponding topography after a drift correction is shown in (b) (3 nm × 3 nm). The result of the fit shown in (c). The parameters are $\Gamma_\mathrm{F} = (1.69 \pm 0.02)$ meV, $q = 60.6 \pm 4.7$, $\epsilon_\mathrm{ex} = (0.76 \pm 0.03)$ meV and $T = (13.0 \pm 0.2)$ K. The inset shows the resonance with linear offest and the inelastic steps separately.

to account for the inelastic excitation [134]. The result is shown in figure 5.5c. The fit gives an estimated Kondo temperature of

$$T_\mathrm{K} = (12.7 \pm 0.2)\,\mathrm{K} \tag{5.4}$$

and excitation energy of

$$\epsilon_\mathrm{ex} = (0.76 \pm 0.03)\,\mathrm{meV}. \tag{5.5}$$

Interestingly, the apparent effective temperature of the system - given by the broadening of the step functions - is estimated to be $T = (13.0 \pm 0.2)$ K, which is more than one order of magnitude higher than the actual sample temperature. Moreover, this is almost the same value as the Kondo temperature. This together with the fact that the excitation occurs inside the Kondo

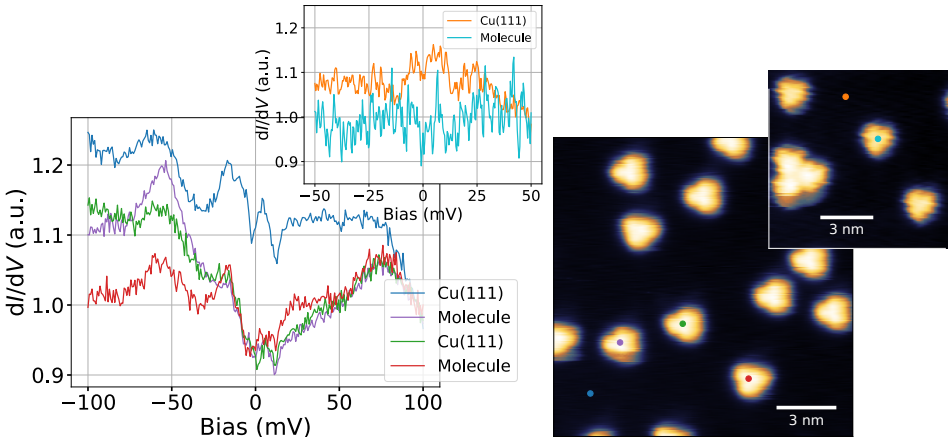

Figure 5.6: STS on the triangular shaped Cr molecules. (a) These molecules do not show any spectroscopic feature, such as a Kondo resonance or inelastic excitations. The inset shows a smaller energy range, measured with different tip conditions. (b) The topography scans show the tip locations during these spectra. Topography parameters: $(1\,\mathrm{V},\ 50\,\mathrm{pA})$. All spectra were measured at a lock-in modulation of 1 mV.

resonance itself might indicate, that this is not thermal broadening at all, but that this is rather lifetime broadening caused by the Kondo scattering.

In contrary, on the triangle molecules no spectroscopic features, such as a Kondo effect or an inelastic excitation, were observed. Figure 5.6 shows several exemplary spectra acquired on these triangular objects, including the respective tip locations. Even at lower lock-in modulations ($\lesssim 0.25\,\mathrm{mV}$) no molecular excitation could be observed even when measuring the second derivative of the tunneling current.

The comparison of the results obtained on these two different species of molecules illustrates, how the geometry and number of ligands can affect the magnetic properties of the chromium spin system: In twofold symmetry, a Kondo effect is expected for half integer spins. Therefore, assuming the dumbbells represent $Cr(acac)_2$, a charge transfer of one electron to the copper substrate is required to end up with a total spin of $S = 3/2$ in order to account for the Kondo resonance and the inelastic excitation. Conversely,

in threefold symmetry one can end up either with a stable spin or a singlet ground state depending on the ligand field parameters, such that no Kondo effect occurs for the triangles. A more detailed discussion will follow in section 5.4. Furthermore, in appendix 2 additional measurements - including the magnetic field dependence of the Kondo resonance, an attempt to fit the Kondo resonance with perturbation theory and an alternative island structure of the triangles - are presented.

5.3.2 $Co(acac)_3$

On the samples of $Co(acac)_3$ on Cu(111) only one type of objects could be observed. These objects again exhibit twofold symmetry and consist of two lobes, similar to the dumbbell molecules observed on one of the chromium samples. Figure 5.7 shows some topography scans of these molecules. Threefold symmetric triangles, like those observed on the $Cr(acac)_3$ samples, could not be observed on any of the $Co(acac)_3$ samples. The assumption, that again these dumbbell objects represent the divalent $Co(acac)_2$, seems compatible with previous reports, where the $Co(acac)_3$ decomposition was observed upon sublimation [139, 140]. Note however, that the molecular deposition for this sample was performed at lower temperatures.

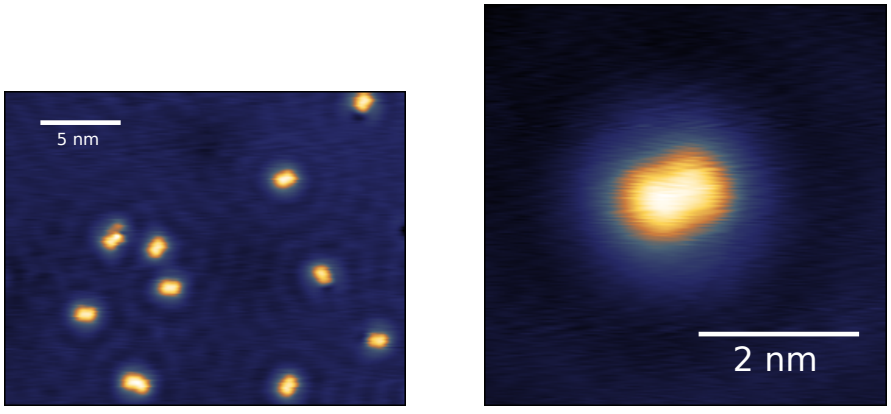

Figure 5.7: Topography of the dumbbell-shaped objects observed on the $Co(acac)_3$/Cu(111) sample. Topography parameters: (0.1 V, 1 nA).

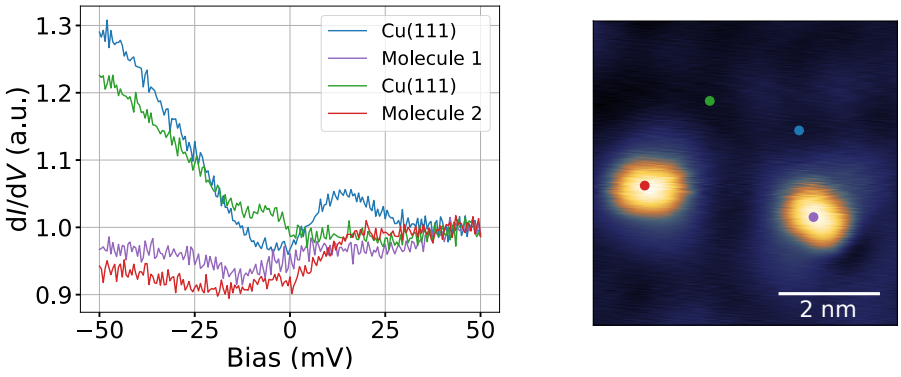

(a) STS spectra

(b) Locations of the spectra

Figure 5.8: STS on the dumbbell-shaped objects of the Co molecules. The topography in (b) shows the tip locations during the spectra of (a). Topography parameters: (50 mV, 1 nA). The spectra were measured at a lock-in modulation of 0.5 mV.

In STS no spectroscopic features, such as a Kondo signature or inelastic excitations, could be observed. Figure 5.8 illustrates some exemplary spectra. These observations appear to be consistent with the previous conclusions drawn for the chromium system: Assuming the same charge transfer from the molecule to the copper substrate as it was done before for the chromium dumbbells, yields an integer spin ($S = 0, 1, 2$) for the resulting Co^{3+} (with $[Ar]3d^6$). Since a singlet ground state is expected for an integer spin in twofold symmetry, no Kondo resonance can be observed. Additionally, the absence of any inelastic excitation is consistent with $S = 0$, though, a more elaborate discussion will follow in the upcoming section 5.4.

5.4 Summary and Conclusion

The scheme in figure 5.9 gives an overview of the observations and what conclusions can be drawn. First of all, the observed shape in topography was related to a certain number of acetylacetonate ligands, and hence a certain charge state of the central ion. The dumbbell shape corresponds to a divalent ion with two ligands, while the triangle corresponds to a trivalent ion with three ligands. Since a Kondo effect in twofold symmetry is expected

for half-integer spins, in the next step, a charge transfer from the dumbbell molecules to the copper substrate is demanded. In case of the chromium molecule this results in a $S = 3/2$ system, that consists of two subsets of states enabling Kondo scattering (see chapter 2.4). Regardless of the precise values of the crystal field parameters, the expected result is a Kondo system with one inelastic excitation, both of which was observed. Conversely, in the case of the cobalt molecules, this charge transfer yields an integer total spin, which in twofold symmetry results in a non-magnetic singlet ground state such that no Kondo effect occurs. As no inelastic excitations were observed either, the measurements are consistent with the singlet $S = 0$. Nevertheless, it may also be possible, that the excitations which would be expected for the cases $S = 1, 2$ were just not observed due to insufficient energy resolution. Last, for the triangular shaped chromium molecules it is not clear right away whether or not the charge transfer occurs in the same way. In case it does, depending on the ligand field parameters, there are two possibilities for the resulting spin $S = 1$ system: $B_2^0 > 0$ yields a singlet ground state, while $B_2^0 < 0$ results in a stable ground state doublet $|\pm 1\rangle$. In both cases though, no Kondo resonance but one inelastic excitation can be expected. Conversely, in case the charge transfer does not occur, again two different cases can arise for the resulting $S = 3/2$ system. This time, though, $B_2^0 > 0$ results in a Kondo system, while $B_2^0 < 0$ again gives a stable ground state doublet $|\pm 3/2\rangle$ with one inelastic excitation expected. The fact that the expected inelastic excitation was not observed might be due to insufficient energy resolution.

In conclusion, most of the observations - except for the missing excitation - can be broken down and understood in this rather simple framework. Trivially, the twofold symmetric dumbbells as either a Kondo system or a non-magnetic singlet are not suited for the application as SMM. Further, whether or not the triangular chromium objects are suitable candidates crucially depends on the sign and magnitude of the crystal field parameter B_2^0. Accordingly, further investigations are needed to draw conclusion on their suitability as SMM.

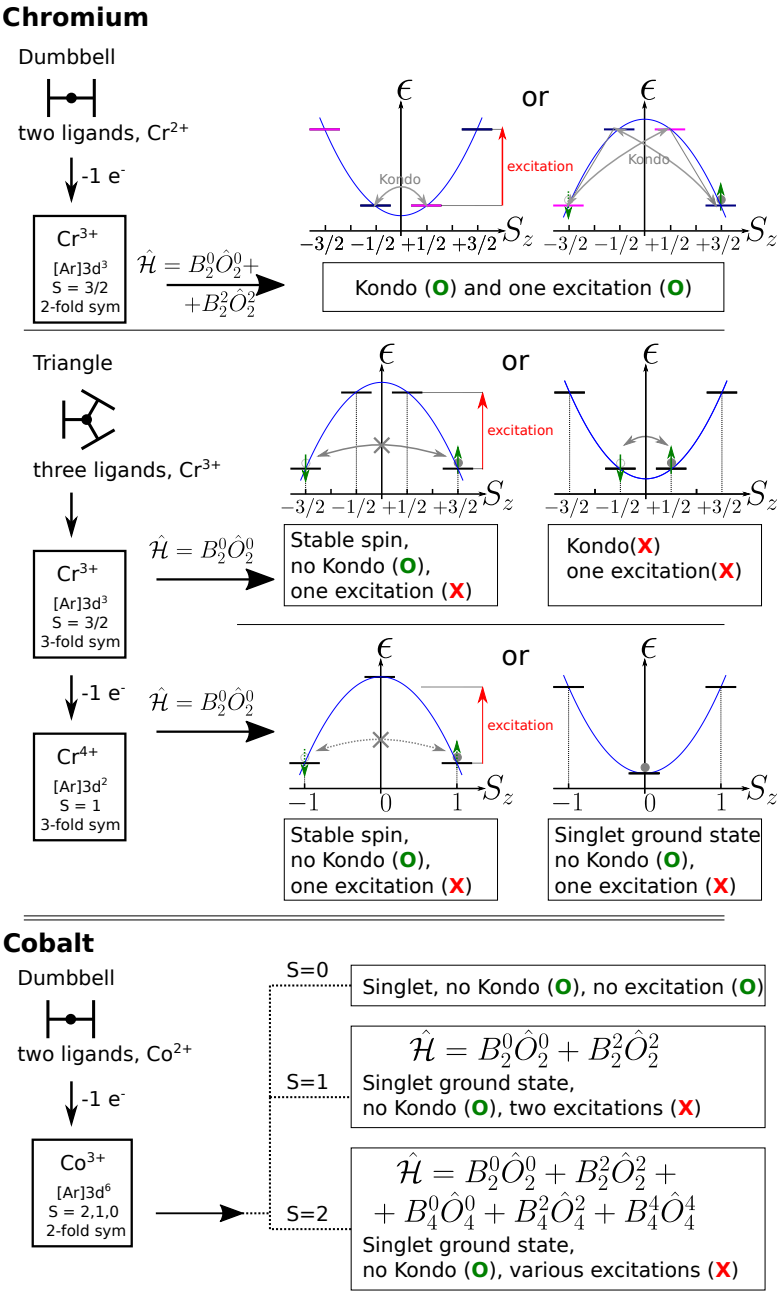

Figure 5.9: Overview of the results and conclusions for the M(acac)$_3$/Cu(111) systems. For every shape and spin state, the effective spin Hamiltonian, the corresponding spin spectrum and the expected spectroscopic features are given. A O or a X indicates, whether or not the respective feature was observed.

6 Spin Crossover Molecules on Ferromagnetic Substrates

Spin crossover (SCO) molecules are metal-organic compounds, that stand out by a thermal phase transition from a non-magnetic ground state with spin $S = 0$ to a paramagnetic state with $S = 2$. The objective of this project was to investigate SCO molecules on ferromagnetic thin films regarding two aspects: Whether or not the adsorbed molecules maintain their ability to switch between the two spin states, and whether they exhibit any magnetic exchange interaction with the substrate. In case both holds true, such a material system would make up an excellent candidate for multifunctional spintronic application, since the spin crossover can be triggered by various other external stimuli. This chapter will be structured in the following way: First of all, a short motivation of the project, including some crucial previous reports on SCO molecules will be given. Then, two different investigated material systems will be presented. This firstly includes Fe(1,10-phenanthroline)$_2$(NCS)$_2$ molecules (short Fe-Phen) on a monolayer of iron nitride ($Fe_2N/Cu(100)$ investigated with low temperature STM. Secondly, $Fe\{[Me_2Pyrz]_3BH\}_2$ molecules (short Fe-Pyrz) on thin films of lanthanum strontium manganate ($La_{1-x}Sr_xMnO_3$, short LSMO) on a niobium-doped strontium titanate substrate ($SrTiO_3$, short STO) were investigated using MOKE, XAS and XMCD. For both systems a short review of previous results and previously published reports will be given.

6.1 Motivation and Project Idea

General properties of SCO molecules have already been discussed elaborately in chapter 2.4.4. Generally, SCO compounds are presumed to be

promising prospects for multifunctional spintronic application because of the versatility of the spin transition. This project aims to investigate SCO molecules adsorbed on ferromagnetic substrates. Given that both, the adsorbed molecules preserved their ability to switch between HS and LS state and that additionally a magnetic exchange between the HS molecules and the substrate occurs, such a material system makes up an interesting prospect for spintronic application, since the magnetic interaction to the substrate can be switched on and off via the SCO. For instance, one could envision to control and to switch the magnetic properties by initiating the SCO using any of the previously described triggers, such as pressure or temperature change, light illumination or electromagnetic fields. Therein, additionally the magneto-elastic coupling would be exploited, since the molecular geometry is slightly deformed upon the SCO. The effective magnetic moment and even anisotropy constants are among those properties that might change upon the SCO. This project idea is schematically illustrated in figure 6.1. Another conceivable application might be even writing magnetic structures using light illumination, exploiting the LIESST effect.

The most challenging issue for realizing such a material system is the electronic coupling between the molecules and the substrate. It was reported, that some SCO molecules may lose their ability to switch between HS and LS state when being adsorbed on metal substrates [142, 143, 144]. In this case the molecules are pinned to one spin state, such that transitions are not possible anymore. This may also lead to a coexistence of HS and LS molecules where the spin state seems to be determined by the very rigid adsorption geometry.
Further it was reported that the switching ability might be retrieved by sufficiently decoupling the molecules from the metallic substrate. For instance, it was reported that for Fe-Phen SCO molecules adsorbed on Cu(100) both spin states exist, though, that switching between HS and LS state is not possible. However, by inserting an insulating monolayer of Cu_2N the switching ability can be restored [103, 144]. In other works it was observed, that the first monolayer of molecules can have an analogue decoupling effect, such that the spin state pinning might be lifted in the second molecular layer already [142, 143]. Therefore, for this project it is crucial to control the interaction between the substrate and the molecules in order to preserve

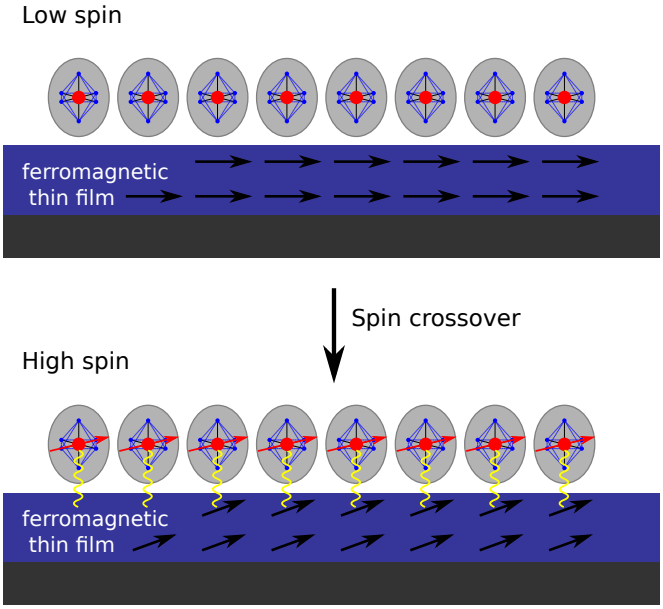

Figure 6.1: Project idea of SCO molecules on a ferromagnet. Upon triggering the SCO from LS to HS an exchange interaction between the HS molecules and the substrate occurs which might alter the sytem's magnetic properties. The magnetic properties of such a system could be controlled by whatever stimulus that triggers the SCO.

the spin transition.

Unfortunately, metallic and itinerant ferromagnets are usually particularly reactive, such that the electronic coupling to adsorbed molecules is expected to be strong. For instance, Gueddida and co-workers investigated the aforementioned Fe-Phen molecules on two monolayers of cobalt on Cu(111) [145]. By comparing the spectra obtained from sp-STS with theory calculations, they were able to identify HS molecules adsorbed on cobalt islands. Moreover, they reported that these molecules are indeed ferromagnetically exchange coupled to the cobalt substrate. The strength of this exchange between the iron ion of the molecules and the cobalt islands was calculated to be 22.6 meV. However, no spin state switching was possible for these molecules. In addition, presumably single phenanthroline molecules and another type of objects were observed on the cobalt. This might suggest that the Fe-Phen molecules can even decompose when they make contact

with cobalt.
Altogether these reports illustrate, that only inherently inert or passivated ferromagnets should be used as substrates for this project. In this work, LSMO thin films on STO as former, and one monolayer of $Fe_2N/Cu(100)$ as latter were investigated. Both choices shall be presented and motivated in more detail in the respective section.

6.2 Fe-Phen on $Fe_2N/Cu(100)$

The Fe-Phen molecules chosen for this project exhibit a thermal spin transition at 175 K [146, 147]. These molecules, whose structure is shown in figure 6.2a, were part of intensive studies on the electronic coupling of SCO molecules to metallic substrates. These previous reports on Fe-Phen, that were shortly mentioned in the last section already, are summarized in figure 6.3: When these molecules were adsorbed on Cu(100), they lost their ability to switch their spin state. Figure 6.4 shows some topography measurements for such an Fe-Phen/Cu(100) sample, which was reproduced for this work. The molecules appear as two symmetric lobes that correspond to the two phenanthroline groups. Interestingly, two different species of molecules occur, that differ in the distance of the two lobes. The molecules with larger inter-lobe distance show a Kondo resonance located in the center, such that they correspond to HS molecules [103, 144]. The smaller molecules do not show any resonance and correspond to LS molecules accordingly. This coexistence of HS and LS was additionally proved by XAS. In the next step, the switching ability of the molecules could be retrieved by inserting an insulating monolayer of Cu_2N [103, 144]. Hence, for the SCO to be possible it is necessary to passivate the substrate. On the other hand, the substrate needs to be ferromagnetic in order to exhibit a magnetic exchange interaction with the molecules, as it was observed in the case of Fe-Phen on Co/Cu(111) [144, 145].

Therefore, one promising substrate to unite both properties seems to be one monolayer of iron nitride (Fe_2N) on Cu(100) [148], whose structure is shown in figure 6.2b. It was reported, that one monolayer is already ferromagnetic

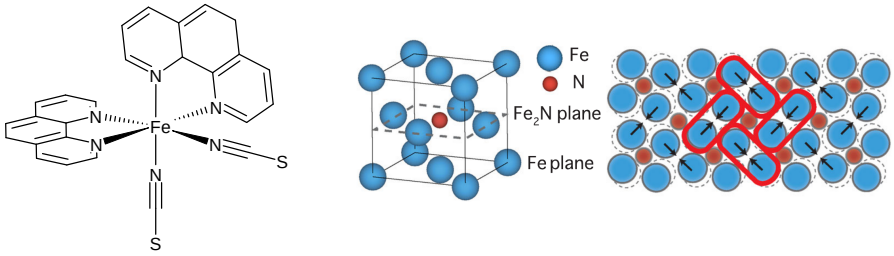

(a) Fe-Phen structure **(b)** Structure of Fe_2N/Cu(100)

Figure 6.2: Structures of Fe-Phen SCO molecules and Fe_2N/Cu(100). (a) The divalent iron ion is surrounded by six nitrogen atoms in octahedral symmetry. (b) The reconstruction of a monolayer of Fe_2N consists of iron dimers (right). This image is adopted from [148]. Reuse was permitted by T. Miyamachi.

with an in-plane easy axis and a spin magnetic moment of 1.1 μ_B [124]. Moreover, the structure and composition of Fe_2N resembles the analogue Cu_2N, such that there are good chances that this layer is still relatively inert in spite of its iron content. One characteristic feature of Fe_2N is its surface reconstruction, that includes the formation of iron dimers (as shown in 6.2b) [124, 148]. Interestingly, this reconstruction seems to have a magnetic origin: It was reported that thick film samples of γ'-Fe_4N on Cu(100) (roughly 200 monolayers) terminate with an Fe_2N layer, that exhibits the same surface reconstruction. For this system it was theoretically predicted that for the Fe pairing to occur in the terminating layer, it needs to be both, ferromagnetic as well as electronically decoupled from the bulk crystal [149]. Assuming both of this was transferable to a monolayer, the Fe_2N/Cu(100) would make up a promising prospect for this project.

Previous Works

For this system, some preliminary results were already reported in Jinjie Chen's PhD thesis [150]. On one sample, certain molecules were observed, that in topography resembled the Fe-Phen molecules on Cu(100). Additionally, on these molecules a reversible and robust switching between two states - analogue to the observations on Fe-Phen molecules on Cu_2N/Cu(100) - could be observed. It was concluded, that Fe-Phen adsorbed on Fe_2N indeed

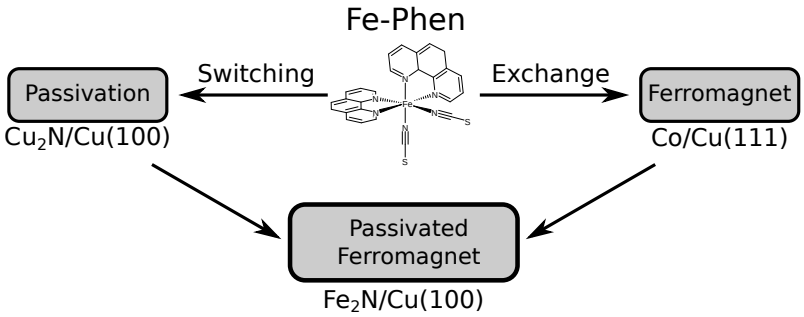

Figure 6.3: Summary on previous reports on Fe-Phen. The motivation for Fe-Phen on $Fe_2N/Cu(100)$ results from previous reports on Fe-Phen molecules: In order to preserve the spin state swichting, the molecules need to be decoupled sufficiently from the substrate, e.g. by one Monolayer of Cu_2N [103]. Moreover, an exchange interaction to a ferromagnetic substrate of Co/Cu(111) was detected [145]. $Fe_2N/Cu(100)$ seems to be a promising candidate to unite both prerequisites.

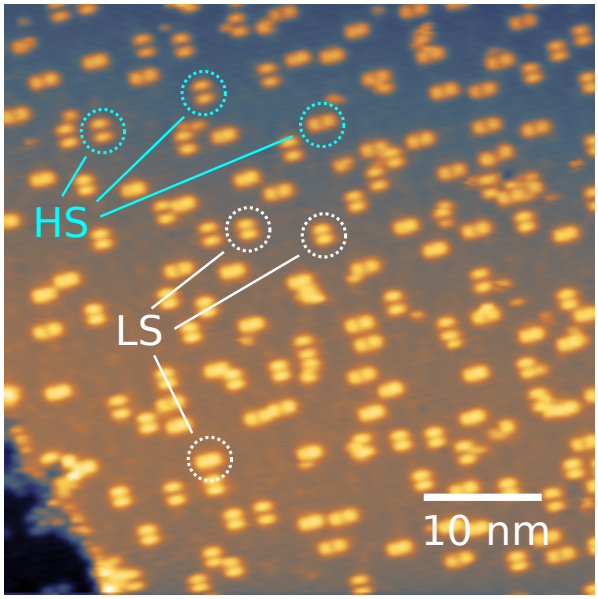

Figure 6.4: Topography of Fe-Phen on Cu(100). The molecules with larger (shorter) inter-lobe distance correspond to HS (LS) Fe-Phen. Topography parameters: $(1\,\mathrm{V},\ 50\,\mathrm{pA})$.

shows the desired behavior. However, since this was observed only on one sample, this system was supposed to be investigated more elaborately in this work.
Surprisingly, though, these previous, very promising results could not be confirmed in this work. Actually, an utterly different behavior was observed. This issue can only be explained in the way that actually different systems were measured. Hence, in one of the works, a severe problem must have occurred either during the growth of the monolayer of iron nitride, or during the molecular deposition. Therefore, special emphasis will be placed on the quality of the presented sample while presenting the results in the following section. Additionally, a more elaborate discussion of this contradiction, and a possible explanation for the occurrence of the previous results are presented in appendix 3.1.
The upcoming results were measured with the JT STM at roughly 5 K.

6.2.1 Results

To begin with, figure 6.5a shows an overview scan of the sample. It is apparent that the sample is very homogeneous and contains a large number of equal adsorbates. The fact that most of the adsorbates are equal indicates, that they are indeed the evaporated molecules and not just impurities from the gas phase. In order to ensure that the molecular deposition had indeed worked reliably without the Fe-Phen powder being decomposed during the sublimation process, a control sample of Fe-Phen on Cu(100) was grown after finishing the presented experiments. Thereby, the same deposition temperature was used, while the crucible was not exchanged but only degassed again. This sample did mainly show a high density of Fe-Phen molecules, but hardly any impurities. The topography shown in figure 6.4 actually shows this control sample.
Furthermore, figure 6.5b shows a scan of the Fe_2N substrate with atomic resolution. Clearly, the characteristic reconstruction including iron dimers is visible (see figure 6.2b). Together with the observation, that this sample is very homogeneous, this indicates that also the iron nitride growth worked satisfactorily.

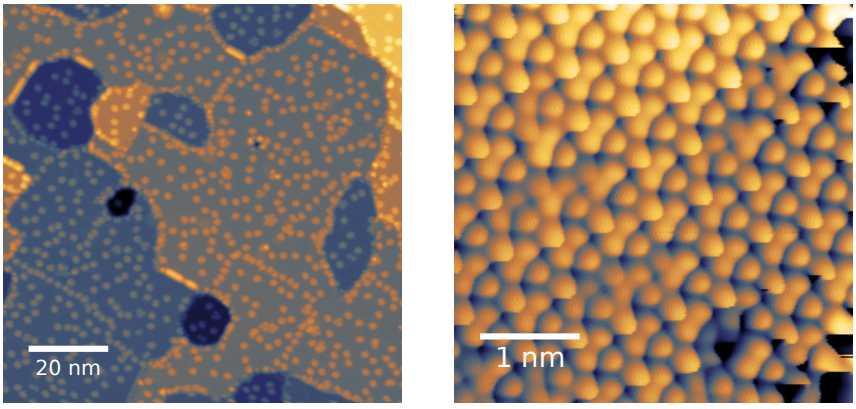

(a) 1 V, 50 pA **(b)** 0.1 V, 100 pA

Figure 6.5: Overview scan of the Fe-Phen on Fe_2N/Cu(100) sample and atomic resolution of the Fe_2N reconstruction. (a) The sample is very homogenous and clean. The large number of equal adsorbates indicates, that these are indeed the Fe-Phen molecules. (b) Scan with atomic resolution of Fe_2N. The atomic reconstruction is visible.

Figure 6.6 is a close-up scan including all the occurring adsorbates. The molecules of type A and B resemble the familiar shape of Fe-Phen consisting of two lobes. In analogy to the observations on Cu(100), the first notion might be, that molecules of type A with the larger inter-lobe distance correspond to HS Fe-Phen, while type B molecules are LS. Meanwhile type C appears to be simply an aggregation of impurities or molecule fragments. By far the largest fraction of adsorbates were type B molecules, while type A and type C could only be observed rarely. On a subsequent control sample of Fe-Phen on Fe_2N exclusively type B molecules were observed. No transition from type A to B (or vice versa) could be observed.
Interestingly, the shape of type B molecules strongly depends on the tunneling voltage. While the molecules appear symmetric at negative bias (figure 6.6c), they show a chiral structure at positive bias (figure 6.6c). Indeed, the Fe-Phen molecules are chiral, provided that they are anchored to the surface by both of their thiocyanate groups. Further, these molecules adsorb preferably along four directions. These directions consist of two directions, that are perpendicular to each other, and their mirrored counterparts with respect to the Fe_2N mirror axes. Conversely, the molecules of type B adsorbed preferably along the Fe_2N mirror axes.

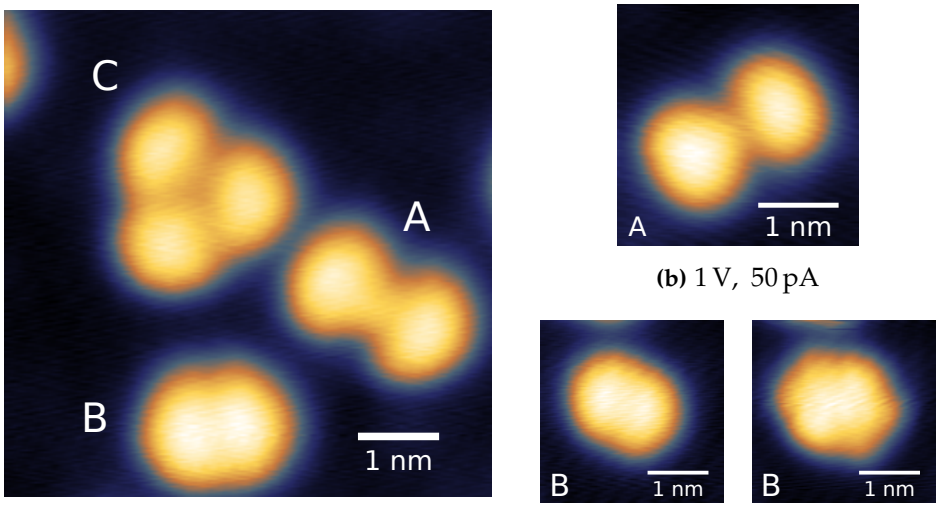

(a) $-1\,\mathrm{V},\ 50\,\mathrm{pA}$ **(b)** $1\,\mathrm{V},\ 50\,\mathrm{pA}$ **(c)** $-1\,\mathrm{V},\ 50\,\mathrm{pA}$ **(d)** $1\,\mathrm{V},\ 50\,\mathrm{pA}$

Figure 6.6: Topography of different types of molecules on Fe-Phen/Fe_2N. In (a) a scan with all three types is shown. (b) shows the shape of type A molecules, which is independent of the tunneling voltage. (c) and (d) show the type B molecules, where the shape varies with bias. Moreover, these molecules appear chiral at positive bias.

In the first step it was supposed to be tested, whether a robust switching between two states can be induced, in analogy to Fe-Phen molecules on Cu_2N. For this, the tunneling voltage was swept while the STM tip was placed atop a molecule's center, which is supposably the location of the central iron ion. During this bias sweep, the tunneling current was recorded. In case a molecular switching is triggered by a change in tunneling voltage or current, this can be observed as a sudden jump in the tunneling current. Assuming the two states are robust, this results in a hysteresis curve when the backward sweep is included (compare Fe-Phen on Cu_2N [103]). This experiment is shown in figure 6.7 for both, type A and type B molecules and various tip heights. It is apparent that no sudden changes in the tunneling current occurred, such that forward and backward sweep result in the same I-V spectrum. Hence, no molecular switching could be observed.

Figure 6.8 additionally shows some differential conductance spectra for the two types of molecules. No Kondo resonance could be observed. However,

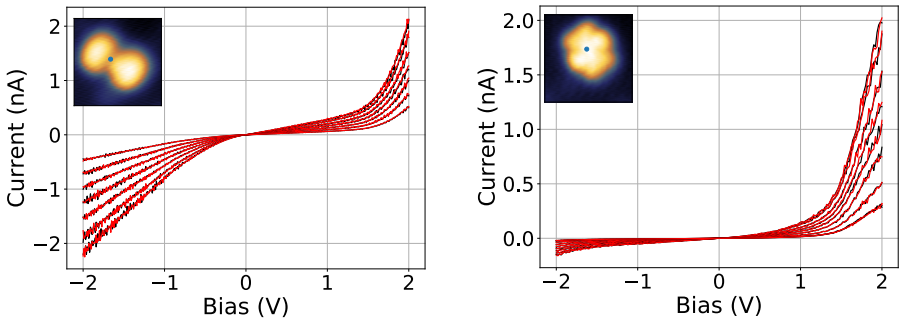

(a) Molecule type A **(b)** Molecule type B

Figure 6.7: Scanning tunneling spectroscopy on Fe-Phen on Fe_2N. I-V-curves are shown for type A molecules (a) and type B molecules (b). The black and red curves correspond to forward and backward sweep of the tunneling voltage, respectively. The different plots correspond to different tip-sample distances. No switching can be observed for either molecule type. The insets show the respective topography and the lateral tip position during the spectra. Topography parameters: $(3\,\mathrm{nm} \times 3\,\mathrm{nm},\ 1\,\mathrm{V},\ 50\,\mathrm{pA})$.

this measurement is not too compelling considering the poor energy resolution given the high temperature and the too high lock-in modulation. In general, for a LS molecule no Kondo effect can occur. For HS molecules no Kondo effect would mean the molecules are either exchange-coupled to the Fe_2N or that they are simply sufficiently decoupled from the copper substrate.

Interestingly, a different kind of switching behavior of type B molecules could be observed. When the STM tip is located atop such a molecule outside its center, a bistability, i.e. random switching between two metastable states, can be observed at high positive bias ($\sim 1.5\,\mathrm{V}$) and sufficiently high tunneling currents. This kind of back and forth switching is usually referred to as random telegraph noise (RTN). This behavior is shown in figure 6.9b. The two states correspond to different current values, while a switching event is visible as a sudden change in current. Additionally, topography scans of both states and the location where the RTN was recorded are shown in figure 6.9a: Since this switching only occurs at high bias, one can stop it at any given time. Thus, it is possible to determine in which of the two states the molecule will end up and both states can be scanned independently.

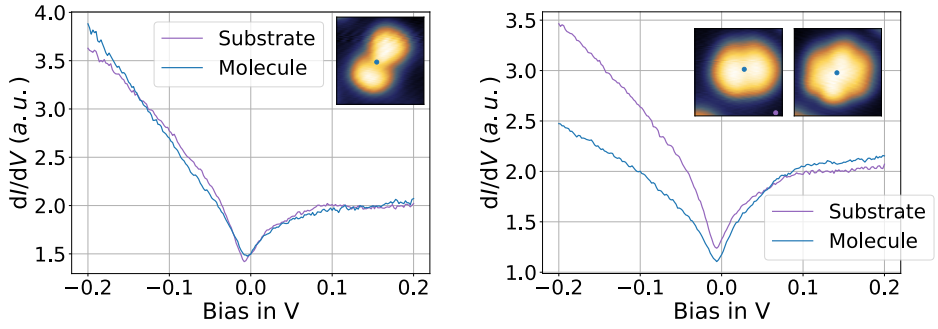

(a) Molecule type A **(b)** Molecule type B

Figure 6.8: Differential conductance spectra on Fe-Phen on Fe_2N. The energy resolution is very limited due to the high temperature and high lock-in modulation. No zero-bias anomaly was observed. The insets show the respective topography and the lateral tip position during the spectra. Lock-in parameters: 5 mV modulation at 2.2 kHz. Topography parameters: (a) (3 nm × 3 nm, 1 V, 50 pA), (b) (2.5 nm × 2.5 nm, ∓1 V, 50 pA).

Strangely, it appears as if the two states are merely rotated by 90°. This is illustrated more compellingly for the molecule in figure 6.10. Besides its topography, also a differential conductance map for the two states is shown. In fact, all the features including the molecule's chirality remain unchanged upon switching. No displacement of its center of mass could be observed either. This was verified for the molecule in figure 6.10. A possible displacement of the molecule's center of mass due to the switching was determined to be smaller than 1 pm or smaller than 2.5 pm for topography and dI-dV, respectively. Figure 7 in appendix 3.1 shows additional dI-dV maps for the two molecular states for various energies. These measurements also indicate that this swichting is merely a rotation. In any case it appears very unlikely that this switching corresponds to the desired spin crossover transition. Last, figure 6.11 shows how indeed the orientation of every type B molecule can be change arbitrarily.

It is hard to fully understand why this switching appears as a rotation, although the two rotational states must be energetically degenerate due to the fourfold rotational symmetry of the Fe_2N. Assuming the molecule is bound to the substrate via its thiocyanate groups, such a transition should

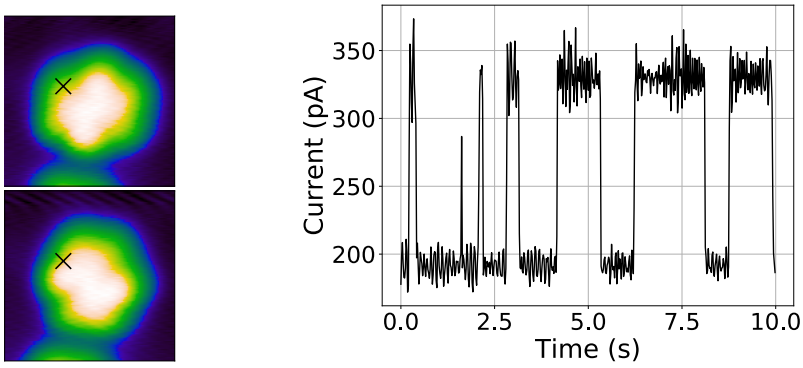

(a) Rotational-like switching **(b)** Random telegraph noise at 1.5 V

Figure 6.9: Images of the two states and the random telegraph noise of the rotational-like switching. (a) The cross indicates the tip position, where the random telegraph noise was recorded. Topography parameters: $(3\,\mathrm{nm} \times 3\,\mathrm{nm},\ 1\,\mathrm{V},\ 50\,\mathrm{pA})$. (b) The two states correspond to the two bistable current values observed in the time trace during the telegraph noise.

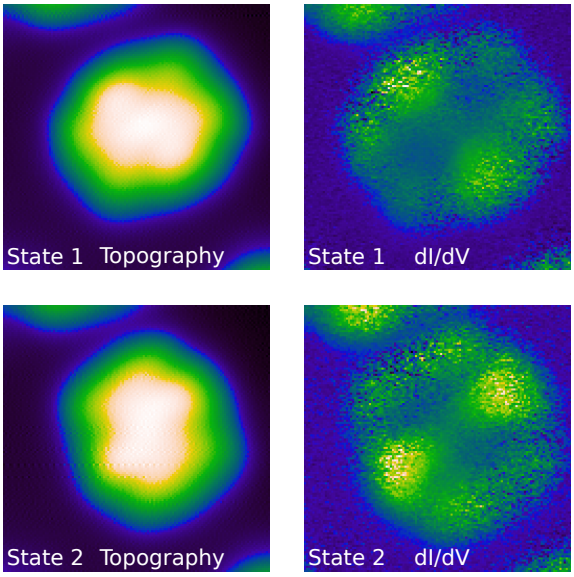

Figure 6.10: Topography and dI-dV-map of the two molecular states. No displacement for the center of mass for both, topography and map could be detected, which is consistent with a rotation. Topography parameters: $(0.8\,\mathrm{V},\ 500\,\mathrm{pA})$.

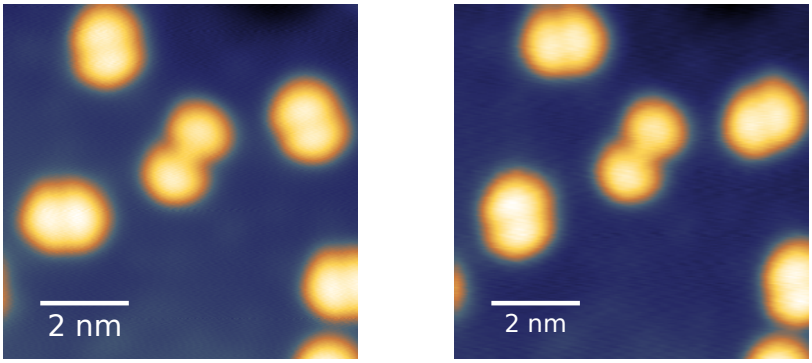

Figure 6.11: Switching the molecules at will. The four molecules were switched subsequently, proving that the rotational state can be chosen arbitrarily. Topography parameters: $(-1\,\mathrm{V},\ 50\,\mathrm{pA})$.

not be possible just like that, since a rotation required the simultaneous breaking of two sulfur-substrate bonds. In comparison, it should be more likely to break only one bond for a short time, such that switching events with a visible displacement should occur a lot more frequently than the actual observed rotation without displacement. On the other hand, it is plain that the molecules do not have any intrinsic rotational degree of freedom once the two sulfur-substrate bonds are fixed.

In conclusion, although the nature of the switching could not be fully understood, it seems plain that the measured system is not suited for the project described above.

6.3 Fe-Pyrz on LSMO

LSMO

As an alternative substrate, LSMO thin films epitaxially grown on STO were investigated. As an oxide, the LSMO surface is supposed to be inert, such that the coupling to adsorbed molecules is expected to be weak. Interestingly, LSMO still is ferromagnetic with Curie temperatures above room temperature and even electrically conductive, in contrast to undoped

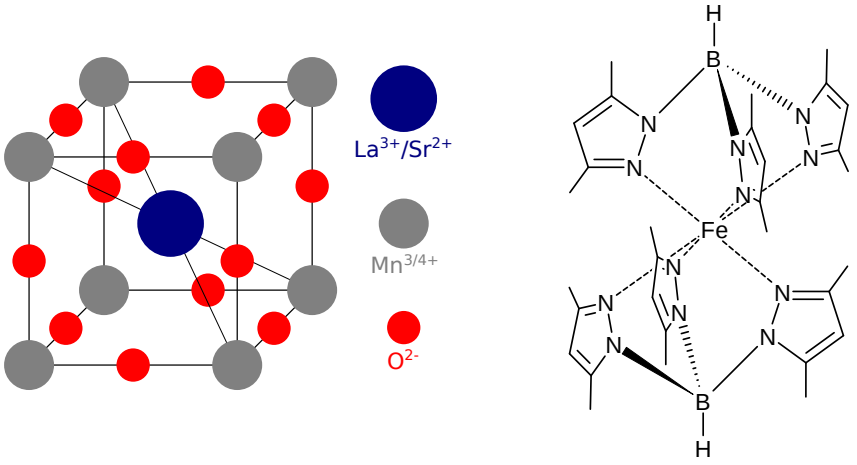

(a) Structure of LSMO **(b)** Fe-Pyrz structure

Figure 6.12: Structures of the LSMO substrate and the Fe-Pyrz SCO molecules. (a) Unit cell of the cubic perovskite structure of the LSMO. (b) Inside the Fe-Pyrz molecules, the divalent iron ion is surrounded by six nitrogen atoms in octahedral symmetry.

$LaMnO_3$ which is insulating and antiferromagnetic [46, 125]. The cause is a ferromagnetic double exchange between Mn^{3+} and Mn^{4+} ions, where the mixed valency originates from the strontium doping: Every La^{3+} ion that is replaced by a Sr^{2+} ion yields one Mn^{4+} ion instead of a Mn^{3+} ion, as is illustrated in the unit cell in figure 6.12a. The LSMO thin film samples used in this work are roughly 30 monolayers, epitaxially grown on niobium-doped STO and exhibit a strontium ratio close to the optimal concentration of $x \approx 0.3$ [125]. Thereby, the surface is oriented along the $[001]$ direction which results in two in-plane magnetic easy axes being aligned along the $\langle 110 \rangle$ directions [151]. The coercive field is estimated to be of the order of 10 Oe [152, 153].

Since the magnetism of LSMO - unlike Fe_2N - originates from manganese, this system is suited for XAS and XMCD investigations, because the substrate and adsorbed iron-based SCO molecules can be distinguished. Thereby, not only the molecules' spin state can be determined, but also evidence of magnetic interactions between the molecules and the substrate might be observed.

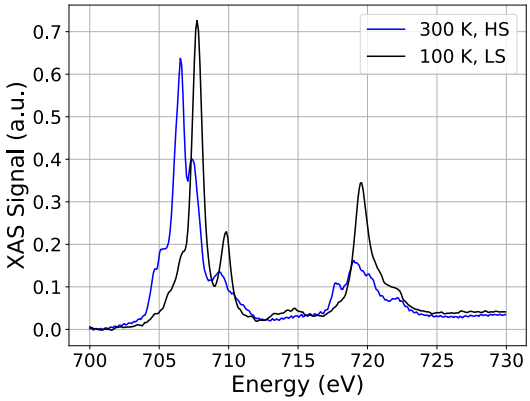

Figure 6.13: XAS performed on Fe-Pyrz powder. HS and LS state can readily be distinguished by the peak positions, shapes and ratios. These reference spectra correspond to the original data published in [101].

Fe-Pyrz

For this project, Fe-Pyrz SCO molecules were chosen [154]. Their structure is shown in figure 6.12b. In crystalline Fe-Pyrz, a thermal spin transition occurs at $T_{\mathrm{HS}\rightarrow\mathrm{LS}} = 174\,\mathrm{K}$ upon cooling. Conversely, upon warming up the SCO occurs at $T_{\mathrm{LS}\rightarrow\mathrm{HS}} = 199\,\mathrm{K}$. This difference is attributed to a structural phase transition [155, 156]. Figure 6.13 shows two reference x-ray absorption spectra of a powder sample of these molecules in HS and LS state, respectively. It is apparent that the two spin states can readily be distinguished in XAS. Additionally, LIESST and SOXIESST effect [101] was observed for these molecules. Moreover, it was reported, that these molecules can be sublimed easily without any decomposition. However, it was observed that the spin transition temperature might be different in thin films [155].

As emphasized before, the electronic interaction between the molecules and the substrate is crucial for this project, since SCO molecules might lose their ability to switch if the coupling is too strong. The Fe-Pyrz molecules are particularly interesting prospects, since they seem to be intrinsically inert in this regard. It was reported, that these molecules still remain switchable, even when directly adsorbed on Au(111) [100, 157]. At low temperatures

only about 1/3 of the molecules remain in the HS state while at room temperature all molecules are in the HS state. The spin transition of Fe-Pyrz/Au(111) could be observed thermally and by LIESST and SOXIESST effect.

6.3.1 Results

Growth study of Fe-Pyrz

As discussed already in section 3.5, the Fe-Pyrz/LSMO sample was prepared at the 4K setup and subsequently transferred to the WERA beam line using a vacuum suitcase in order to perform x-ray absorption measurements. The total coverage of Fe-Pyrz molecules was crucial for the synchrotron measurements: On the one hand, the coverage must be high enough such that a sufficiently large signal of the iron absorption edges can be measured. Since the main interest of this project is the magnetic coupling between molecules and substrate, though, the fraction of molecules in direct contact with the LSMO surface must be maximized. The optimum coverage is therefore exactly one monolayer. Unfortunately, the LSMO surface turned out to be rather rough, such that determination of the molecule coverage by STM measurements was not possible. To get an estimate on the amount of deposited molecules nevertheless, the deposition temperature and corresponding molecular growth rate was first checked on Cu(100). Figure 6.14 shows a topography measurement of such a sample of Fe-Pyrz/Cu(100). The deposition rate was determined from the deposition time and the coverage. Next, the amount of Fe-Pyrz molecules, that corresponds to slightly more than one monolayer on Cu(100), was deposited on LSMO. The difficulty lies in possibly different sticking coefficients for copper and LSMO. Hence, Auger electron spectroscopy (AES) measurements were supposed to be used in order to get a grasp on this problem. In doing so, the intensities of the iron resonances for Fe-Pyrz/LSMO and a sample of one monolayer Fe-Pyrz/Cu(100) were supposed to be compared. Unfortunately, the iron signals of both samples were too small in order to draw quantitative conclusions on the molecular coverage.

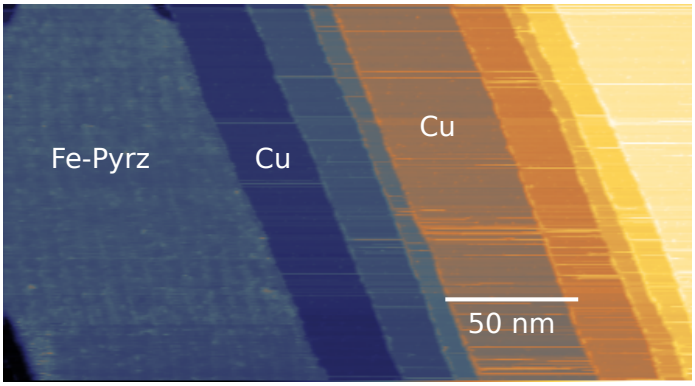

Figure 6.14: Topography of Fe-Pyrz on Cu(100). The deposited Fe-Pyrz molecules aggregate in large islands. Topography parameters: $(-1\,\mathrm{V},\ 100\,\mathrm{pA})$.

Kerr Measurements on LMSO

Before the transfer to the synchrotron, MOKE measurements were performed on the LSMO before and after the molecule deposition. Because of the given geometry of the 4K setup, these measurements represent a combination of longitudinal and polar MOKE. Moreover, the size of the applied magnetic field, which is proportional to the current through the coil, is not calibrated. Hence, these measurements are suited only to detect relative changes in the coercivity of the sample. Such a change could occur because of a magnetic interaction with HS Fe-Pyrz molecules. In this case, a SCO that occurs during a temperature dependent measurement might even occur as a sudden change of the coercivity.
Figure 6.15a shows some examples of acquired hysteresis curves. With this it is ensured, that the LSMO substrate is indeed ferromagnetic at room temperature. The different plots are scaled in the same way. The small difference in the general shape is related to a slightly different geometry for the two measurement.
In the next step, the coercive fields were determined as function of the sample temperature. For this, the sample manipulator was first cooled by continuous flow cooling using liquid nitrogen. Afterwards, the hysteresis curves were acquired at various temperatures while the sample was warming up. In figure 6.15b the extracted coercive fields are plotted for the sample before and after the molecule deposition. The magnitudes of both

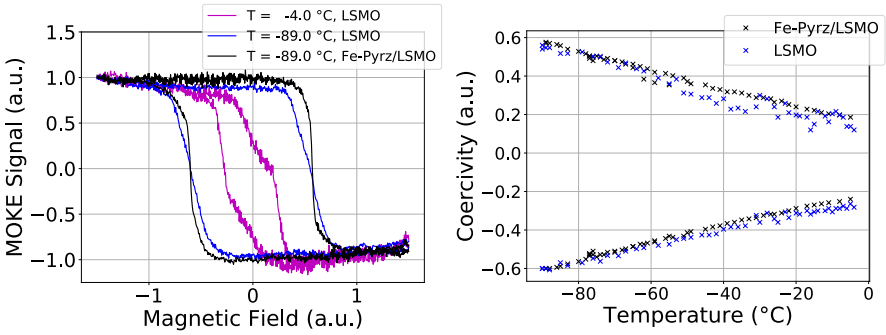

(a) Hysteresis acquired by MOKE **(b)** Coercivity

Figure 6.15: MOKE measurements on LSMO and Fe-Pyrz/LSMO. (a) Normalized hysteresis curves measured by MOKE. (b) Extracted coercive fields as function of temperature. No significant difference can be detected for the coercive fields after the molecule deposition.

coercive fields decrease gradually as the temperature increases and no clear difference occurs for the sample before and after molecule deposition. No rapid change is observable either. Perhaps, this might be attributed to not reaching the spin transition temperature yet. Nevertheless, no hint for any magnetic interaction between the LSMO and the Fe-Pyrz could be observed.

X-ray Absorption Spectroscopy on Fe-Pyrz on LSMO

Last, the presented sample of Fe-Pyrz molecules on LSMO was investigated by means of XAS and XMCD at the WERA beam line, which was presented in chapter 3.5. The sample was transferred from the 4K setup to the beamline using a vacuum suitcase, as described earlier in chapter 3.5. As illustrated in figure 6.13, one can readily distinguish the spin states of Fe-Pyrz using XAS. Hence, by measuring at various temperatures it is straightforward to examine whether or not the spin crossover still occurs for the molecules on the LSMO film. By means of XMCD, additional information on the magnetic properties of this system were supposed to be extracted. This might allow conclusions about any possible exchange interaction between the molecules and the LSMO substrate. For instance, by comparing the

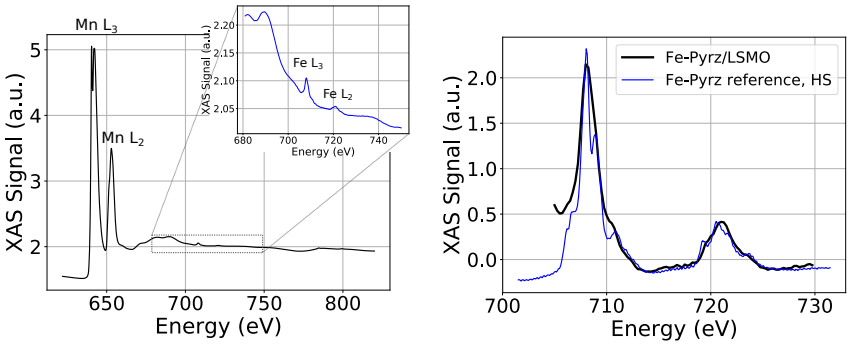

(a) XAS overview spectrum **(b)** XAS on Fe edges

Figure 6.16: XAS on Fe-Pyrz/LSMO and identification of HS state. (a) Overview spectrum of the Fe-Pyrz/LSMO sample is shown. (b) Reference XAS spectrum of the L_3 and L_2 edges of iron of the Fe-Pyrz powder sample of [101] in the HS state (scaled and offset in x and y) is superimposed on a measured spectrum on the Fe-Pyrz/LSMO sample. These spectra were measured at room temperature and grazing incidence (60°).

signs of the XMCD of iron and manganese one could determine whether the exchange is ferromagnetic or anti-ferromagnetic.

To begin with, figure 6.16a shows an overview spectrum of the sample. As expected, the largest signal arises from the manganese of the LSMO substrate. The respective L_3 and L_2 absorption edges are marked. The small inset shows a subsequently acquired spectrum of the iron edges including their position in the overview scan. This already illustrates the largest challenge for this experiment: The iron signal is small and occurs on a large, non-flat manganese background. In fact, this background may even vary slightly for subsequent spectra. This holds difficulties especially for XMCD measurements, since the XMCD is the difference of two spectra of different polarization or opposite magnetic field. Thus, a background correction was often necessary. Thereby, the corrections used in the following only included scaling, substracting a constant or linear background, correcting a background slope and normalizing the size of the edge jump.

First of all, the spin state of the molecules at room temperature was determined. Figure 6.16b shows a spectrum of the two iron edges together with the reference data on the powder sample in the HS state of figure 6.13 from

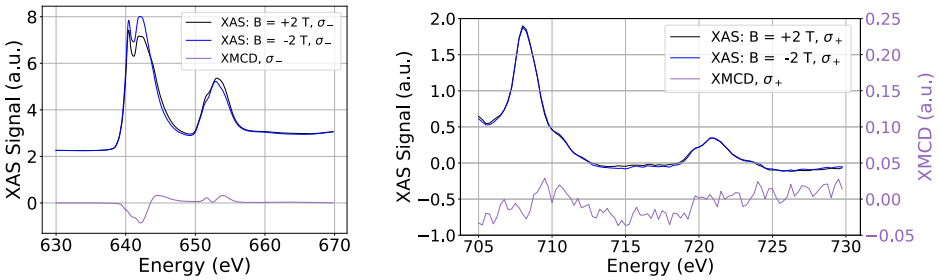

(a) XMCD of Mn edges **(b)** XMCD of Fe edges

Figure 6.17: XMCD on Fe-Pyrz/LSMO at room temperature. Both spectra were measured at grazing incidence (60°) with ±2 T of magnetic field. (a) The XMCD of manganese is clearly visible. Raw data were used. (b) For iron no clear XMCD signal could be detected. The XMCD signal is magnified by a factor of 10. Here a background and offset correction was performed.

[101]. Therein, the reference spectrum was scaled and appropriate y- and x-offsets were included. The latter was necessary, because the energy calibration of the reference data is surprisingly different to the measurements of this work. Nevertheless, one can directly recognize the resemblance to the reference spectrum. Both, the ratio of the peak heights and the relative peak position, as well as the peak shapes of the HS reference seem to be well-reproduced. Hence, the majority of the adsorbed molecules is in the HS state. For the sake of completeness, figure 8 in appendix 3.2 shows the same plot for the LS reference spectrum, from which it is apparent that the measured spectra are not compatible with the molecules in the LS state.

Since the molecules exhibit a magnetic moment, in the next step the XMCD was supposed to be measured. Figure 6.17a shows this demonstratively for the manganese edges, for starters: Two XAS spectra with equal polarization but opposite magnetic field (±2 T) and their difference as XMCD are plotted. As verified already by the MOKE measurements, this again is proof that the LSMO is indeed magnetic at room temperature. Next, figure 6.17b shows the same measurement for the iron edges. However, no clear XMCD can be identified. Most likely the iron signal and the respective signal-to-noise ratio are simply too small for such a measurement.

The next step was to check whether the adsorbed molecules still undergo the spin transition. For this purpose, the XAS measurement was repeated at low temperatures, as is shown in figure 6.18a. For both 30 K and 120 K no change in the spectrum can be observed. This means that the molecules cannot switch their spin state anymore and are pinned to the HS state. The additional measurement at 120 K was performed in order to avoid any effects of the SOXIESST effect (section 2.4.4). At this temperature the thermal relaxation to the LS ground state is fast enough, such that the spin state trapping is not possible anymore. Furthermore, this temperature is still well-above the structural phase transition of the STO substrate, which occurs at roughly 105 K [158].

Finally, for the sake of completeness, an attempt to measure the XMCD of iron at low temperature was performed. The reason is the following: The reported exchange for Fe-Phen molecules on cobalt was 22.6 meV [145], which is the same order of magnitude as $k_B T \sim 26\,\text{meV}$ at room temperature. Expecting, that any exchange of Fe-Pyrz molecules to the LSMO substrate is of the same order or smaller, it might very well be that the molecular spins are not fully aligned at room temperature, but thermally fluctuating. The applied magnetic field of 2 T is way too weak in order to align the spins, either.
The corresponding measurement at 30 K is shown in figure 6.18b. Still, no clear XMCD signal could be detected.

In conclusion one can see, that the Fe-Pyrz molecules are pinned to the HS state when adsorbed on LSMO. No thermal spin crossover occurs and no XMCD signal could be observed.

6.4 Conclusion

In conclusion, two different systems of SCO molecules on weak-coupling ferromagnetic substrates were investigated. The objective was to check whether or not the adsorbed molecules maintain their ability to switch the spin state, and whether HS molecules are magnetically coupled to the

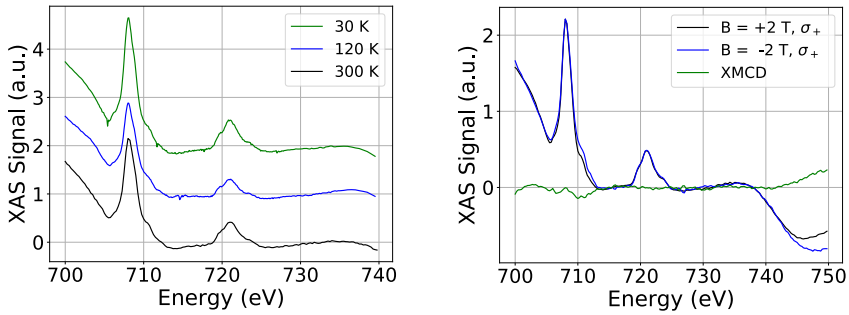

(a) XAS on Fe edges **(b)** XMCD on Fe edges

Figure 6.18: Temperature-dependend XAS and XMCD at 30 K for Fe.
(a) The shape of the XAS spectra does not change with temperature. Hence, no thermal spin crossover occurs for Fe-Pyrz molecules on LSMO. All spectra were measured at grazing incidence (60°) with linear polarization. The spectrum at 300 K corresponds to room temperature, where the precise temperature was not measured. The spectra are offset for clarity. (b) No clear XMCD signal could be detected at the L_3 and L_2 edges. The spectra were measured at 30 K and grazing incidence (60°) with ±2 T of magnetic field. A background correction was performed for all spectra shown.

substrate.
Firstly, Fe-Phen on a monolayer of $Fe_2N/Cu(100)$ was examined. There, three types of adsorbates occurred. Two of these adsorbates resembled Fe-Phen on Cu(100) in topography. No transitions of one molecule between these different types could be observed, though. On a later sample, only one of those molecule types occurred. These molecules showed a switching between two states, which in topography and differential conductance maps appears as a rotation by 90°. Hence, it seems unlikely that this switching corresponds to the SCO. Nevertheless, the nature of this switching could not be fully understood.
Secondly, Fe-Pyrz on LSMO thin films on STO were investigated. By means of XAS it was shown, that the majority of adsorbed molecules are pinned to the HS state, irrespective of the sample temperature. Hence, the SCO is quenched in this system. However, no XMCD signal of these HS molecules could be detected. In MOKE, no evidence of any magnetic interactions between Fe-Pyrz and LSMO could be observed, either.

7 Conclusion and Outlook

In the framework of this thesis three different projects regarding magnetic metal-organic molecules and their interactions with metallic substrates were investigated. Therein, the main questions were how the magnetic properties are affected by the interaction with the substrate, whether and how the molecular magnetic moments can be read out and addressed electronically in STM and finally whether such a material system may be suited for future technical application in data storage, quantum computing or for multifunctional devices. This chapter aims to summarize the main achievements of this dissertation and to offer possible outlooks and future experiments.

Transition metal acetylacetonates as 3d single-ion magnets were investigated on Cu(111) concerning their magnetic properties and suitability as SMMs. For the two compounds $Co(acac)_3$ and $Cr(acac)_3$ a total of three different types of adsorbates were identified and studied using STM and STS. Two of these objects - one for each of the two compounds - seemed to be bound only to two remaining acetylacetonate ligands. Consequently, these molecules with only twofold rotational symmetry cannot represent stable spin systems. Depending on the number of 3d electrons (Cr or Co), these adsorbates represent either a Kondo system (odd number) or a singlet (even number). The third type of molecule, that was observed, exhibits a threefold rotational symmetry, which might possibly correspond to a stable spin. Overall, this study illustrates, how the symmetry and molecular structure of adsorbed molecules are crucial for stable SMMs.

$DyPc_2$ as 4f single-ion magnet was presumed more promising. The main achievement of this study is the readout of the dysprosium spin using STM, which was based on the previous reports on the similar $TbPc_2$ molecules [16, 127, 128]. When adsorbed on Au(111), the molecules behave like a quantum

dot with an odd number of electrons and show a Kondo resonance, which results from the Kondo screening of an unpaired electron on one of the phthalocyanine ligands. Because of a ferromagnetic exchange coupling to the dysprosium magnetic moment, this resonance splits into two peaks. In the next step this exchange was exploited to address the dysprosium spin indirectly. Using spin-polarized spectroscopy, the polarization of the unpaired spin 1/2 - and thus the behavior of dysprosium - was investigated for one molecule. The results suggest, that the dysprosium moment follows a thermal population of its spin states, such that it is not stable on the time scale of the experiments of roughly 1 ms. In this context, the possible influence of the dysprosium nuclear spin was discussed. As dysprosium occurs in various isotopes with different nuclear spins, these experiments should be repeated on samples with isotopically enriched $DyPc_2$ molecules in the future. This should provide more insights on the spin stability and might even enable the nuclear spin readout of dysprosium in STM.

Generally, this principle of indirectly addressing a 4f magnetic moment in STM may be transferable to other SMMs. This requires simply one unpaired electron on the molecule, that is exchange-coupled to this 4f spin. In the case of $DyPc_2$ this automatically results from the adsorption on Au(111), which fortunately offers the correct work function and electronic structure. It is conceivable to synthesize SMMs as radicals, which means that they intrinsically exhibit an unpaired electron. Another interesting prospect is given by the possibility of using similar triple-decker molecules containing two lanthanide ions or even higher stacks [159, 160, 161, 162]. In view to potential application in quantum information processing, this would offer an interesting approach towards scalability and increasing the number of qubits. The prerequisite would be a suitable magnetic coupling between the lanthanide ions of one molecule.

Last, spin crossover molecules on ferromagnetic substrates were examined. The main question was, whether the molecules maintain the switching ability of their spin state in spite of the electronic interaction to the substrate, while being magnetically exchange-coupled to the substrate at the same time. For this purpose two different material systems were studied. Firstly, Fe-Phen molecules on Fe_2N/Cu(100) were examined using STM. Three

types of adsorbates were observed, two of which presumably correspond to the Fe-Phen molecules. No transitions between the different types and no spin crossover transitions were observed. A reversible switching between two stable states, which appears as a rotation of the molecule, was detected for one adsorbate type. However, this system does not fulfill the previous expectations.
Secondly, one monolayer of Fe-Pyrz molecules on LSMO was studied using XAS and XMCD measurements. It turns out, that the majority of the adsorbed molecules are in the high spin state regardless of the temperature. Furthermore, no hints towards an exchange-coupling could be observed in XMCD.

As a future prospect for this project, Fe-Pyrz on a substrate of Co/Au(111) will be investigated. Interestingly, on this substrate gold diffuses on top of the cobalt film when properly annealed [163]. This should provide a protective layer for the molecules and ensure, that they maintain their switching ability. The latter was already reported for Fe-Pyrz on Au(111) [100, 157]. Still, an indirect magnetic interaction similar to interlayer exchange coupling [164, 165] is expected between the cobalt and the high spin molecules.

Altogether, the results of this dissertation are of significant relevance for the research on SMMs and molecular spintronics. Especially the demonstration of the electronic readout of SMMs based on rare earth ions in STM seems very auspicious for future STM studies of such molecules.

Bibliography

[1] L. Bogani and W. Wernsdorfer: *Molecular spintronics using single-molecule magnets*. Nature Materials **7**.3 (2008), pp. 179–186 (cit. on p. 1).

[2] D. P. DiVincenzo: *Quantum computation*. Science **270**.5234 (1995), pp. 255–261 (cit. on p. 1).

[3] S. Lloyd: *A potentially realizable quantum computer*. Science **261**.5128 (1993), pp. 1569–1571 (cit. on p. 1).

[4] D. Loss and D. P. DiVincenzo: *Quantum computation with quantum dots*. Physical Review A **57**.1 (1998), p. 120 (cit. on p. 1).

[5] J. J. Pla, K. Y. Tan, J. P. Dehollain, W. H. Lim, J. J. Morton, D. N. Jamieson, A. S. Dzurak, and A. Morello: *A single-atom electron spin qubit in silicon*. Nature **489**.7417 (2012), pp. 541–545 (cit. on p. 1).

[6] T. Miyamachi, T. Schuh, T. Märkl, C. Bresch, T. Balashov, A. Stöhr, C. Karlewski, S. André, M. Marthaler, M. Hoffmann, M. Geilhufe, S. Ostanin, W. Hergert, I. Mertig, G. Schön, A. Ernst, and W. Wulfhekel: *Stabilizing the magnetic moment of single holmium atoms by symmetry*. Nature **503**.7475 (2013), pp. 242–246 (cit. on p. 1).

[7] M. N. Leuenberger and D. Loss: *Quantum computing in molecular magnets*. Nature **410**.6830 (2001), pp. 789–793 (cit. on pp. 1, 2).

[8] J. L. O'brien: *Optical quantum computing*. Science **318**.5856 (2007), pp. 1567–1570 (cit. on p. 1).

[9] Y. Makhlin, G. Schön, and A. Shnirman: *Quantum-state engineering with Josephson-junction devices*. Reviews of Modern Physics **73** (2001), pp. 357–400 (cit. on p. 1).

[10] A. Caneschi, D. Gatteschi, R. Sessoli, A. L. Barra, L. C. Brunel, and M. Guillot: *Alternating current susceptibility, high field magnetization, and millimeter band EPR evidence for a ground S = 10 state in [$Mn_{12}O_{12}(CH_3COO)_{16}(H_2O)_4$]· $2CH_3COOH·4H_2O$*. Journal of the American Chemical Society **113**.15 (1991), pp. 5873–5874 (cit. on p. 2).

[11] R. Sessoli, H. L. Tsai, A. R. Schake, S. Wang, J. B. Vincent, K. Folting, D. Gatteschi, G. Christou, and D. N. Hendrickson: *High-spin molecules:[$Mn_{12}O_{12}(O_2CR)_{16}(H_2O)_4$]*. Journal of the American Chemical Society **115**.5 (1993), pp. 1804–1816 (cit. on p. 2).

[12] R. Sessoli, D. Gatteschi, A. Caneschi, and M. Novak: *Magnetic bistability in a metal-ion cluster*. Nature **365**.6442 (1993), pp. 141–143 (cit. on p. 2).

[13] C. A. Goodwin, F. Ortu, D. Reta, N. F. Chilton, and D. P. Mills: *Molecular magnetic hysteresis at 60 kelvin in dysprosocenium*. Nature **548**.7668 (2017), pp. 439–442 (cit. on p. 2).

[14] M. Shiddiq, D. Komijani, Y. Duan, A. Gaita-Ariño, E. Coronado, and S. Hill: *Enhancing coherence in molecular spin qubits via atomic clock transitions*. Nature **531**.7594 (2016), pp. 348–351 (cit. on p. 2).

[15] E. Moreno-Pineda, M. Damjanović, O. Fuhr, W. Wernsdorfer, and M. Ruben: *Nuclear spin isomers: Engineering a Et_4N [$DyPc_2$] spin qudit*. Angewandte Chemie International Edition **56**.33 (2017), pp. 9915–9919 (cit. on pp. 2, 68, 70, 83).

[16] R. Vincent, S. Klyatskaya, M. Ruben, W. Wernsdorfer, and F. Balestro: *Electronic read-out of a single nuclear spin using a molecular spin transistor*. Nature **488**.7411 (2012), pp. 357–360 (cit. on pp. 2, 67, 70, 71, 73, 125).

[17] S. Thiele, F. Balestro, R. Ballou, S. Klyatskaya, M. Ruben, and W. Wernsdorfer: *Electrically driven nuclear spin resonance in single-molecule magnets*. Science **344**.6188 (2014), pp. 1135–1138 (cit. on p. 2).

[18] L. K. Grover: *Quantum mechanics helps in searching for a needle in a haystack*. Physical Review Letters **79** (1997), pp. 325–328 (cit. on p. 2).

[19] C. Godfrin, A. Ferhat, R. Ballou, S. Klyatskaya, M. Ruben, W. Wernsdorfer, and F. Balestro: *Operating Quantum States in Single Magnetic Molecules: Implementation of Grover's Quantum Algorithm*. Physical Review Letters **119** (2017), p. 187702 (cit. on pp. 2, 72).

[20] P. Gehring, J. M. Thijssen, and H. S. van der Zant: *Single-molecule quantum-transport phenomena in break junctions*. Nature Reviews Physics **1**.6 (2019), pp. 381–396 (cit. on p. 2).

[21] T. Böhler, J. Grebing, A. Mayer-Gindner, H. v Löhneysen, and E. Scheer: *Mechanically controllable break-junctions for use as electrodes for molecular electronics*. Nanotechnology **15**.7 (2004), p. 465 (cit. on p. 2).

[22] H. Park, A. K. Lim, A. P. Alivisatos, J. Park, and P. L. McEuen: *Fabrication of metallic electrodes with nanometer separation by electromigration*. Applied Physics Letters **75**.2 (1999), pp. 301–303 (cit. on p. 2).

[23] G. Binnig, H. Rohrer, C. Gerber, and E. Weibel: *Surface studies by scanning tunneling microscopy*. Physical Review Letters **49** (1982), pp. 57–61 (cit. on pp. 2, 6).

[24] N. Tsukahara, K.-i. Noto, M. Ohara, S. Shiraki, N. Takagi, Y. Takata, J. Miyawaki, M. Taguchi, A. Chainani, S. Shin, and M. Kawai: *Adsorption-induced switching of magnetic anisotropy in a single iron (II) phthalocyanine molecule on an oxidized Cu(110) surface*. Physical Review Letters **102**.16 (2009), p. 167203 (cit. on p. 3).

[25] J. Chen, H. Isshiki, C. Baretzky, T. Balashov, and W. Wulfhekel: *Abrupt switching of crystal fields during formation of molecular contacts*. ACS Nano **12**.4 (2018), pp. 3280–3286 (cit. on p. 3).

[26] J. A. Real, A. B. Gaspar, and M. C. Muñoz: *Thermal, pressure and light switchable spin-crossover materials*. Dalton Transactions 12 (2005), pp. 2062–2079 (cit. on pp. 3, 36, 39).

[27] P. K. Hansma and J. Tersoff: *Scanning tunneling microscopy*. Journal of Applied Physics **61**.2 (1987), R1–R24 (cit. on pp. 6, 8, 9).

[28] G. Binnig and D. P. Smith: *Single-tube three-dimensional scanner for scanning tunneling microscopy*. Review of Scientific Instruments **57**.8 (1986), pp. 1688–1689 (cit. on pp. 6, 53).

[29] F. Schwabl, ed.: *Quantenmechanik (QM I) : Eine Einführung*. 7th ed. Springer-Lehrbuch. Berlin, Heidelberg: Springer Berlin Heidelberg, 2007 (cit. on pp. 7–9).

[30] J. C. Cuevas and E. Scheer: *Molecular electronics : an introduction to theory and experiment*. World Scientific series in nanoscience and nanotechnology ; 1. Chapter 4.4. Hackensack, NJ: World Scientific, 2010 (cit. on pp. 7, 8).

[31] C. Joachim, J. K. Gimzewski, R. R. Schlittler, and C. Chavy: *Electronic transparence of a single C_{60} molecule*. Physical Review Letters **74** (1995), pp. 2102–2105 (cit. on p. 8).

[32] E. Scheer, N. Agraït, J. C. Cuevas, A. L. Yeyati, B. Ludoph, A. Martín-Rodero, G. R. Bollinger, J. M. van Ruitenbeek, and C. Urbina: *The signature of chemical valence in the electrical conduction through a single-atom contact*. Nature **394**.6689 (1998), pp. 154–157 (cit. on p. 8).

[33] J. Fisher and I. Giaever: *Tunneling through thin insulating layers*. Journal of Applied Physics **32**.2 (1961), pp. 172–177 (cit. on p. 9).

[34] J. J. Sakurai: *Modern quantum mechanics*. Rev. ed. Reading, Mass.: Addison-Wesley, 1994 (cit. on p. 9).

[35] J. Bardeen: *Tunnelling from a many-particle point of view*. Physical Review Letters **6**.2 (1961), p. 57 (cit. on p. 9).

[36] J. Tersoff and D. Hamann: *Theory and application for the scanning tunneling microscope*. Physical Review Letters **50**.25 (1983), p. 1998 (cit. on p. 9).

[37] F. Hooge, T. Kleinpenning, and L. Vandamme: *Experimental studies on 1/f noise*. Reports on progress in Physics **44**.5 (1981), p. 479 (cit. on p. 10).

[38] B. Voigtländer: *Scanning probe microscopy : Atomic force microscopy and scanning tunneling microscopy*. NanoScience and Technology. Berlin, Heidelberg: Springer, 2015 (cit. on p. 11).

[39] B. Stipe, M. Rezaei, and W. Ho: *Single-molecule vibrational spectroscopy and microscopy*. Science **280**.5370 (1998), pp. 1732–1735 (cit. on p. 11).

[40] H. Gawronski, M. Mehlhorn, and K. Morgenstern: *Imaging phonon excitation with atomic resolution*. Science **319**.5865 (2008), pp. 930–933 (cit. on p. 11).

[41] T. Balashov, A. Takács, W. Wulfhekel, and J. Kirschner: *Magnon excitation with spin-polarized scanning tunneling microscopy*. Physical Review Letters **97**.18 (2006), p. 187201 (cit. on p. 11).

[42] A. Heinrich, J. Gupta, C. Lutz, and D. Eigler: *Single-atom spin-flip spectroscopy*. Science **306**.5695 (2004), pp. 466–469 (cit. on p. 11).

[43] J.-P. Gauyacq, N. Lorente, and F. D. Novaes: *Excitation of local magnetic moments by tunneling electrons*. Progress in Surface Science **87**.5 (2012), pp. 63–107 (cit. on p. 11).

[44] M. Bode: *Spin-polarized scanning tunnelling microscopy*. Reports on Progress in Physics **66**.4 (2003), p. 523 (cit. on p. 12).

[45] M. Julliere: *Tunneling between ferromagnetic films*. Physics Letters A **54**.3 (1975), pp. 225–226 (cit. on p. 13).

[46] S. Blundell: *Magnetism in condensed matter*. Repr. Oxford Master Series in Physics 4. Oxford: Oxford University Press, 2006 (cit. on pp. 13, 19, 20, 29, 45, 116).

[47] J. C. Slonczewski: *Conductance and exchange coupling of two ferromagnets separated by a tunneling barrier*. Physical Review B **39** (1989), pp. 6995–7002 (cit. on p. 14).

[48] R. Wiesendanger, H.-J. Güntherodt, G. Güntherodt, R. J. Gambino, and R. Ruf: *Observation of vacuum tunneling of spin-polarized electrons with the scanning tunneling microscope*. Physical Review Letters **65** (1990), pp. 247–250 (cit. on p. 14).

[49] M. Pratzer, H. J. Elmers, M. Bode, O. Pietzsch, A. Kubetzka, and R. Wiesendanger: *Atomic-Scale Magnetic Domain Walls in Quasi-One-Dimensional Fe Nanostripes*. Physical Review Letters **87** (2001), p. 127201 (cit. on p. 14).

[50] S. Heinze, K. Von Bergmann, M. Menzel, J. Brede, A. Kubetzka, R. Wiesendanger, G. Bihlmayer, and S. Blügel: *Spontaneous atomic-scale magnetic skyrmion lattice in two dimensions*. Nature Physics **7**.9 (2011), pp. 713–718 (cit. on p. 14).

[51] M. Bode, M. Getzlaff, and R. Wiesendanger: *Spin-polarized vacuum tunneling into the exchange-split surface state of Gd (0001)*. Physical Review Letters **81**.19 (1998), p. 4256 (cit. on pp. 14, 15).

[52] A. Kubetzka, M. Bode, O. Pietzsch, and R. Wiesendanger: *Spin-Polarized Scanning Tunneling Microscopy with Antiferromagnetic Probe Tips*. Physical Review Letters **88** (2002), p. 057201 (cit. on p. 15).

[53] A. Li Bassi, C. S. Casari, D. Cattaneo, F. Donati, S. Foglio, M. Passoni, C. E. Bottani, P. Biagioni, A. Brambilla, and M. Finazzi: *Bulk Cr tips for scanning tunneling microscopy and spin-polarized scanning tunneling microscopy*. Applied Physics Letters **91**.17 (2007), p. 173120 (cit. on p. 15).

[54] P. Forrester, T. Bilgeri, F. Patthey, H. Brune, and F. Natterer: *Antiferromagnetic MnNi tips for spin-polarized scanning probe microscopy*. Review of Scientific Instruments **89**.12 (2018), p. 123706 (cit. on p. 15).

[55] O. Pietzsch, A. Kubetzka, M. Bode, and R. Wiesendanger: *Spin-polarized scanning tunneling spectroscopy of nanoscale cobalt islands on Cu(111)*. Physical Review Letters **92** (2004), p. 057202 (cit. on pp. 16, 63).

[56] W. Wulfhekel and J. Kirschner: *Spin-polarized scanning tunneling microscopy on ferromagnets*. Applied Physics Letters **75**.13 (1999), pp. 1944–1946 (cit. on p. 16).

[57] U. Schlickum, W. Wulfhekel, and J. Kirschner: *Spin-polarized scanning tunneling microscope for imaging the in-plane magnetization*. Applied physics letters **83**.10 (2003), pp. 2016–2018 (cit. on p. 16).

[58] J. Muscat and D. Newns: *Chemisorption on metals*. Progress in Surface Science **9**.1 (1978), pp. 1–43 (cit. on p. 17).

[59] J. Norsko: *Chemisorption on metal surfaces*. Reports on Progress in Physics **53**.10 (1990), p. 1253 (cit. on p. 17).

[60] X.-Y. Zhu: *Electronic structure and electron dynamics at molecule–metal interfaces: implications for molecule-based electronics*. Surface Science Reports **56**.1-2 (2004), pp. 1–83 (cit. on p. 17).

[61] J. C. Cuevas and E. Scheer: *Molecular electronics : an introduction to theory and experiment*. World Scientific Series in Nanoscience and Nanotechnology 1. Chapter 5.5.3. Hackensack, NJ: World Scientific, 2010 (cit. on p. 18).

[62] J. M. D. Coey: *Magnetism and magnetic materials*. Cambridge: Cambridge University Press, 2010 (cit. on pp. 19, 20, 29, 30, 35, 36).

[63] W. Heisenberg: *Mehrkörperproblem und Resonanz in der Quantenmechanik*. Zeitschrift für Physik **38**.6-7 (1926), pp. 411–426 (cit. on p. 19).

[64] L. D. Landau and E. M. Lifšic: *Statistical physics*. Vol. 2: Theory of the condensed state. Course of Theoretical Physics 9. Oxford: Pergamon Press, 1980 (cit. on p. 21).

[65] F. Bloch: *Zum elektrischen Widerstandsgesetz bei tiefen Temperaturen*. Zeitschrift für Physik **59**.3-4 (1930), pp. 208–214 (cit. on p. 21).

[66] E. Grüneisen: *Die Abhängigkeit des elektrischen Widerstandes reiner Metalle von der Temperatur*. Annalen der Physik **408**.5 (1933), pp. 530–540 (cit. on p. 21).

[67] W. De Haas, J. De Boer, and G. Van den Berg: *The electrical resistance of gold, copper and lead at low temperatures*. Physica **1**.7-12 (1934), pp. 1115–1124 (cit. on p. 22).

[68] J. Kondo: *Resistance minimum in dilute magnetic alloys*. Progress of Theoretical Physics **32**.1 (1964), pp. 37–49 (cit. on pp. 22, 26).

[69] A. C. Hewson and A. C. Hewson: *The Kondo problem to heavy fermions*. 1. publ. Cambridge studies in magnetism 2. Cambridge: Cambridge University Press, 1993 (cit. on p. 22).

[70] C. Zener: *Interaction Between the d Shells in the Transition Metals*. Physical Review **81** (1951), pp. 440–444 (cit. on p. 22).

[71] T. Kasuya: *A theory of metallic ferro-and antiferromagnetism on Zener's model*. Progress of Theoretical Physics **16**.1 (1956), pp. 45–57 (cit. on p. 22).

[72] P. W. Anderson: *Localized magnetic states in metals*. Physical Review **124**.1 (1961), p. 41 (cit. on pp. 22, 24).

[73] K. G. Wilson: *The renormalization group: Critical phenomena and the Kondo problem*. Reviews of Modern Physics **47**.4 (1975), p. 773 (cit. on p. 23).

[74] Y.-h. Zhang, S. Kahle, T. Herden, C. Stroh, M. Mayor, U. Schlickum, M. Ternes, P. Wahl, and K. Kern: *Temperature and magnetic field dependence of a Kondo system in the weak coupling regime*. Nature Communications **4**.1 (2013), pp. 1–6 (cit. on pp. 23, 27).

[75] H. O. Frota and L. N. Oliveira: *Photoemission spectroscopy for the spin-degenerate Anderson model*. Physical Review B **33** (1986), pp. 7871–7874 (cit. on pp. 23, 25).

[76] H. O. Frota: *Shape of the Kondo resonance*. Physical Review B **45** (1992), pp. 1096–1099 (cit. on pp. 23, 25).

[77] M. Ternes, A. J. Heinrich, and W.-D. Schneider: *Spectroscopic manifestations of the Kondo effect on single adatoms*. Journal of Physics: Condensed Matter **21**.5 (2008), p. 053001 (cit. on pp. 23, 24).

[78] H. Manoharan, C. Lutz, and D. Eigler: *Quantum mirages formed by coherent projection of electronic structure*. Nature **403**.6769 (2000), pp. 512–515 (cit. on p. 24).

[79] N. Quaas, M. Wenderoth, A. Weismann, R. Ulbrich, and K. Schönhammer: *Kondo resonance of single Co atoms embedded in Cu (111)*. Physical Review B **69**.20 (2004), p. 201103 (cit. on p. 24).

[80] H. Prüser, M. Wenderoth, A. Weismann, and R. G. Ulbrich: *Mapping itinerant electrons around Kondo impurities*. Physical Review Letters **108** (2012), p. 166604 (cit. on p. 25).

[81] Y.-S. Fu, S.-H. Ji, X. Chen, X.-C. Ma, R. Wu, C.-C. Wang, W.-H. Duan, X.-H. Qiu, B. Sun, P. Zhang, J.-F. Jia, and Q.-K. Xue: *Manipulating the Kondo resonance through quantum size effects*. Physical Review Letters **99** (2007), p. 256601 (cit. on p. 25).

[82] S. Frank and D. Jacob: *Orbital signatures of Fano-Kondo line shapes in STM adatom spectroscopy*. Physical Review B **92** (2015), p. 235127 (cit. on p. 26).

[83] J. Appelbaum: *"$s - d$" exchange model of zero-bias tunneling anomalies*. Physical Review Letters **17**.2 (1966), p. 91 (cit. on p. 26).

[84] J. A. Appelbaum: *Exchange model of zero-bias tunneling anomalies*. Physical Review **154**.3 (1967), p. 633 (cit. on p. 26).

[85] P. W. Anderson: *Localized magnetic states and Fermi-surface anomalies in tunneling*. Physical Review Letters **17**.2 (1966), p. 95 (cit. on p. 26).

[86] M. Ternes: *Spin excitations and correlations in scanning tunneling spectroscopy*. New Journal of Physics **17**.6 (2015), p. 063016 (cit. on pp. 26, 27, 77, 78, 85, 86, 154, 155).

[87] M. Ternes: *Probing magnetic excitations and correlations in single and coupled spin systems with scanning tunneling spectroscopy*. Progress in Surface Science **92**.1 (2017), pp. 83–115 (cit. on p. 26).

[88] A. F. Otte, M. Ternes, K. Von Bergmann, S. Loth, H. Brune, C. P. Lutz, C. F. Hirjibehedin, and A. J. Heinrich: *The role of magnetic anisotropy in the Kondo effect*. Nature Physics **4**.11 (2008), pp. 847–850 (cit. on p. 27).

[89] R. Žitko, R. Peters, and T. Pruschke: *Splitting of the Kondo resonance in anisotropic magnetic impurities on surfaces*. New Journal of Physics **11**.5 (2009), p. 053003 (cit. on p. 27).

[90] K. von Bergmann, M. Ternes, S. Loth, C. P. Lutz, and A. J. Heinrich: *Spin polarization of the split Kondo state*. Physical Review Letters **114**.7 (2015), p. 076601 (cit. on p. 27).

[91] T. A. Costi: *Kondo effect in a magnetic field and the magnetoresistivity of Kondo alloys*. Physical Review Letters **85** (2000), pp. 1504–1507 (cit. on p. 27).

[92] A. J. Freeman and R. Watson: *Theoretical investigation of some magnetic and spectroscopic properties of rare-earth ions*. Physical Review **127**.6 (1962), p. 2058 (cit. on pp. 29, 67).

[93] A. Abragam and B. Bleaney: *Electron paramagnetic resonance of transition ions*. The International Series of Monographs on Physics. Oxford: Clarendon Press, 1970 (cit. on pp. 31, 35, 36).

[94] D. Gatteschi, R. Sessoli, and J. Villain: *Molecular nanomagnets*. Mesoscopic Physics and Nanotechnology 5. Oxford: Oxford University Press, 2006 (cit. on pp. 33, 35).

[95] T. Balashov, C. Karlewski, T. Märkl, G. Schön, and W. Wulfhekel: *Electron-assisted magnetization tunneling in single spin systems*. Physical Review B **97**.2 (2018), p. 024412 (cit. on p. 34).

[96] K. Stevens: *Matrix elements and operator equivalents connected with the magnetic properties of rare earth ions*. Proceedings of the Physical Society. Section A **65**.3 (1952), p. 209 (cit. on p. 35).

[97] E. König, G. Ritter, and S. Kulshreshtha: *The nature of spin-state transitions in solid complexes of iron (II) and the interpretation of some associated phenomena*. Chemical Reviews **85**.3 (1985), pp. 219–234 (cit. on p. 36).

[98] E. König and K. Madeja: $^5T_2$-$^1A_1$ *equilibria in some iron (II)-bis(1,10-phenanthroline) complexes*. Inorganic Chemistry **6**.1 (1967), pp. 48–55 (cit. on p. 36).

[99] S. Decurtins, P. Gutlich, K. Hasselbach, A. Hauser, and H. Spiering: *Light-induced excited-spin-state trapping in iron (II) spin-crossover systems. Optical spectroscopic and magnetic susceptibility study*. Inorganic Chemistry **24**.14 (1985), pp. 2174–2178 (cit. on p. 36).

[100] K. Bairagi, O. Iasco, A. Bellec, A. Kartsev, D. Li, J. Lagoute, C. Chacon, Y. Girard, S. Rousset, F. Miserque, et al.: *Molecular-scale dynamics of light-induced spin cross-over in a two-dimensional layer*. Nature Communications **7**.1 (2016), pp. 1–7 (cit. on pp. 36, 117, 127).

[101] V. Davesne, M. Gruber, T. Miyamachi, V. Da Costa, S. Boukari, F. Scheurer, L. Joly, P. Ohresser, E. Otero, F. Choueikani, et al.: *First glimpse of the soft x-ray induced excited spin-state trapping effect dynamics on spin cross-over molecules*. The Journal of Chemical Physics **139**.7 (2013), p. 074708 (cit. on pp. 36, 41, 117, 121, 122, 161).

[102] T. Granier, B. Gallois, J. Gaultier, J. A. Real, and J. Zarembowitch: *High-pressure single-crystal x-ray diffraction study of two spin-crossover iron (II) complexes: $Fe(Phen)_2(NCS)_2$ and $Fe(Btz)_2(NCS)_2$*. Inorganic Chemistry **32**.23 (1993), pp. 5305–5312 (cit. on p. 36).

[103] T. Miyamachi, M. Gruber, V. Davesne, M. Bowen, S. Boukari, L. Joly, F. Scheurer, G. Rogez, T. K. Yamada, P. Ohresser, et al.: *Robust spin crossover and memristance across a single molecule*. Nature Communications **3**.1 (2012), pp. 1–6 (cit. on pp. 36, 104, 106, 108, 111).

[104] C. J. Ballhausen: *Introduction to ligand field theory*. McGraw-Hill Series in Advanced Chemistry. New York: McGraw-Hill Book Comp., 1962 (cit. on p. 38).

[105] E. Beaurepaire, H. Bulou, F. Scheurer, and J.-P. Kappler, eds.: *Magnetism: A synchrotron radiation approach*. SpringerLink. Berlin, Heidelberg: Springer Berlin Heidelberg, 2006 (cit. on pp. 41–43).

[106] G. Bunker: *Introduction to XAFS : a practical guide to x-ray absorption fine structure spectroscopy*. Cambridge: Cambridge University Press, 2010 (cit. on pp. 41, 43, 44).

[107] J. Stöhr: *X-ray magnetic circular dichroism spectroscopy of transition metal thin films*. Journal of Electron Spectroscopy and Related Phenomena **75** (1995), pp. 253–272 (cit. on pp. 42, 43).

[108] J. Stöhr and R. Nakajima: *Magnetic properties of transition-metal multilayers studied with X-ray magnetic circular dichroism spectroscopy*. IBM Journal of Research and Development **42**.1 (1998), pp. 73–88 (cit. on p. 42).

[109] T. Funk, A. Deb, S. J. George, H. Wang, and S. P. Cramer: *X-ray magnetic circular dichroism—a high energy probe of magnetic properties*. Coordination Chemistry Reviews **249**.1-2 (2005), pp. 3–30 (cit. on pp. 42, 43).

[110] J. Stöhr and H. König: *Determination of spin-and orbital-moment anisotropies in transition metals by angle-dependent X-ray magnetic circular dichroism*. Physical Review Letters **75**.20 (1995), p. 3748 (cit. on p. 43).

[111] P. Auger: *The Auger effect*. Surface Science **48**.1 (1975), pp. 1–8 (cit. on p. 44).

[112] M. P. Seah and W. Dench: *Quantitative electron spectroscopy of surfaces: A standard data base for electron inelastic mean free paths in solids*. Surface and Interface Analysis **1**.1 (1979), pp. 2–11 (cit. on p. 44).

[113] L. Tröger, D. Arvanitis, H. Rabus, L. Wenzel, and K. Baberschke: *Comparative study of fluorescence-and electron-yield detection on YB_2 Cu_3 $O_{7-\delta}$ at the O K edge through x-ray absorption*. Physical Review B **41**.10 (1990), p. 7297 (cit. on p. 44).

[114] U. Bergmann, P. Glatzel, and S. P. Cramer: *Bulk-sensitive XAS characterization of light elements: from X-ray Raman scattering to X-ray Raman spectroscopy*. Microchemical Journal **71**.2-3 (2002), pp. 221–230 (cit. on p. 44).

[115] J. Kerr: *On rotation of the plane of polarization by reflection from the pole of a magnet*. The London, Edinburgh, and Dublin Philosophical Magazine and Journal of Science **3**.19 (1877), pp. 321–343. DOI: 10.1080/14786447708639245 (cit. on p. 44).

[116] Z. Qiu and S. D. Bader: *Surface magneto-optic Kerr effect (SMOKE)*. Journal of Magnetism and Magnetic Materials **200**.1-3 (1999), pp. 664–678 (cit. on pp. 45–47).

[117] Z. Qiu and S. D. Bader: *Surface magneto-optic Kerr effect*. Review of Scientific Instruments **71**.3 (2000), pp. 1243–1255 (cit. on pp. 45–47).

[118] L. Zhang, T. Miyamachi, T. Tomanić, R. Dehm, and W. Wulfhekel: *A compact sub-Kelvin ultrahigh vacuum scanning tunneling microscope with high energy resolution and high stability*. Review of Scientific Instruments **82**.10 (2011), p. 103702 (cit. on pp. 49, 52, 54).

[119] L. Zhang: *Sub-Kelvin scanning tunneling microscopy on magnetic molecules*. PhD thesis, Experimental condensed matter physics ; Band 25. Karlsruhe: KIT Scientific Publishing, 2019 (cit. on pp. 49, 52, 93–95).

[120] T. Balashov, M. Meyer, and W. Wulfhekel: *A compact ultrahigh vacuum scanning tunneling microscope with dilution refrigeration*. Review of Scientific Instruments **89**.11 (2018), p. 113707 (cit. on pp. 49, 52, 54, 55).

[121] O. Lounasmaa: *Dilution refrigeration*. Journal of Physics E: Scientific Instruments **12**.8 (1979), p. 668 (cit. on p. 55).

[122] C. Enss and S. Hunklinger: *Tieftemperaturphysik*. Berlin: Springer, 2000 (cit. on pp. 55, 57).

[123] D. S. Betts: *An introduction to millikelvin technology*. 1. publ. Cambridge studies in low temperature physics 1. Cambridge: Cambridge University Press, 1989 (cit. on pp. 55, 57).

[124] Y. Takahashi, T. Miyamachi, S. Nakashima, N. Kawamura, Y. Takagi, M. Uozumi, V. Antonov, T. Yokoyama, A. Ernst, and F. Komori: *Thickness-dependent electronic and magnetic properties of γ'- Fe_4 N atomic layers on Cu(001)*. Physical Review B **95**.22 (2017), p. 224417 (cit. on pp. 59, 107, 158).

[125] A. Urushibara, Y. Moritomo, T. Arima, A. Asamitsu, G. Kido, and Y. Tokura: *Insulator-metal transition and giant magnetoresistance in La_{1-x} Sr_x MnO_3*. Physical Review B **51**.20 (1995), p. 14103 (cit. on pp. 60, 116).

[126] N. Ishikawa, M. Sugita, T. Ishikawa, S.-y. Koshihara, and Y. Kaizu: *Lanthanide double-decker complexes functioning as magnets at the single-molecular level*. Journal of the American Chemical Society **125**.29 (2003), pp. 8694–8695 (cit. on pp. 67, 68).

[127] T. Komeda, H. Isshiki, J. Liu, Y.-F. Zhang, N. Lorente, K. Katoh, B. K. Breedlove, and M. Yamashita: *Observation and electric current control of a local spin in a single-molecule magnet*. Nature Communications **2**.1 (2011), pp. 1–7 (cit. on pp. 67, 70–72, 74, 125).

[128] C. Godfrin, S. Thiele, A. Ferhat, S. Klyatskaya, M. Ruben, W. Wernsdorfer, and F. Balestro: *Electrical read-out of a single spin using an exchange-coupled quantum dot*. ACS Nano **11**.4 (2017), pp. 3984–3989 (cit. on pp. 67, 72, 125).

[129] N. Ishikawa, M. Sugita, T. Okubo, N. Tanaka, T. Iino, and Y. Kaizu: *Determination of ligand-field parameters and f-electronic structures of double-decker bis(phthalocyaninato)lanthanide complexes*. Inorganic Chemistry **42**.7 (2003), pp. 2440–2446 (cit. on pp. 68, 69, 71, 83, 85, 86).

[130] N. Koike, H. Uekusa, Y. Ohashi, C. Harnoode, F. Kitamura, T. Ohsaka, and K. Tokuda: *Relationship between the skew angle and interplanar distance in four bis(phthalocyaninato)lanthanide(III) Tetrabutylammonium Salts ($[NBu^n{}_4][Ln^{III}Pc_2]$; Ln= Nd, Gd, Ho, Lu)*. Inorganic Chemistry **35**.20 (1996), pp. 5798–5804 (cit. on p. 68).

[131] N. Ishikawa, M. Sugita, and W. Wernsdorfer: *Quantum tunneling of magnetization in lanthanide single-molecule magnets: Bis(phthalocyaninato)terbium and bis(phthalocyaninato)dysprosium anions*. Angewandte Chemie International Edition **44**.19 (2005), pp. 2931–2935 (cit. on pp. 68–70).

[132] F. Pointillart, K. Bernot, S. Golhen, B. Le Guennic, T. Guizouarn, L. Ouahab, and O. Cador: *Magnetic memory in an isotopically enriched and magnetically isolated mononuclear dysprosium complex*. Angewandte Chemie **127**.5 (2015), pp. 1524–1527 (cit. on p. 70).

[133] S. Thiele, R. Vincent, M. Holzmann, S. Klyatskaya, M. Ruben, F. Balestro, and W. Wernsdorfer: *Electrical readout of individual nuclear spin trajectories in a single-molecule magnet spin transistor*. Physical Review Letters **111**.3 (2013), p. 037203 (cit. on p. 72).

[134] K. von Bergmann, M. Ternes, S. Loth, C. P. Lutz, and A. J. Heinrich: *Spin polarization of the split Kondo state*. Physical Review Letters **114**.7 (2015), p. 076601 (cit. on pp. 79, 97, 153).

[135] J. Miller, N. Schaefle, and R. Sharp: *Calculating NMR paramagnetic relaxation enhancements without adjustable parameters: the spin-3/2 complex Cr(III)(AcAc)* $_3$. Magnetic Resonance in Chemistry **41**.10 (2003), pp. 806–812 (cit. on p. 92).

[136] P.-L. Wang, J.-H. Lee, S.-M. Huang, and L.-P. Hwang: *Proton spin relaxation in solutions of the complex tris(acetylacetonato)chromium(III)*. Journal of Magnetic Resonance (1969) **73**.2 (1987), pp. 277–286 (cit. on p. 92).

[137] L. Singer: *Paramagnetic resonance absorption in some* Cr^{+3} *complexes*. The Journal of Chemical Physics **23**.2 (1955), pp. 379–388 (cit. on p. 92).

[138] M. A. Siddiqi, R. A. Siddiqui, and B. Atakan: *Thermal stability, sublimation pressures and diffusion coefficients of some metal acetylacetonates*. Surface and Coatings Technology **201**.22-23 (2007), pp. 9055–9059 (cit. on p. 92).

[139] G. Beech and R. M. Lintonbon: *Thermal and kinetic studies of some complexes of 2,4-pentanedione*. Thermochimica Acta **3**.2 (1971), pp. 97–105 (cit. on pp. 92, 99).

[140] A. Rautiainen, M. Lindblad, L. B. Backman, and R. L. Puurunen: *Preparation of silica-supported cobalt catalysts through chemisorption of cobalt(II) and cobalt(III) acetylacetonate*. Physical Chemistry Chemical Physics **4**.11 (2002), pp. 2466–2472 (cit. on pp. 92, 99).

[141] S. Schmaus: *Spintronics with individual metal-organic molecules*. PhD thesis, Experimental condensed matter physics ; 2. Karlsruhe: KIT Scientific Publishing, 2011 (cit. on pp. 93–95).

[142] T. G. Gopakumar, F. Matino, H. Naggert, A. Bannwarth, F. Tuczek, and R. Berndt: *Electron-induced spin crossover of single molecules in a bilayer on gold*. Angewandte Chemie International Edition **51**.25 (2012), pp. 6262–6266 (cit. on p. 104).

[143] M. Gruber, V. Davesne, M. Bowen, S. Boukari, E. Beaurepaire, W. Wulfhekel, and T. Miyamachi: *Spin state of spin-crossover complexes: From single molecules to ultrathin films*. Physical Review B **89**.19 (2014), p. 195415 (cit. on p. 104).

[144] M. Gruber, T. Miyamachi, V. Davesne, M. Bowen, S. Boukari, W. Wulfhekel, M. Alouani, and E. Beaurepaire: *Spin crossover in Fe(phen)$_2$(NCS)$_2$ complexes on metallic surfaces*. The Journal of Chemical Physics **146**.9 (2017), p. 092312 (cit. on pp. 104, 106).

[145] S. Gueddida, M. Gruber, T. Miyamachi, E. Beaurepaire, W. Wulfhekel, and M. Alouani: *Exchange coupling of spin-crossover molecules to ferromagnetic Co islands*. The Journal of Physical Chemistry Letters **7**.5 (2016), pp. 900–904 (cit. on pp. 105, 106, 108, 123).

[146] E. König and K. Madeja: *Unusual magnetic behaviour of some iron(II)–bis-(1,10-phenanthroline) complexes*. Chemical Communications (London) 3 (1966), pp. 61–62 (cit. on p. 106).

[147] S. Shi, G. Schmerber, J. Arabski, J.-B. Beaufrand, D. Kim, S. Boukari, M. Bowen, N. Kemp, N. Viart, G. Rogez, et al.: *Study of molecular spin-crossover complex Fe(phen)$_2$(NCS)$_2$ thin films*. Applied Physics Letters **95**.4 (2009), p. 202 (cit. on p. 106).

[148] Y. Takahashi, T. Miyamachi, K. Ienaga, N. Kawamura, A. Ernst, and F. Komori: *Orbital selectivity in scanning tunneling microscopy: Distance-dependent tunneling process observed in iron nitride*. Physical Review Letters **116**.5 (2016), p. 056802 (cit. on pp. 106, 107).

[149] J. Gallego, D. Boerma, R. Miranda, and F. Ynduráin: *1D lattice distortions as the origin of the (2×2)p4gm reconstruction in γ'-Fe$_4$N(100): A magnetism-induced surface reconstruction*. Physical Review Letters **95**.13 (2005), p. 136102 (cit. on p. 107).

[150] J. Chen: *Local investigation of single magnetic molecules with scanning tunneling microscopy*. PhD thesis, Experimental condensed matter physics ; Band 21. Karlsruhe: KIT Scientific Publishing, 2018 (cit. on pp. 107, 157, 158).

[151] H. Chen, Y. Yu, Z. Wang, Y. Bai, H. Lin, X. Li, H. Liu, T. Miao, Y. Kou, Y. Zhang, et al.: *Thickness-driven first-order phase transitions in manganite ultrathin films*. Physical Review B **99**.21 (2019), p. 214419 (cit. on p. 116).

[152] M. Huijben, L. Martin, Y.-H. Chu, M. Holcomb, P. Yu, G. Rijnders, D. H. Blank, and R. Ramesh: *Critical thickness and orbital ordering in ultrathin $La_{0.7}Sr_{0.3}MnO_3$ films*. Physical Review B **78**.9 (2008), p. 094413 (cit. on p. 116).

[153] B. Kim, D. Kwon, J. H. Song, Y. Hikita, B. G. Kim, and H. Y. Hwang: *Finite size effect and phase diagram of ultra-thin $La_{0.7}Sr_{0.3}MnO_3$*. Solid State Communications **150**.13-14 (2010), pp. 598–601 (cit. on p. 116).

[154] J. Jesson, S. Trofimenko, and D. R. Eaton: *Spin equilibria in octahedral iron(II) poly(1-pyrazolyl)borates*. Journal of the American Chemical Society **89**.13 (1967), pp. 3158–3164 (cit. on p. 117).

[155] V. Davesne, M. Gruber, M. Studniarek, W. Doh, S. Zafeiratos, L. Joly, F. Sirotti, M. Silly, A. Gaspar, J. Real, et al.: *Hysteresis and change of transition temperature in thin films of $Fe\{[Me_2Pyrz]_3BH\}_2$, a new sublimable spin-crossover molecule*. The Journal of Chemical Physics **142**.19 (2015), p. 194702 (cit. on p. 117).

[156] M. Seredyuk, M. C. Muñoz, M. Castro, T. Romero-Morcillo, A. B. Gaspar, and J. A. Real: *Unprecedented multi-Stable spin crossover molecular material with two thermal memory channels*. Chemistry–A European Journal **19**.21 (2013), pp. 6591–6596 (cit. on p. 117).

[157] K. Bairagi, A. Bellec, C. Fourmental, O. Iasco, J. Lagoute, C. Chacon, Y. Girard, S. Rousset, F. Choueikani, E. Otero, et al.: *Temperature-, light-, and soft x-ray-induced spin crossover in a single layer of Fe^{II}-pyrazolylborate molecules in direct contact with gold*. The Journal of Physical Chemistry C **122**.1 (2018), pp. 727–731 (cit. on pp. 117, 127).

[158] R. A. Cowley: *The phase transition of strontium titanate*. Philosophical Transactions of the Royal Society of London. Series A: Mathematical, Physical and Engineering Sciences **354**.1720 (1996), pp. 2799–2814 (cit. on p. 123).

[159] K. Katoh, T. Kajiwara, M. Nakano, Y. Nakazawa, W. Wernsdorfer, N. Ishikawa, B. K. Breedlove, and M. Yamashita: *Magnetic relaxation of single-molecule magnets in an external magnetic field: An Ising dimer of a terbium(III)–phthalocyaninate triple-decker complex*. Chemistry–A European Journal **17**.1 (2011), pp. 117–122 (cit. on p. 126).

[160] T. Fukuda, W. Kuroda, and N. Ishikawa: *Observation of long-range f–f interactions between two f-electronic systems in quadruple-decker phthalocyanines*. Chemical Communications **47**.42 (2011), pp. 11686–11688 (cit. on p. 126).

[161] T. Fukuda, K. Matsumura, and N. Ishikawa: *Influence of intramolecular f-f interactions on nuclear spin driven quantum tunneling of magnetizations in quadruple-decker phthalocyanine complexes containing two terbium or dysprosium magnetic centers*. The Journal of Physical Chemistry A **117**.40 (2013), pp. 10447–10454 (cit. on p. 126).

[162] T. Fukuda, T. Biyajima, and N. Kobayashi: *A discrete quadruple-decker phthalocyanine*. Journal of the American Chemical Society **132**.18 (2010), pp. 6278–6279 (cit. on p. 126).

[163] M. Speckmann, H. P. Oepen, and H. Ibach: *Magnetic domain structures in ultrathin Co/Au(111): On the influence of film morphology*. Physical Review Letters **75** (1995), pp. 2035–2038 (cit. on p. 127).

[164] P. Bruno and C. Chappert: *Oscillatory coupling between ferromagnetic layers separated by a nonmagnetic metal spacer*. Physical Review Letters **67** (1991), pp. 1602–1605 (cit. on p. 127).

[165] A. Fuss, S. Demokritov, P. Grünberg, and W. Zinn: *Short-and long period oscillations in the exchange coupling of Fe across epitaxially grown Al-and Au-interlayers*. Journal of Magnetism and Magnetic Materials **103**.3 (1992), pp. 221–227 (cit. on p. 127).

List of Abbreviations

CFG	Crystal field theory
DOS	Density of states
$DyPc_2$	Bis(phthalocyaninato)dysprosium
Fe-Phen	$Fe(1,10\text{-phenanthroline})_2(NCS)_2$
Fe-Pyrz	$Fe\{[Me_2Pyrz]_3BH\}_2$
FWHM	Full width at half maximum
FY	Fluorescence yield
HOMO	Highest occupied molecular orbital
HS	High spin
HTS	High-temperature superconductor
HV	High voltage
IETS	Inelastic electron tunneling spectroscopy
JT	Joule-Thomson
LDOS	Local density of states
LIESST	Light-induced excited spin state trapping
LHe	Liquid helium
LN_2	Liquid nitrogen
LS	Low spin
LSMO	Lanthanum strontium manganate
LUMO	Lowest unoccupied molecular orbital
MO	Molecular Orbital
MOKE	Magneto-optic Kerr effect
$M(acac)_3$	Metal(III)-acetylacetonate
Pc	Phthalocyanine
QTM	Quantum tunneling of magnetization
RTN	Random telegraph noise
SCO	Spin crossover
SMM	Single-molecule magnet
SNR	Signal to noise ratio
SOMO	Singly occupied molecular orbital
SOXIESST	Soft x-ray-induced excited spin state trapping
sp-STM	Spin-polarized Scanning tunneling microscopy

STM	Scanning tunneling microscopy/microscope
STO	Strontium titanate
STS	Scanning tunneling spectroscopy
TEY	Total electron yield
TMP	Turbo molecular pump
TMR	Tunneling magnetoresistance
UHV	Ultra high vacuum
XAS	X-ray absorption spectroscopy
XMCD	X-ray magnetic circular dichroism
ZFS	Zero field splitting

Appendix

1 Bis(phthalocyaninato)dysprosium Molecules

The first successful spin-polarized measurements on $DyPc_2$ on Au(111) were in fact achieved with a ferromagnetic cobalt-coated tungsten tip. These results shall be presented in the following. In contrast to the results presented in the main part of the thesis in section 4.4, these measurements were performed on a molecule inside an island instead of a single molecule. The experiments were performed at the dilution STM at roughly 45 mK.

First, figure 1a shows some exemplary spin-polarized spectra. Like before the two peaks of the split Kondo resonance exhibit different heights and their asymmetry varies with the applied magnetic field. Again this peak asymmetry was measured for various magnetic field values. In contrast to the procedure described in section 4.4, substraction of the background and normalization of these asymmetries was analogue for positive and negative polarizations. The result is shown in figure 1b. In general, a more complex curve of the asymmetry results compared to the data shown for the chromium tip. On the first sight, this plot reminds of the typical butterfly-shaped hysteresis curves, typically obtained for the TMR in spin valves: The asymmetry is saturated at large fields. As the magnetic field decreases - coming from larger positive fields - the asymmetry decreases smoothly until it changes sign at roughly -50 mT. Additionally, a second sudden inversion of the spin-polarization occurs at roughly -100 mT. The mirrored behavior is observed for the opposite changing direction of the applied magnetic field. The first notion in order to explain this curve would be, that the molecule spin changes sign at -50 mT, when the stray field of the tip is compensated by the coil, and that additionally the tip magnetization

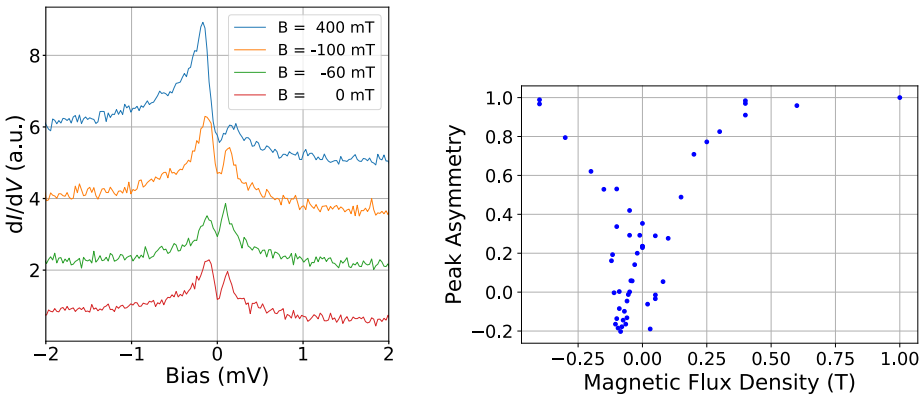

(a) **(b)**

Figure 1: Spin-polarized tunneling spectra and Kondo peak asymmetry for $DyPc_2$ using a ferromagnetic tip. (a) A bias offset was removed for all spectra. Lock-in parameters: 50 µV modulation at 1.7 kHz. (b) The peak asymmetries are plotted as function of the applied magnetic field.

flips at −100 mT, which in turn would correspond to the tip coercive field. However, with this it is difficult to understand why the spin polarization increases so slowly with the external magnetic field. At such low temperatures, saturation should already occur at roughly 100 mT of effective field, which is the sum of applied field and tip stray field, as discussed in section 4.4.

Since the magnetic field dependence of the tip stray field is unknown, in the next step the peak asymmetries were plotted as function of the width of the Kondo splitting. The latter represents the energy gap between the two states of the spin 1/2 with opposite spin orientation. Accordingly, this corresponds to the internal field (B_{int}), which is the total field felt by the spin 1/2. This in turn will be given by the sum of applied field, tip stray field and exchange field. In order to extract the peak position and the peak asymmetry at the same time, the following model function

$$\begin{aligned}\sigma(\epsilon) = \sigma_0 + A_{\mathrm{K}}/2\,[(1-\eta_{\mathrm{K}})f(\epsilon_{\mathrm{K}}-\epsilon,\Gamma) + (1+\eta_{\mathrm{K}})f(\epsilon_{\mathrm{K}}+\epsilon,\Gamma)] \\ + A_{\mathrm{S}}/2\,[(1-\eta_{\mathrm{S}})\Theta(\epsilon_{\mathrm{K}}-\epsilon,T) + (1+\eta_{\mathrm{S}})\Theta(\epsilon_{\mathrm{K}}+\epsilon,T)]\end{aligned} \tag{1}$$

similar to reference [134], was fitted to the tunneling spectra. Therein, $f(\epsilon, \Gamma)$ represents a Frota function (see section 2.3.3) and $\Theta(\epsilon, T)$ is the thermally broadend step function with

$$\Theta(\epsilon) = \frac{1 + (x-1)\exp(x)}{(\exp(x)-1)^2} \quad \text{and} \quad x = \epsilon/(k_\mathrm{B}T). \tag{2}$$

As an example, figure 2a shows the tunneling spectrum at zero magnetic field including the fit. It turns out, though, that this model contains too many free parameters. Especially the peak position cannot be fully independent of the broadening of Kondo resonance and step function. Therefore, for the residual fits the values of Γ and the effective temperature T needed to be fixed to the values obtained from the fit in figure 2a:

$$\Gamma = 0.06\,\mathrm{meV}, \quad T = 168\,\mathrm{mK}. \tag{3}$$

The result for the polarization η_K of the split Kondo resonance is shown in figure 2b. Therein, the internal field B_int is given by the fitted peak positions via $\epsilon_\mathrm{K} = g_S \mu_B B_\mathrm{int}$. Moreover, the solid line is an offset Brillouin function for a spin $1/2$ with a Landé factor of $g_S = 1.85$ given by the expression

$$\eta_\mathrm{K} = \tanh\left(\frac{g_S \mu_B (B - B_0)}{2k_\mathrm{B}T}\right). \tag{4}$$

The effective temperature was set analogue to the fits to $T = 168\,\mathrm{mK}$.

From this follows the offset field of $B_0 = (703 \pm 14)\,\mathrm{mT}$. Initially one might expect, that this internal field value, where the two peaks of the split Kondo resonance exhibit the same height, corresponds simply to the exchange field, as the tip stray field should be precisely compensated by the external field. It should be stressed, though, that the result for this offset field is not independent of the parameter Γ which in turn was fixed for the fits. Choosing a larger (smaller) value for Γ results in smaller (larger) energy values ϵ_K and thus in a smaller (larger) offset field. Nevertheless, this plot clearly illustrates, that the spin polarization as function of the internal field behaves as expected for a spin $1/2$. Still it is not easy to understand the hysteretic curve of figure 1b, especially the slow rise of the spin polarization. The latter might be attributed to an unknown magnetic field dependence of the tip spin polarization. Furthermore, it seems likely that the easy axis

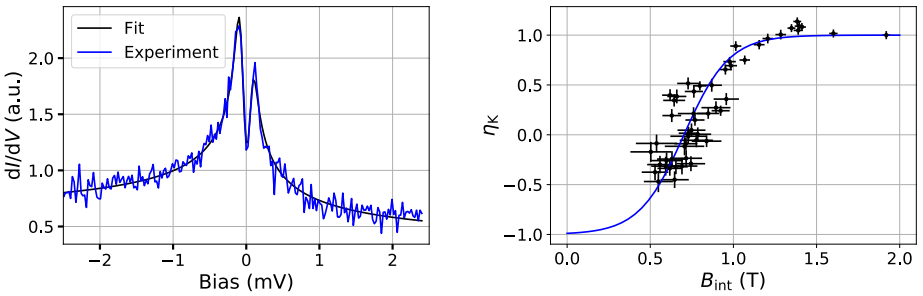

(a) **(b)**

Figure 2: Determination of peak asymmetry as function of peak splitting. (a) An exemplary spectrum (at zero magnetic field) with the corresponding fit is shown. (b) The resulting asymmetries as function of the effective field is shown including the error bars. The effective field results from the fitted Kondo peak position via $B_{\mathrm{int}} = \epsilon_{\mathrm{K}}/(g_S \mu_{\mathrm{B}})$. The solid line is an offset Brillouin function for a spin 1/2 with $g_S = 1.85$.

of the tip magnetization is not precisely perpendicular with respect to the sample surface, but tilted.

In conclusion, this analysis shows, that it is hard to get any insights on the dysprosium spin with ferromagnetic tips. Especially in the limit of small external fields, which would be most interesting in this respect, it is particularly difficult to draw any conclusions, as the unknown stray field of the tip becomes the dominant factor. This led to the use of antiferromagnetic tips in the next step.

2 3d Metal Acetylacetonates

This section gives some supplementary information on the project including the transition metal acetylacetonates. This includes the sample preparation parameters, the magnetic field dependence of the observed Kondo resonance, an attempt to fit the Kondo resonance with the perturbation theory model [86] and an additional island structure.

Details on the Sample Preparation

Table 1 gives the deposition temperatures and labels the presented samples.

Table 1: Deposition parameters for the different samples of M(acac)$_3$/Cu(111)

Sample label	$T_{\text{Deposition}}$ (°C)	T_{Degas} (°C)
Cr(acac)$_3$ sample 1	57	62
Cr(acac)$_3$ sample 2	48	62
Cr(acac)$_3$ sample 3	62	70
Co(acac)$_3$	44	44

Magnetic Field Dependence of the Kondo Resonance and Perturbation Theory Approach

The magnetic field dependence of the Kondo resonance measured on the chromium dumbbells is illustrated in figure 3a. The spectrum at 1.7 T looks a bit wider and less sharp compared to the spectrum at zero field, which is in agreement with the expectations. Moreover, in figure 3b the spectrum of figure 5.5c is fitted using the perturbative approach of [86]. The fit yields

$$T = (8.6 \pm 0.1)\,\text{K} \tag{5}$$
$$J = -0.132 \pm 0.002 \tag{6}$$
$$U = -0.048 \pm 0.006 \tag{7}$$
$$B_2^0 = (-0.38 \pm 0.04)\,\text{meV} \tag{8}$$
$$B_2^2 = (-1.16 \pm 0.05)\,\text{meV}. \tag{9}$$

It appears, though, as if this model does not describe the measured spectrum well-enough. It seems like this model can only account for the observed peak width by assuming a quite high effective temperature. Though this results in the peak not being high enough. Moreover, the step heights are a bit too high.

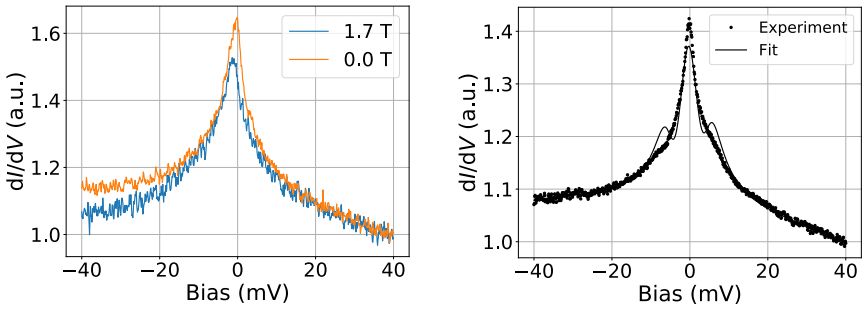

(a) Magnetic field dependence **(b)** Perturbative approach

Figure 3: Magnetic field dependence and perturbative approach to the Kondo resonance observed on the chromium dumbbells. Both spectra were measured at a lock-in modulation of 0.1 mV.

Additional island structure on the $Cr(acac)_3$ sample

Besides the hexagonal island structure, another structure was observed. However, this structure, which is shown in figure 4, occurred only very rarely on sample 1.

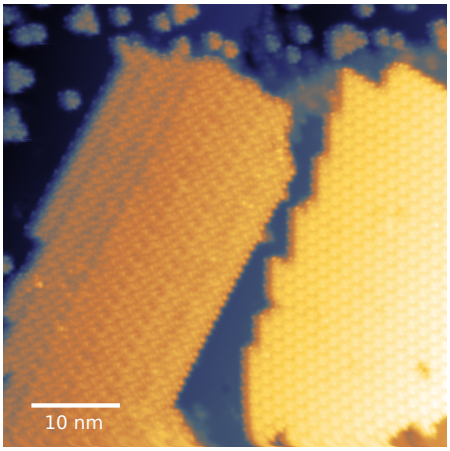

Figure 4: Alternative island structure observed on $Cr(acac)_3$ sample 1. Topography parameters: 1.5 V, 5 pA.

3 Spin Crossover Molecules on Ferromagnetic Substrates

3.1 Fe-Phen on Fe_2N/Cu(100)

Discussion of previous results

Here, the discrepancy between the observations presented in chapter 6.2.1 and the previous works of reference [150] shall be discussed more elaborately. In chapter 6.2 the issue, that completely different results were reported on the Fe-Phen on Fe_2N system in [150], was mentioned already. There, molecules resembling Fe-Phen on Cu(100) were observed on one sample. Besides the two lobes that correspond to the phenanthroline groups, these molecules showed an additional tail in topography. On such a molecule a robust and reversible switching between two states, analogue to the behavior of Fe-Phen molecules on Cu_2N/Cu(100), was observed. It was concluded, that this switching might correspond to the SCO such that Fe-Phen molecules preserved their ability to switch their spin state when adsorbed on Fe_2N, as desired. However, such a behavior was never observed on the sample presented in chapter 6.2. There, also additional control experiments were presented, in order to ensure both, the quality of the Fe_2N film and the successful molecule growth. The problem there was, that the underlying physics of these results could not be fully understood. Nevertheless, the question remains, what the origin of these contradicting observations might be.

On one sample of rather poor Fe_2N quality a single molecule with similar properties as reported in [150] was observed. For the sake of completeness, these observations will be presented in the following in order to dare an attempt to explain the different observations with growth problems of Fe_2N. These measurements of this aforementioned molecule are presented in figure 5. First, a topography is shown in figure 5a. The molecule exhibits an additional tail strikingly similar to the molecules presented in [150]. In the molecule's center - marked by a black cross - several I-V-spectra were acquired. One exemplary spectrum is shown in figure 5c. Indeed,

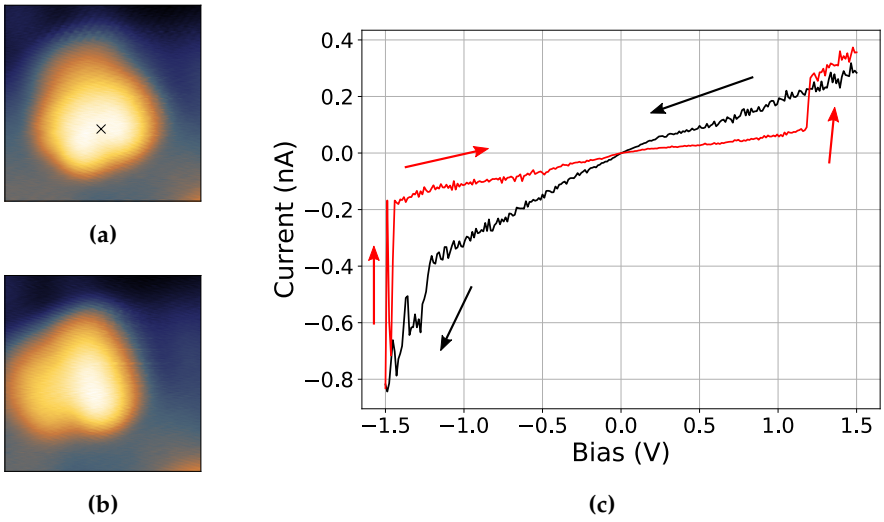

Figure 5: Measurements of a molecule on a failed sample of Fe-Phen on Fe_2N. (a) shows the topography of a molecule. The black cross marks the position where several I-V curves were measured subsequently. (c) shows one of these measurements. The arrows indicate the sweep direction of the tunneling voltage. (b) shows the topography of the same molecule after several of such bias sweeps. Obviously, after these experiments, the molecule was displaced. Topography parameters: $(3\,\mathrm{nm} \times 3\,\mathrm{nm},\ 0.2\,\mathrm{V},\ 50\,\mathrm{pA})$.

sudden changes in the tunneling current occurred during the bias sweep, which appear as molecular switching events. Figure 5b, however, shows the topography of the very same molecule acquired after several of such bias sweeps. Obviously, the molecule was displaced. Hence, the jumps in the tunneling current during the sweeps likely correspond to mere movements of the molecules and not - as assumed before - to the changes of an internal degree of freedom. It seems possible that the molecular switching observed in [150] has a similar origin.

Last, figure 6 shows the topography of the sample on which these observations were made. In contrast to the sample presented in chapter 6.2, this sample is very inhomogeneous. The slightly brighter stains within one terrace presumably correspond to iron aggregations underneath the Fe_2N layer [124]. It seems, that the overall quality of this Fe_2N film is lower. Possibly, the results presented in [150] were measured on a similar sample

and the observations are in accordance with the measurements shown in figure 5. In this case, the different results were related to a non-sufficient quality of the Fe_2N film.

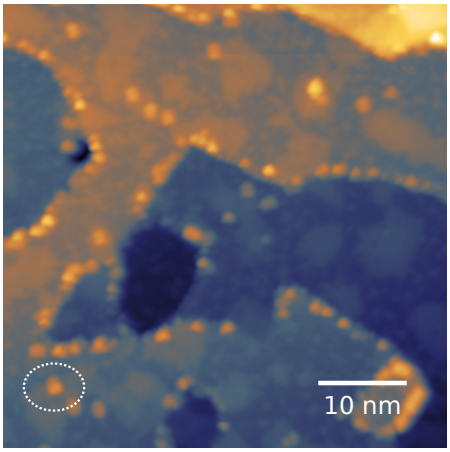

Figure 6: Topography of a non-homogeneous Fe-Phen on Fe_2N/Cu(100) sample. The quality of the Fe_2N film is quite poor. The dashed circle indicates the molecule of figure 5. Topography parameters: $(0.2\,\mathrm{V},\ 50\,\mathrm{pA})$.

Rotational switching

For the switching observed on type B molecules on the sample of Fe-Phen on Fe_2N (chapter 6.2), figure 7 shows differential conductance maps at various energies for both states. For every map, it looks like the switching corresponds to a rotation.

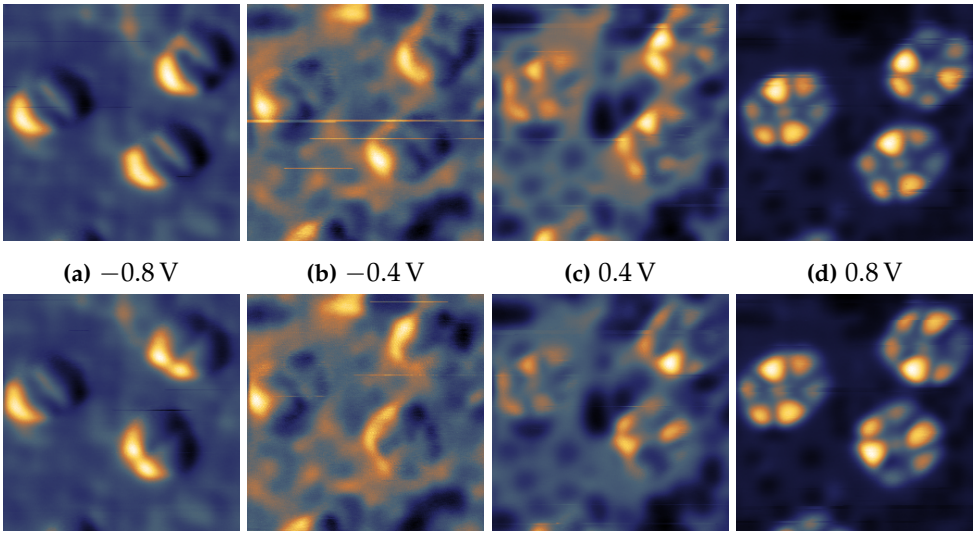

Figure 7: dI-dV maps for the rotational-like switching of Fe-Phen on Fe_2N/Cu(100). Two of the molecules have been switched. For several tunneling voltages, the two states are shown. For every map, the switching looks like a rotation by 90°. The scan frame is rotated by 30°. $(6\,\mathrm{nm} \times 6\,\mathrm{nm},\ 500\,\mathrm{pA})$.

3.2 Fe-Pyrz on LSMO

XAS LS Comparison

Figure 8 shows the same XAS spectrum as figure 6.16b, but superimposed with the LS reference data on the Fe-Pyrz powder sample from figure 6.13 of [101]. From this it is apparent that the measured spectra are not compatible with Fe-Pyrz molecules in the LS state.

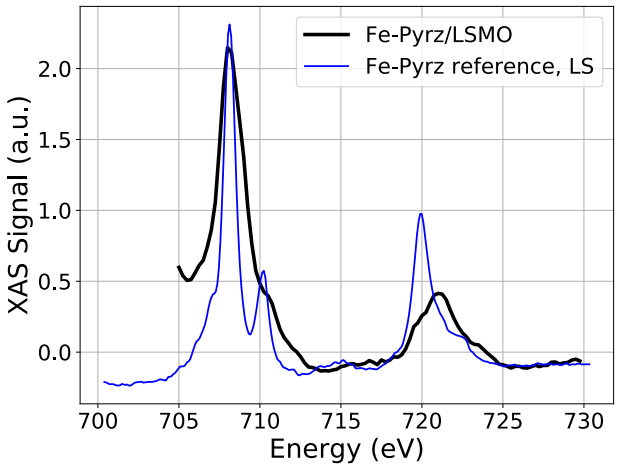

Figure 8: XAS on Fe-Pyrz/LSMO and comparison to the LS state. A reference XAS spectrum of the Fe-Pyrz powder sample of [101] in the LS state (scaled and offset in x and y) is superimposed on a measured spectrum on the Fe-Pyrz/LSMO sample at room temperature (analogue to figure 6.16).

Acknowledgements

What can I say. It has been a great, challenging, rewarding, stressful, happy and awesome time. I gave all I could and even though it cost lots of efforts, time, sacrifice and endurance, I am extremely grateful I could get through and evolve personally in so many ways in the process. Still I have countless great memories and will always hold the time in our great group in highest regard. And frankly, without the incredible support of friends, colleagues, family and collaborators, this work, my studies and the great experiences I made over the last years would never have been possible. Therefore, my most sincere gratitude goes to...

... Prof. Dr. Wulf Wulfhekel for giving me the chance to be a PhD candidate in his group, for his supervision and support, for his valuable experience, for discussions, input and ideas, for all the joyful moments I was able to experience during summer schools, conferences, group seminars and all other group happenings, for everything else I am forgetting but most of all for all the things I learned during almost five years in his group.

... Prof. Dr. Wolfgang Wernsdorfer for being the second referee of this thesis.

... Prof. Dr. Mario Ruben, Dr. Svetlana Klyatskaya and Dr. Eufemio Moreno-Pineda for providing the $DyPc_2$ molecules and the ongoing colaboration.

... Prof. Dr. Eric Beaurepaire, Dr. Martin Bowen and all other collaborators from the IPCMS in Strassbourg.

... Dr. Ana B. Gaspar for providing the Fe-Pyrz molecules.

... Prof. Dr. Markus Ternes for valuable discussions and his Kondo perturbation theory simulation script.

... Dr. Timofey Balashov for all his countless contributions to all kinds of issues in the group and his Kondo program.

... the French-German Graduate School on Hybrid Organic-Inorganic Nanostructures and Molecular Electronics and the DFG.

... the Landesstiftung Baden-Württemberg for my scholarship and two years of funding the projects on $DyPc_2$ and Metal Acetylacetonates.

... Dr. Peter Nagel and Dr. Stefan Schuppler for making the x-ray absorption measurements at the WERA beamline possible.

... Dr. Jinjie Chen, Dr. Timofey Balashov and Dr. Hongyan Chen for common experiments and lab teamwork, but especially to Hongyan, who was such a great support, a beacon of good mood and such a pleasant lab partner during the last year.

... all other present and past members of our group including Timofey, Lukas, Marie, Fang, Kevin, Jasmin, Jinjie, Sergey, Vibhuti, Thomas, Loïc, Julian, Gabriel, Hongyan, Haoran and Hung-Hsiang for the great atmosphere, for making the past years incredibly fun and for all I was able to learn from you.

... all my friends and family for their incredible support, their genuine believe in me and my abilities and for making these past years in Karlsruhe simply unforgettable.

Thank you!